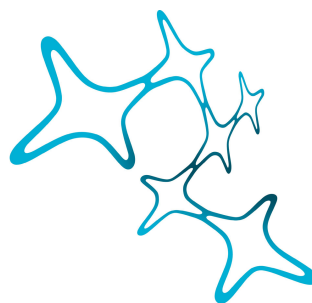

Intrinsic Structure of the Inferior Colliculus

Lu Li



Graduate School of
Systemic Neurosciences
LMU Munich

München 2016

Intrinsic Structure of the Inferior Colliculus

Lu Li

Dissertation
of the Graduate School of Systemic Neurosciences
of Ludwig–Maximilians–Universität München

Submitted by

Lu Li

from Dalian

München, December 8th, 2016

Supervisor: Prof. Dr. Christian Leibold

Second reviewer: Prof. Dr. Conny Kopp-Scheinpflug

Third reviewer: Prof. Dr. George D Pollak

Oral defense: March 23rd, 2016

Acknowledgments

I would like to express my deep gratitude to Professor Dr. Christian Leibold and Professor Dr. Felix Felmy, my research supervisors, for their patient guidance, enthusiastic encouragement and useful critiques of this research work, as well as their additional support when I was facing difficulties. I would also like to thank Prof. Dr. Hans Straka and Dr. Ilona Grunwald Kadow for their scientific advices and assistance in keeping my progress on schedule. My grateful thanks are also extended to Dr. Lina Yassin, for her scientific conversations, practical advices, and for her advice with cell subdivisions control, to Dr. Susanne Radtke-Schuller, who helped me with the cell morphology studies and for her support in cell subdivision classification, and to Dr. Olga Alexandrova, for her help in axon reconstruction imaging.

I would also like to extend my thanks to the GSN management staff for their advices and assistance throughout my PhD time. Also thanks go to all my colleagues in the office and in the BCCN and the Biology Department in the Biocenter for their scientific help and for providing a friendly atmosphere and nice time.

Special thanks goes to Prof. Benedikt Grothe and to Prof. Anderas Herz for their support that helped me through the most difficult times.

Also special thanks to Prof. John Rinzal for his scientific inspirations and motivation.

Finally, I wish to thank my family for their great hearts and encouragement throughout my study.

Summary

The inferior colliculus (IC) is a major integrative center within the central auditory system, which contains three main subdivisions, i.e. the central nuclei (ICc), the external cortex (ICx) and the dorsal cortex (ICd). The central nucleus is characterized by the fibro-dendritic laminae constructed from the dendrites and axons of its two principal cell types: the disc-shaped cells and the stellate cells. Whereas in the ICc ascending inputs converge from all auditory nuclei upstream, the external and dorsal cortex converge the descending inputs from all auditory nuclei downstream. Additionally, the external cortex is receiving ascending inputs from multisensory systems.

The IC plays an important functional role in the auditory system. A large amount of work has been done on the cell morphology and electrophysiology; however, less research work was done to study the intrinsic network, which is important to understand the computations performed by the inferior colliculus. Recently, the existence of excitatory and inhibitory intrinsic innervations has been proven in the ICc; however, it is still unclear whether the amount of intrinsic innervation and orientation depends on the location, the morphology of the cell or its intrinsic membrane parameters. Besides, the intrinsic inputs of other IC subdivisions are still unknown.

This thesis was a phenomenological study of the intrinsic innervation of the inferior colliculus neurons. We used whole-cell patch clamp technique combined with laser scanning photostimulation of caged glutamate in order to determine the organization of intrinsic inputs of the ICc and the ICx neurons

in the Mongolian gerbil. Our approach specifically aimed not only to study the intrinsic innervations and their regional differences, but also to find the correlations of intrinsic innervation with electrophysiological and morphological parameters.

The excitatory and inhibitory intrinsic inputs of neurons from the ICc and ICx were measured. In addition, the electrophysiology and morphology of the neurons were recorded. We were the first to find that in case of excitation, ICc cells had two preferred orientations that were arranged both in the isofrequency axis and in the tonotopic axis, and yet the innervation of ICx cells only oriented along the outer boundary of the IC. In contrast, the inhibitory innervations of both ICc and ICx neurons dispersed in different directions. Moreover, we found that the intrinsic innervations were regionally heterogeneous in their excitation-inhibition balance. Whereas cells in the dorso-medial ICc cells had a balanced intrinsic excitation and inhibition, excitation was prevalent in the ventro-lateral ICc and in the ICx. Besides, we compared the amount of inputs in paired regions. Thus we found that in the lateral ICc, there existed a narrow region spanning along the outer boundary of the ICc where cells received significantly smaller amounts of excitatory inputs than in the adjacent region (ICx). In addition, we found that ICx cells received more excitatory inputs than the ICc cells. Moreover, we found that the amount of excitatory intrinsic innervations was correlated with the apparent surface of the cells, and the amount of inhibitory intrinsic innervations was correlated with the membrane conductance of the cells. Thus we found that the dorso-medial ICc cells varied most in their membrane conductance, whereas the ICx cells were most similar in their membrane conductance and the lateral ICc cells were most similar in their apparent cell surface.

Contents

List of Figures	xv
List of Tables	xvii
List of Acronyms	xix
1 Introduction	1
1.1 Inferior Colliculus: A Central Nucleus in the Auditory System	1
1.1.1 Location in the Auditory System	2
1.1.2 Functional Role	5
1.2 Anatomical Neuronal Organization	5
1.2.1 Major Neuron Types	6
1.2.2 Connection between Neurons and Fibro-dendritic Laminae	8
1.2.3 Subdivisions	9
1.2.4 Connections between IC Subdivisions	10
1.2.5 Functional Domains build from Afferent Inputs	11
1.3 Electrophysiological Properties	13
1.3.1 Membrane Properties	13
1.3.2 Neuronal Firing Patterns	14

1.3.3	Characteristic Frequency and Tonotopic Structure . . .	14
1.4	Intrinsic Synaptic Connections and Motivation of the work . .	17
1.4.1	Indication of Intrinsic Synaptic Connections	17
1.4.2	Relationship between Anatomical Organization, Tono- topy and Intrinsic Synaptic Connection	17
1.4.3	State of the Art	20
1.4.4	Contribution of this Work	22
2	Material and Methods	25
2.1	Slice Preparation	25
2.2	Setup	26
2.3	Electrophysiology and UV Uncaging	28
2.4	Slice Fixation and Confocal Microscopy	35
2.5	Data Analysis	36
3	Results	39
3.1	General Cell Characterization	39
3.1.1	Electrophysiology	40
3.1.2	Morphology	52
3.1.3	Miniature Postsynaptic Currents Study	57
3.2	Organization of Intrinsic Innervations	60
3.2.1	Temporal Organization	63
3.2.2	Spatial Organization	66
3.2.3	Correlation to Electrophysiology and Morphology . . .	69
3.2.4	Regional Heterogeneity	73
3.2.4.1	Innervation Orientation	73

3.2.4.2	Innervation Profiles	78
4	Discussion	91
4.1	Intrinsic Innervation Organization: Dorso-medial ICc vs. Ventro-lateral ICc	92
4.2	Region of Distinct Intrinsic Innervation: Lateral ICc?	96
4.3	Intrinsic Innervation Orientation: Iso-frequency Axis, Tonotopy Axis or both?	99
4.4	Differences in the Innervation Organization of the ICx	104
4.5	Technical Considerations	107
4.6	Conclusion	110
	Author Contributions	135

List of Figures

1.1	Auditory pathways	2
1.2	Principal neurons and fibrodendritic lamina within ICc	7
1.3	Main subdivisions of IC	9
1.4	Schema of an ICc synaptic domain model.	12
1.5	Main firing Patterns of inferior colliculus (IC) neurons	15
1.6	Tonotopic structure of the IC	16
2.1	Setup and the light pathway	27
2.2	Effective spot size (ESS) calibration experiment	31
2.3	Scanning resolution (SR) calibration experiment	33
2.4	Stimulation layouts of SR and mapping input experiments	34
2.5	Working mechanism of uncaging experiment and PSC detection diagram	38
3.1	Neuronal firing patterns and their spatial distribution	41
3.2	Intrinsic membrane properties	49
3.3	Morphological properties and their correlations to electrophysiology	53
3.4	Miniature EPSC analysis	58
3.5	Miniature IPSC analysis	59

3.6	Latency map of direct and indirect PSCs	62
3.7	Spatial distribution of the amount of intrinsic inputs and their correlations to electrophysiological parameters	67
3.8	Intrinsic inputs related to morphological properties	72
3.9	Orientations of intrinsic innervations	74
3.10	Radial density of intrinsic inputs according to regions	85
3.11	Regional heterogeneity of intrinsic inputs and electrophysiological parameters	90

List of Tables

3.1 Paired student t-test on the spatial distribution of the three firing patterns.	44
3.2 Paired student t-test on the spatial distribution of cells with and without rebound spike.	46
3.3 Membrane properties of IC neurons from the region of interest (ROI)	48
3.4 Morphological properties and the correlations to electrophysiology	54
3.5 Regional heterogeneity of intrinsic inputs , electrophysiological parameters and correlations	79
3.6 Paired student t-tests on the intrinsic inputs and electrophysiological parameters according to regions	81
3.7 F-tests on the intrinsic inputs and electrophysiological parameters according to regions	82

List of Acronyms

AC	auditory cortex
CN	cochlear nucleus
DCN	dorsal cochlear nucleus
VCN	ventral cochlear nucleus
IC	inferior colliculus
ICc	central nucleus of inferior colliculus
ICx	external cortex of the inferior colliculus
ICd	dorsal cortex of the inferior colliculus
dm	dorso-medial of ICc
lt	lateral of ICc
vl	ventro-lateral of ICc
ex	external cortex of IC
LL	lateral lemniscus
VNLL	ventral nucleus of the lateral lemniscus
DNLL	dorsal nucleus of the lateral lemniscus
SC	superior colliculus

SOC	superior olivary complex
MSO	medial superior olivary nuclei
LSO	lateral superior olivary nuclei
MGB	medial geniculate body
ANOVA	analysis of variance
Ampl	amplitude
AP	action potential
CC	cell characterization
CF	characteristic frequency
DF	dendritic field
DFA	dendritic field area
DFL	dendritic field length
DFW	dendritic field width
ESS	effective spot size
FWHM	full width of half maximum
PSC	postsynaptic current
EPSC	excitatory presynaptic current
IPSC	inhibitory presynaptic current
mPSC	miniature postsynaptic current
mEPSC	miniature excitatory postsynaptic current
mIPSC	miniature inhibitory postsynaptic current

RF	roundness factor
ROI	region of interest
SEM	standard error of the mean
SFM	sinusoidally frequency-modulated
SR	scanning resolution
UV	ultraviolet
VSD	voltage sensitive dye
KS-test	Kolmogorov-Smirnov test
4AP	4-Aminopyridine ($C_5H_6N_2$)
AMPA	AMPA receptor
AMPA	alpha-amino-3-hydroxy-5-methylisoxazole-4-propionic acid ($C_7H_{10}N_2O_4$)
AP5	2-amino-5-phosphonovalerate ($C_5H_{12}NO_5P$)
ATP	adenosine triphosphate ($C_{10}H_{16}N_5O_{13}P_3$)
DNQX	6,7-dinitroquinoxaline-2,3-dione ($C_8H_2N_4O_6$)
EGTA	ethylene glycol tetraacetic acid ($C_{14}H_{24}N_2O_{10}$)
GABA	gamma-aminobutyric acid ($C_4H_9NO_2$)
GABA_AR	GABA _A receptor
GAD	glutamate decarboxylase
GTP	guanosine-5'-triphosphate ($C_{10}H_{16}N_5O_{14}P_3$)
HEPES	4-(2-hydroxyethyl)-1-piperazineethanesulfonic acid ($C_8H_{18}N_2O_4S$)

MNI	4-methoxy-7-nitroindolinyI ($C_9H_{10}N_2O_3$)
NMDA	N-methyl-D-aspartate ($C_5H_9NO_4$)
PBS	phosphate buffer saline
SR 95531	SR95531 (Gabazine) ($C_{15}H_{17}N_3O_3 \cdot HBr$)
STRY	strychnine hydrochloride ($C_{21}H_{22}N_2O_2 \cdot HCl$)
TTX	tetrodotoxin ($C_{11}H_{17}N_3O_8$)
TEA	tetraethylammonium ($C_8H_{20}N^+$)

1 Introduction

The inferior colliculus (IC) is a major integrative center within the auditory system (Ahuja and Wu, 2007). A contemporary study of the IC was done 1911 by Ramón y Cajal, who used Golgi staining methods to define the morphological subdivisions of the IC (Ramón y Cajal, 1911). During that time, the IC was still only seen as a reflex center (Prus, 1899; Bekhterev, 1908; Spiegel, 1926). Since the publication of Rasmussen 1946, the IC has been considered to be an important *relay* station in the auditory system (Rasmussen, 1946). Until today, enormous efforts have been made to study the IC with respect to its neuronal organization and its function, which since then has proven the pivotal role of the IC in the auditory system.

1.1 Inferior Colliculus: A Central Nucleus in the Auditory System

The inferior colliculus plays an important role in auditory processing. This importance can be evidenced in two aspects: its pivotal location in the auditory system and its functional role.

1.1.1 Location in the Auditory System

The inferior colliculus (IC) is located in the center of the central auditory system. The cochlear nucleus (CN), the superior olivary complex (SOC) and the lateral lemniscus (LL) are located upstream of the IC in the ascending auditory pathway, whereas the medial geniculate body (MGB) and the auditory cortex (AC) are located downstream of the IC (Fig. 1.1).

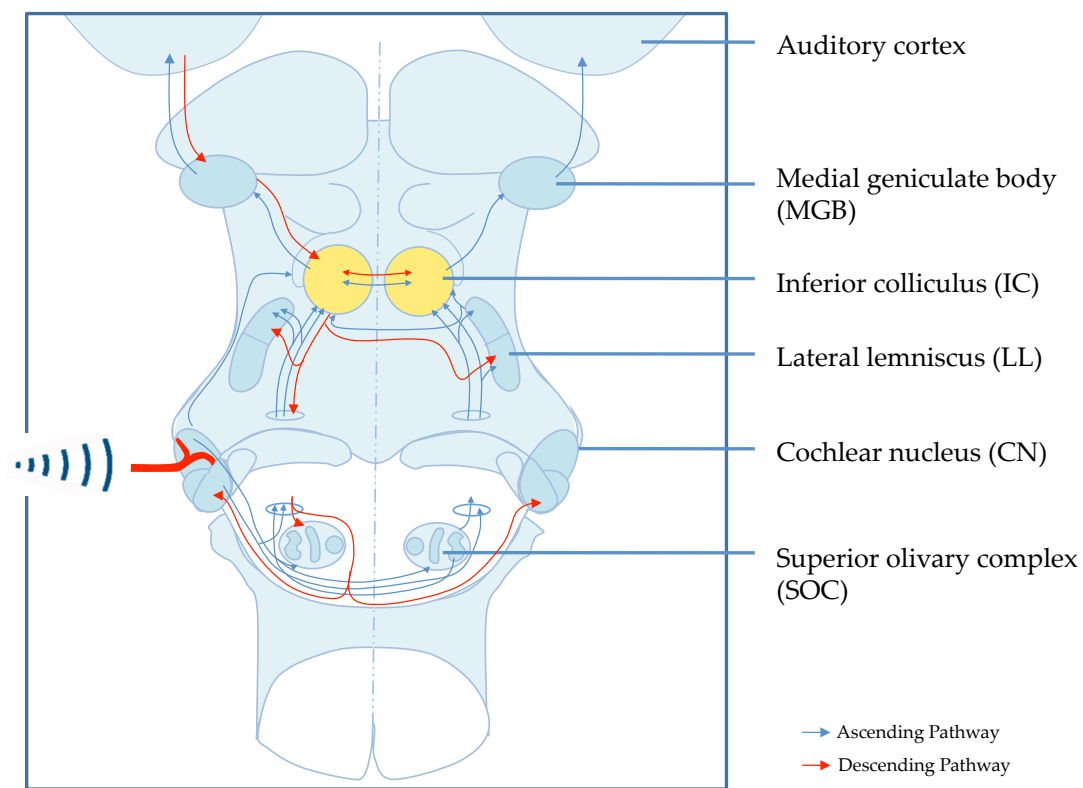


Figure 1.1: Auditory pathways. The ascending (red curves) and descending (dark blue curves) auditory pathways are shown traversing the six main nuclei of the auditory system: the cochlear nucleus (CN), the superior olivary complex (SOC), the lateral lemniscus (LL), the inferior colliculus (IC), the medial geniculate body (MGB) and the auditory cortex (AC). (Figure based on Nieuwenhuys et al., 2007).

To understand the ascending pathways (Fig. 1.1), we begin with the sound waves analyzed into different frequencies in the inner ear on the basilar mem-

brane. The sound waves are then transmitted through the cochlear nerve into the central auditory system (Nieuwenhuys et al., 2007). The CN is the first relay station of the central auditory system (Sotoca et al., 2014), where basic response patterns are generated (Schreiner and Winer, 2005). It can be further divided into the dorsal cochlear nucleus (DCN) and the ventral cochlear nucleus (VCN) (Nieuwenhuys et al., 2007). Several ascending pathways emerge from the CN and terminate in the SOC, the LL and the IC bilaterally with major collaterals sending to the LL, which consists of the dorsal nucleus of the lateral lemniscus (DNLL) and the ventral nucleus of the lateral lemniscus (VNLL) (Kudo and Niimi, 1980; Moore, 1985; Cant and Benson, 2006, 2008; Nieuwenhuys et al., 2007). The SOC is important for binaural information processing (Moore, 1991), and it can be further divided into the medial superior olivary nuclei (MSO) and the lateral superior olivary nuclei (LSO) (Vater et al., 1995). The SOC in each hemisphere projects only to the ipsilateral LL then to the IC bilaterally, but one direct projection from the LSO enters the contralateral LL and IC (Kudo and Niimi, 1980; Cant and Benson, 2006). Furthermore, the ascending pathways run from the IC of both hemispheres to the MGB ipsilaterally then to the AC bilaterally (Peruzzi et al., 1997; Venkataraman and Bartlett, 2013).¹ Thus, the IC is almost obligatory in the ascending auditory pathway, with one exception that a direct projection from the SOC and the LL to the supragenulate nucleus bypassing the IC (Casseday et al., 1989).

Likewise, almost all descending pathways pass through the IC. Firstly, they

¹the nucleus of the brachium of the IC projects extrathalamically directly into the AC bypassing the MGB (Rouiller et al., 1989), which is omitted in Figure 1.1 and the auditory pathway description in this paragraph.

project from the AC to the MGB ipsilaterally and then to the IC ipsilaterally, or bypass the MGB and project to the IC directly (Straka et al., 2015). From the IC, the projections run to the LL bilaterally, SOC ipsilaterally mainly and finally to the ipsilateral CNs bilaterally (Nieuwenhuys et al., 2007; Druga and Syka, 1984). However, the IC is not an obligatory nucleus in the descending auditory pathways, because of the direct descending projections bypassing the IC, e.g. the monosynaptic projection from the AC to the CN. (Chandrasekaran and Kraus, 2010).

Besides the above described connections, there are in addition the commissural connections at most stages of the auditory system with the exception of the MGB (Schreiner and Winer, 2005; Chandrasekaran and Kraus, 2010). This commissural connection is called *commissure of Probst* in the DNLL (Winer and Schreiner, 2005) and is called commissure of the IC in the IC (Reetz and Ehret, 1999). The auditory ascending, descending pathways and the commissural connections lead to the metaphor that the IC is like a hub that is located in the center of the auditory system (Casseday et al., 2002).

Beyond the auditory system, several IC subnuclei are also connected with other sensory systems, e.g. the spinal cuneate and the gracile nuclei of the somatosensory system (Feldman and Kruger, 1980; Aitkin et al., 1981; Tokunaga et al., 1984; Wiberg et al., 1987), the substantia nigra and globus pallidus of the motor system (Yasui et al., 1991; Moriizumi and Hattori, 1991; Shammah-Lagnado et al., 1996) and the parabrachial nucleus of the superior colliculus in the visual system (Edwards et al., 1979; Appell and Behan, 1990; King et al., 1998). This lends further support to the notion that the IC is a multisensory integrative nucleus (Ahuja and Wu, 2007).

1.1.2 Functional Role

From the anatomically pivotal position and the multisensory connections, multiple functional roles of the IC can be concluded (Malmierca et al., 2005). Generally, the IC takes part in all basic auditory functions, i.e. frequency, temporal and spatial information processing, which can be concluded from the existence of functionally specific neurons in the IC, e.g. neurons specialized in duration tuning (Sayegh et al., 2014; Casseday et al., 1994, 2000), in delay tuning (Feng et al., 1978) and neurons that are SFM-selective (Casseday et al., 1997)

The collaboration of these functionally specific neurons further enables the IC to take part in advanced functional activities, e.g. sound localization and binaural integration (Nakamoto et al., 2014), gain control (Xiong et al., 2013), the precedence effects (Wang et al., 2014), selectivity for complex acoustic features like speech and vocalization (Willmore et al., 2014; Sturm et al., 2014) and other multisensory functions (Muller-Ribeiro et al., 2014).

1.2 Anatomical Neuronal Organization

So far, by looking at its anatomical location and interconnection, we have outlined that the IC is a pivotal nucleus in the auditory system. The foundation to further understand the important functional role of the IC, however, is its neuronal organization. The following introduction of the inner structure of the IC is organized from single neurons to larger organizations and from the inside to the outside.

Since in the context of this work, middle cut frontal slices were used, only

neuronal organizations relevant for this work, i.e. the neurons, dendritic fields, axons and subdivisions observable from this specific perspective will be introduced. Neuronal organizations more rostrally or caudally are described in detail in other publications (Morest and Oliver, 1984; Oliver, 1984; Cant and Benson, 2005; Schreiner and Winer, 2005; Loftus et al., 2008).

1.2.1 Major Neuron Types

There are two major types of morphological neurons inside the center area of the IC: the stellate neuron and the disc-shaped neuron (Mylius et al., 2013; Morest and Oliver, 1984; Meininger et al., 1986; Wallace et al., 2012).

Disc-shaped neurons (Figure 1.2 bottom right inset) have an ovoid soma of about 5–30 μm in size with one or two stem dendrites at each end of the pole (Rockel and Jones, 1973b; Meininger et al., 1986). Each stem dendrite further branches into an either radial or tufted pattern (Meininger et al., 1986), and some of the dendrites are heavily spined (Rockel and Jones, 1973b), whereas others are only slightly spined or have no spine (Wallace et al., 2012). The dendritic fields of disc-shaped neurons are very characteristic; they extend in two dimensions and are narrow in the third dimension (Malmierca et al., 1993). The longest axis can be up to 800 μm (Oliver et al., 1991) with slight differences between species (cat, Rockel and Jones 1973b; Oliver et al. 1991; monkey, FitzPatrick 1975; human, Geniec and Morest 1971), whereas the narrowest axis is up to 70 μm in diameter (Malmierca et al., 1993). The dendritic field as a whole can be seen as having the shape of a short cylinder or a disc-like form (Rockel and Jones, 1973b), which is the reason why these type of neurons are named disc-shaped neurons. The main axons of a disc-shaped neuron are

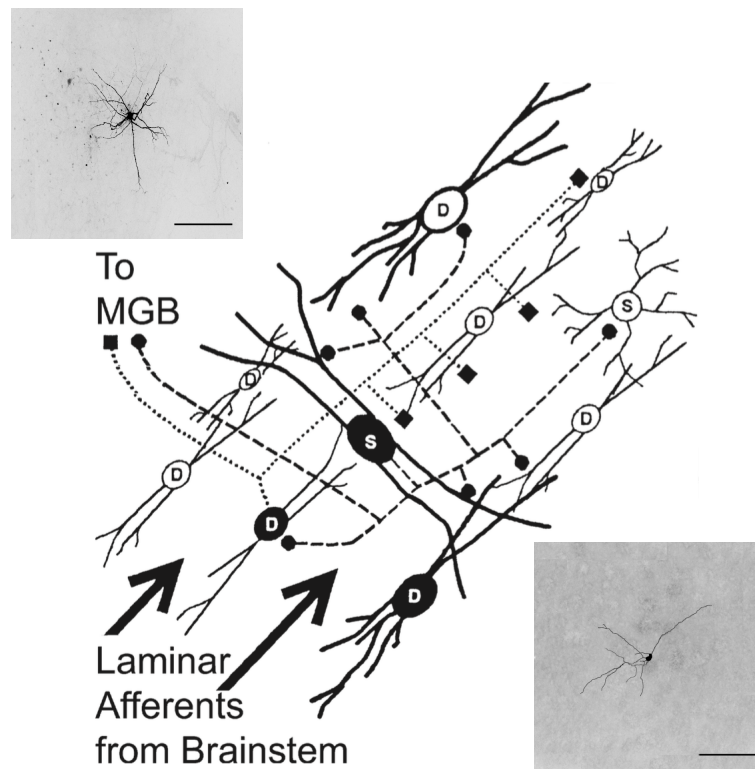


Figure 1.2: Principal types of neurons and fibrodendritic lamina within ICc. Example of a stellate neuron (upper left), example of a disc-shaped neuron (lower right), and schema of the fibro-dendritic laminae (center of figure), which are organized by the dendrites of disc-shaped neurons (D) running parallel to the afferent and efferent axons, and perpendicular to the dendritic field of the stellate neuron (S) (Center Figure from Oliver, 2005, reprinted with permission of Springer Science+Business Media, Inc.).

around $5\ \mu\text{m}$ in diameter and always have collaterals with $1 - 2\ \mu\text{m}$ in diameter in cats (Rockel and Jones, 1973b; Oliver et al., 1991).

Stellate neurons (Figure 1.2 top left inset) have a polyhedral soma of around $50\ \mu\text{m}$ in diameter with 5–6 stem dendrites (Rockel and Jones, 1973b). The dendritic fields of stellate neurons are spherical, spanning in three dimensions. The longest axes are up to $800\ \mu\text{m}$ (Rockel and Jones, 1973b) with some variations between species (cat, Rockel and Jones 1973b; Oliver et al. 1991; monkey, FitzPatrick 1975; human, Geniec and Morest 1971). The dendrites

of stellate neurons have a variable concentration of spines (Rockel and Jones, 1973b). Stellate neurons usually have large axons arising from the soma with a diameter of 5 μm in cats (Rockel and Jones, 1973b).

In addition to disc-shaped and stellate neurons that are located in the center area of the IC, there are other small bipolar neurons, multipolar neurons and large multipolar stellate neurons existing on the surface of the IC (Mylius et al., 2013). The arrangement of such neurons will be introduced in Section 1.2.2.

1.2.2 Connection between Neurons and Fibro-dendritic

Laminae

As shown in the center of Figure 1.2, soma, dendritic fields and axons of neurons have been reported to be organized in parallel to each other, which leads to a special morphological structure called the *fibro-dendritic laminae* (Rockel and Jones, 1973b; Malmierca et al., 1993). The laminae are around 150–200 μm in width and run from ventrolateral to dorsomedial and span rostrocaudally (Zook and Casseday, 1985; Malmierca et al., 1993; Mylius et al., 2013).

Confined within the lamina, the soma of the neurons are lying closely adjacent to each other and are stacking up end-to-end (Rockel and Jones, 1973b). The longest axes of the dendritic fields of the disc-shaped neurons are overlapping with each other, with the longest axes in parallel. The axons of the disc-shaped neurons, as well as the afferent axons from the lower brain stem, run also in the same direction (Rockel and Jones, 1973b; Schreiner and Winer, 2005; Malmierca et al., 1993).

The connections of components within a lamina are called *intralaminar con-*

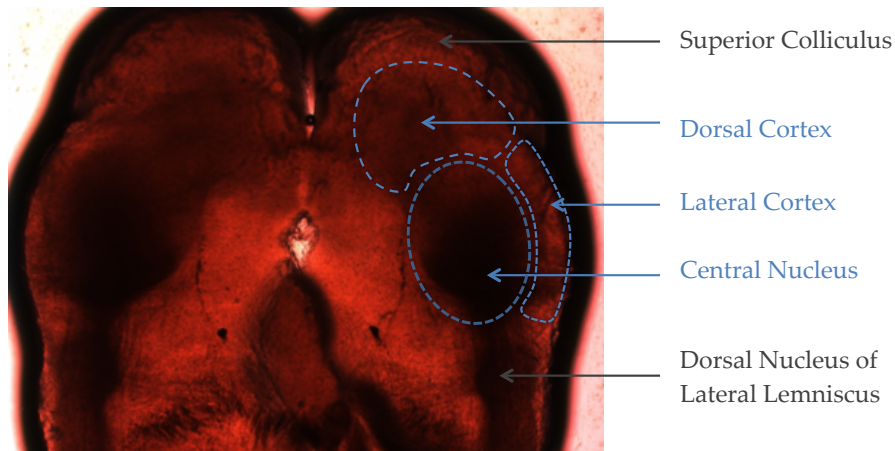


Figure 1.3: Three main subdivisions of IC. Three main subdivisions of the IC (noted in blue) shown on a slice at the cutting depth used in this thesis: the central nucleus (ICc), the dorsal cortex (ICd) and the lateral cortex (ICx) of the inferior colliculus. The SC and the VNLL (noted in gray) are located dorsal and ventral of the ICc, respectively.

nections (Oliver, 2005). Connections that reach between laminae are called *interlaminar connections* (Cant and Benson, 2008; Oliver, 2005; Malmierca et al., 1993). These are usually built from the dendritic fields and the axons of the stellate neurons, which are oriented perpendicular to the fibro-dendritic laminae (Malmierca et al., 1993).

1.2.3 Subdivisions

The boundary of the area with fibro-dendritic laminae is used to define the morphological subdivision of the central nucleus of inferior colliculus (ICc) (Morest and Oliver, 1984; Mylius et al., 2014) (Fig. 1.3). The area partially surrounding the ICc dorsally and laterally can be further divided into the dorsal cortex of the inferior colliculus (ICd) and the external cortex of the inferior colliculus (ICx) (Geniec and Morest, 1971; Rockel and Jones, 1973b; Meininger et al., 1986; Mylius et al., 2014) (Fig. 1.3).

Both ICd and ICx have their neurons organized in three layers (Mylius et al., 2014). The superficial layers of ICd and ICx are continuous and contain mainly small cells with the ICx mostly being comprised of small bipolar neurons (e.g. Mylius et al., 2014). The middle layers of both regions contain small to medium-sized neurons, and there are mostly multipolar neurons in the ICd in this layer (eg Mylius et al., 2014). The third layer of both regions occupies almost two thirds of both regions and is therefore the largest of all three layers. It contains small, medium and large size neurons. Some cells of the third layer in the ICd have a triangular soma as well as basal and apical dendrites that resemble neocortical pyramidal cells (Morest and Oliver, 1984; Oliver, 2005; Mylius et al., 2014). The border of ICd and ICx can be demarcated between layers two and three of both regions, because cells in the ICx are generally larger and slightly more loosely packed than in the ICd (Mylius et al., 2014).

1.2.4 Connections between IC Subdivisions

The three morphological subdivisions, ICc, ICd and ICx are not isolated. There are two types of connections within the IC: The interconnections among the three subdivisions of the IC of one hemisphere are called local or *intrinsic connections* (Schreiner and Winer, 2005), whereas the interconnections between two hemispheres of the IC are referred to as *commissural connections* (see Fig. 1.6) (Saldana and Merchan, 1992) . The intra- and interlaminar connections within the ICc, which were introduced in Section 1.2.4, are the most basic form of intrinsic connections (Schreiner and Winer, 2005). Intrinsic connections between the subdivisions had been clearly demonstrated in a 3-dimensional reconstruction of fiber plexuses of intrinsic CN axons at three

characteristic frequencies (CFs) in Guinea pig by Malmierca et al. (1995).

The projections originating from the ICc have been studied by injecting anterograde tracer into a discrete deposit of the ICc. With this method, two ipsilateral axon plexuses have been found. The main plexus runs dorsomedially and ventrolaterally along the fibro-dendritic laminae of the ICc and extends into the ICd (Gonzalez Hernandez et al., 1986; Saldana and Merchan, 1992; Frisina et al., 1997; Caspary et al., 1995; Saint Marie, 1996; Malmierca et al., 1995). Another external plexus runs laterally into the ICx, which is narrower than the first and is nearly parallel to the surface of the nucleus. (Saldana and Merchan, 1992).

The same method of injecting anterograde tracer can also be used to measure the projections from ICd and ICx. The ICd has a projection pattern that is remarkably similar to that of injecting into the ICc, which emphasizes the connective similarities between ICc and ICd (Saldana and Merchan, 1992; Saldana et al., 1996). In contrast, the ICx innervates preferably the peripheral regions of the IC, so the significant projections from ICx are less or absent (Kudo and Niimi, 1980; Saldana et al., 1996; Chernock and Winer, 2003; Schreiner and Winer, 2005).

1.2.5 Functional Domains build from Afferent Inputs

Besides the previously stated intrinsic neuronal organization, there are also neuronal organizations that are formed from the outside of the IC by the segregation of inputs from different sources. These organizations are called functional or *synaptic domains* (Oliver, 2005). The neurons in a synaptic domain share a similar function. In the ICc, a single lamina may actually be

composed of two or more synaptic domains (Oliver, 2005).

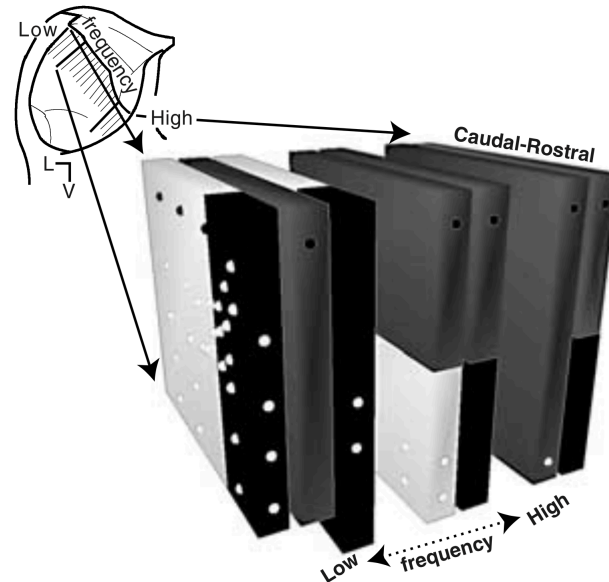


Figure 1.4: Schema of an ICc synaptic domain model. Different excitatory afferent auditory inputs are shown in light gray shade (MSO), dark gray shade (CN) and black (LSO). Different inhibitory auditory afferent inputs are marked with white spheres (LSO) and black spheres (DNLL) (From Oliver, 2005, reprinted with permission of Springer Science+Business Media, Inc).

The CN projects to the contralateral IC with axons terminating throughout the ICc. Projections from the DCN and the VCN appear to overlap almost completely, whereas CN projections to the ipsilateral IC are largely restricted to the dorsal (low-frequency) part of the ICc (Cant and Benson, 2008) (Fig. 1.4). The MSO sends projections to the ipsilateral ICc mostly for low and medium frequencies and builds functional domains (Oliver et al., 2003), and the high frequency region is devoid of any MSO projections (Oliver, 2005). The projections from the LSO to contralateral of the ICc spanning rostro-caudally are terminating side-by-side with the projections from the ipsilateral LSO in cats (Oliver et al., 1997) (Fig. 1.4). The DNLL sends bilateral projections from the

outer margin of the DNLL into the high- and from its inner center into the low frequency regions in the ICc (Kelly et al., 1998). The VNLL sends ipsilateral projections to the low frequency regions of the ICc banded, but to the high frequency regions more evenly distributed (Kelly et al., 1998). The AC sends corticofugal projections mainly through the MGB to the ipsilateral ICc, dorsal part of the ICc and also to the ICd (Bajo et al., 2007) (Fig. 1.4).

1.3 Electrophysiological Properties

Similar to the anatomical neuronal organization being the foundation for the description of principle functions, electrophysiological studies are fundamental in order to interpret functional roles. The electrophysiological properties related to this work will be introduced here beginning from basic individual neuronal properties to larger-scale properties and from *in vitro* to *in vivo*.

1.3.1 Membrane Properties

The basic electrophysiological properties of single neurons are the passive membrane properties, which consist of the membrane capacitance, the membrane resistance, and the membrane time constant. These properties are usually studied *in vitro*.

Studies have shown that in whole cell recordings *in vitro* at biological temperature, the average range of input resistance of IC neurons is between 239 and 644 M Ω in rats (Sivaramakrishnan and Oliver, 2001), between 38 and 237 M Ω in gerbils (Koch and Grothe, 2003; Yassin et al., 2015), and is between 170 and 235 M Ω at room temperature in mice (Basta and Vater, 2003). The

average range of the neuron's effective capacitance is between 65 and 140 pA (Sivaramakrishnan and Oliver, 2001; Yassin et al., 2015). The membrane time constant of IC neurons is 1.8–14 ms in intracellular recording (Wagner, 1994; Basta and Vater, 2003; Reetz and Ehret, 1999) resembling that of many auditory brain stem neurons (Hirsch and Oertel, 1988; Franzen et al., 2015).

1.3.2 Neuronal Firing Patterns

By injecting current into neurons, different neuronal firing patterns can be observed (Fig. 1.5). There are three major electrophysiological classifications of inferior colliculus (IC) neurons with respect to firing patterns: onset, sustain and adapting (Xie et al., 2008). Additionally, rebound spike patterns can exist for each firing pattern after cell hyperpolarization (Wu, 2005). Furthermore, other types of firing patterns, e.g. buildup-pause (Wu, 2005), rebound-adapting and rebound-transient (Sivaramakrishnan and Oliver, 2001) were found in different researches.

It has been shown that the classification of cell types based on their firing pattern does not correspond to the simple disc-shape or stellate morphological classifications (Bal et al., 2002; Peruzzi et al., 2000). However, the firing pattern might be related to other morphological features, e.g. dendritic branching patterns, size or the incidence of spines (Peruzzi et al., 2000; Oliver, 2005).

1.3.3 Characteristic Frequency and Tonotopic Structure

Another very important property of an auditory neuron is its characteristic frequency, which is measured in electrophysiological experiments in vivo (Merzenich and Reid, 1974; Malmierca et al., 2008; Langner and Schreiner,

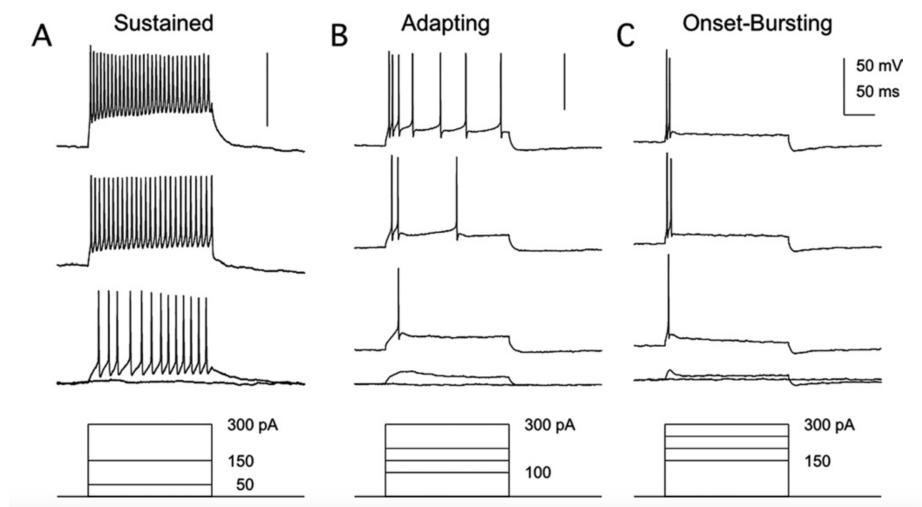


Figure 1.5: Main firing Patterns of inferior colliculus (IC) neurons. Neurons show three main firing patterns (three upper rows) when evoked by different depolarizing current injections (lowest row): **A**) sustained neuron, **B**) adapting neuron, **C**) onset neuron (From Xie et al., 2008, reprinted with permission of Elsevier Limited).

1988). The characteristic frequency (CF) refers to the frequency producing a response at the lowest sound pressure level, i.e. the lowest intensity (Ehret and Schreiner, 2005). Electrophysiological studies of responses of single or multiple units to pure tones have revealed that the best frequencies of neurons are organized tonotopically within the IC (Fig. 1.6), i.e. in topologically neighboring regions (Merzenich and Reid, 1974; FitzPatrick, 1975; Roth et al., 1978; Semple and Aitkin, 1979; Stiebler and Ehret, 1985; Casseday and Covey, 1992; Brückner and Rübsamen, 1995; Schreiner and Langner, 1997).

The tonotopy of the ICc consists of two frequency gradients (Schreiner and Langner, 1997; Ehret and Schreiner, 2005): a gradient with systematic frequency discontinuities along the main tonotopic axis from low frequencies in the dorso-lateral ICc to high frequencies located in the ventro-medial ICc, and a shallow continuous gradient within the isofrequency sheets (Schreiner and Langner, 1997). The latter has CFs that are low dorsomedially and higher

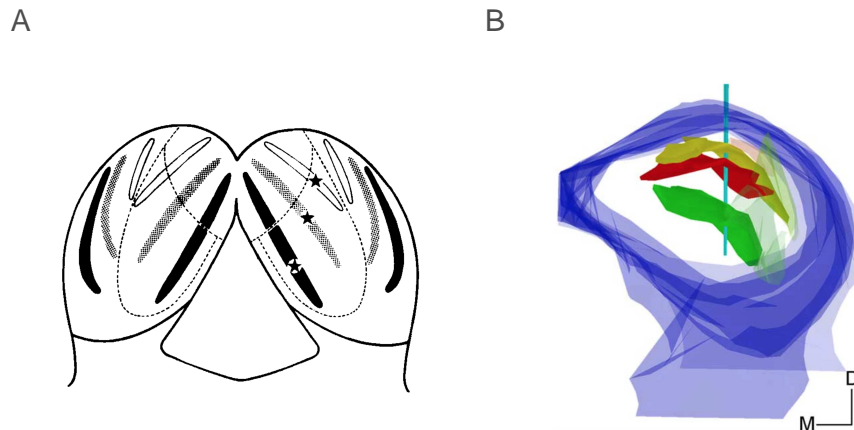


Figure 1.6: Tonotopic structure of the IC. Schema (A) and 3-dimensional reconstruction (B) illustrate the tonotopic structure of the IC. High frequency bands are shown as black areas in (A) and as green band in (B). Medium frequency bands are shown as grey areas in (A) and as red band in (B). Low frequency bands are shown as white area in (A) and as yellow band in (B). Moreover, Schema (A) shows that the intrinsic connections interconnect the main subdivisions IC within one hemisphere and the commissural connections interconnecting two hemispheres of IC arranging in a mirror-like manner. (Figure A. from Saldana and Merchan, 1992, reprinted with permission of John Wiley and Sons and Figure B. from Malmierca et al., 1995, reprinted with permission of Society for Neuroscience).

CFs laterally and ventrolaterally. The frequency range covered within an isofrequency sheet is about one critical band (Langner and Schreiner, 1988; Schreiner and Langner, 1988, 1997).

The ICd and ICx also have their own tonotopic arrangement (Aitkin and Boyd, 1978; Clopton and Winfield, 1973; Kitzes, 1984; Oertel et al., 2002). In the ICx, the frequency gradient decreases from lateral to medial in the cat (Hind et al., 1963; Roth et al., 1978) but increases in the mouse (Stiebler and Ehret, 1985). Different to the tonotopy of the ICc, the frequency range of the ICx is incomplete with the high frequency part being absent or underrepresented (Stiebler and Ehret, 1985; Romand and Ehret, 1990). The frequency gradient of the ICd runs from dorsal to the ventral border of the ICc (Merzenich and Reid, 1974; Serviere et al., 1984).

1.4 Intrinsic Synaptic Connections and Motivation of the work

Until today, a lot of studies have been conducted on the anatomical neuronal organization (e.g. Mylius et al., 2014) and electrophysiological properties (e.g. Loftus et al., 2008) of the inferior colliculus (IC), but less effort has been made to study intrinsic synaptic connections, which pervasively exist in the IC, and are necessary to understand the functional role of the IC.

1.4.1 Indication of Intrinsic Synaptic Connections

Electrophysiological and imaging studies have shown the pervasive existence of intrinsic networks in the ICc (e.g. Saldana et al., 1996; Oliver et al., 1991). One type of studies has suggested the existence of intrinsic networks based on observable dense intracollicular connections, which have been measured by injecting anterograde tracer into the ICc (Saldana and Merchan, 1992; Saldana et al., 1996; Malmierca et al., 1995). Further cellular studies have shown that the existence of local axon collaterals in the IC is the rule rather than the exception (Oliver et al., 1991; Rockel and Jones, 1973c,b; Herrera et al., 1988a,b, 1989; Gonzalez-Hernandez et al., 1989; Smith, 1992; Wagner, 1994, 1996; Reetz and Ehret, 1999; Peruzzi et al., 2000).

1.4.2 Relationship between Anatomical Organization, Tonotopy and Intrinsic Synaptic Connection

As we understand so far, the observable cells, i.e. dendrites, axons of the cells and the fibro-dendritic laminae in the ICc, etc., are the basic anatomical ele-

ments of neuronal circuits. The intrinsic synaptic connection, i.e. the intrinsic networks, are functional micro-circuits built from these elements. Further, the tonotopy is a functional macro-organization consisting of these micro-circuits.

In the central auditory system, tonotopy is a general functional organization, which can be found at almost every stage (Nieuwenhuys et al., 2007). This means that all nuclei in the auditory system are tonotopically organized, even though each of the nuclei has a different task (Ehret, 1997). For example, both the CN and the SOC are tonotopically organized; however, the CN is responsible for generating basic response patterns and the emergence of parallel pathways, whereas the SOC is responsible for binaural information processing. Even within a nucleus, different subdivisions can have different anatomical organizations, but they are then generally also tonotopically arranged (Winer and Schreiner, 2005). For example both the DCN and the VCN are tonotopically arranged; however, the DCN is reported to have an anatomical laminar structure, whereas in the VCN there is no laminar structure reported (Mylius et al., 2013). This indicates that the intrinsic synaptic connections, i.e. the microscopic intrinsic network, is generally different for each nucleus and even for different subdivisions of one nucleus.

So one exciting question is how the intrinsic synaptic connections are arranged based on different anatomical organizations, so that the tonotopic organizations are created generally within the different functions of different nuclei?

Especially in the IC, experiments have indicated that the morphological foundations, i.e. the fibro-dendritic laminae, and the functional macro-organization, i.e. the tonotopy, have a similar, band-like appearance. They run both

from the ventro-lateral to dorso-medial direction and have similar spacing between the bands (Rockel and Jones, 1973b; Malmierca et al., 1993; Schreiner and Langner, 1997; Ehret and Schreiner, 2005). Besides, the fact that both tonotopy and the fibro-dendritic laminae extend into the ICd is also an indication for the relation between the two structures (Gonzalez Hernandez et al., 1986; Saldana and Merchan, 1992; Malmierca et al., 1995; Bajo et al., 2007). So the question is, do the functional micro-organizations, i.e. the synaptic intrinsic connections of the ICc, also have a similar appearance? Do they happen to be band-like, too? Moreover, ICc and ICx are organized anatomically different, so how do the synaptic intrinsic connections in ICc and ICx differ from each other?

1.4.3 State of the Art

There are a few studies that tried to answer the questions: how does the appearance of the functional micro-organization of the IC, i.e. the intrinsic synaptic network look like? And from where do the synaptic inputs come from, and how strong are these connections?

Two recent studies (Chen et al., 2012; Mei et al., 2013) have made approaches to explore the functional micro-organization through their functional micro-circuit, by measuring the functional correlations and interaction of simultaneously recorded IC neurons, i.e. paired neurons, in response to sound stimulation. Chen et al. (2012) have analyzed the spectral and temporal responses of paired neurons detected by a four-tetrode array, and have reported similar preferences of neighbouring neurons, while the neurons recorded across distant sites have been less similar (Chen et al., 2012). Mei et al. (2013) further have studied paired neurons recorded with a pair of electrodes using a two-tone stimulation paradigm. They have reported that a pair of neurons stimulated by their two best frequency tones have been responding either both inhibited (two tone suppression) or both facilitated (two tone facilitation). Further, they have applied bicuculline (an antagonist of the GABA_A receptor) to one neuron of the pair in order to study the mechanism underlying the effect of two tone suppression. They have reported a response facilitation in the neuron under bicuculline application, but stronger response suppression of the paired neuron.

The collective appearance of IC neurons has been studied by Chandrasekaran et al. (2013), who have used optical imaging with voltage-sensitive dyes to investigate the spatio-temporal dynamic of synaptically evoked activities in

brain slices of the IC. They have observed LL-driven spatio-temporal activities in the IC slice and have found that the strong spatio-temporal propagation occurred in the direction of the fibro-dendritic laminae.

In contrast, the cross-laminar propagation appeared to be much weaker, which has been suggested to be a consequence of lemniscal inputs with amplified by local circuits. Further, the DNLL has been stimulated with different stimulation patterns in order to observe the propagation and local variations of the responses. By using stimulations of small frequencies, they have observed first a local response, which could then propagate along the fibro-dendritic laminae by increasing the stimulation frequencies. This observation has indicated that the propagation of the responses have been amplified by local circuits. By using a long stimulus train with a low current strength likewise, they have observed the oscillation between excitatory and inhibitory activities, which suggested local circuits specific to inhibitory post-synaptic rebound neurons. However, due to the low resolution resulting from the low-power objective, the intrinsic synaptic connections of single cells have not been resolvable.

Recently, Sturm et al. (2014) have used laser-scanning photo-stimulation with caged glutamate to characterize the spatial distribution and strength of the local synaptic connections of the ICc neuron, with a focus on the development of the intrinsic network (P2–P22). They have shown the presence of an extensive excitatory and inhibitory intrinsic network already at P2, which has underwent an expansion in the first week, followed by a refinement after hearing onset. Besides, they have found that excitatory and inhibitory synaptic maps to individual IC neurons have formed continuous maps that largely

overlapped with each other, and that have been aligned with the presumed isofrequency axis of the central nucleus of the ICc solely. However, it has not been shown how the intrinsic maps are different according to the locations of the cells in the ICc. The intrinsic maps of the two other subdivisions of the IC, i.e. the ICc and the ICx, have not yet been studied.

1.4.4 Contribution of this Work

In our work we answered the previously stated questions using laser scanning photostimulation (Dantzker and Callaway, 2000; Callaway, 2002; Kötter et al., 2005; Bendels et al., 2008; Sturm et al., 2014) of caged glutamate activated neurons to acquire the synaptic inputs of neurons in different regions of the ICc and also in the ICx. Our approach specifically aimed to study not only the intrinsic innervations and their regional differences, but also to find the correlations of intrinsic innervation with electrophysiological and morphological parameters.

We were the first to find that in case of excitation, ICc cells had two preferred intrinsic innervation orientations. Not only did the innervation follow the direction of the isofrequency axis (Sturm et al., 2014), but also a second innervation direction existed that ran along the tonotopic axis and was connecting a wider range of isofrequency sheets. Likewise, the inhibitory innervation of ICc cells had no sole preferred direction as shown in Sturm et al. (2014), but was rather dispersed in different directions.

Furthermore, we were the first to study the organization of intrinsic inputs of the ICx as well. We found that in case of excitation, ICx cells had a sole preferred orientation that ran, unlike ICc cells, in a direction along the outer

boundary of the IC. The inhibitory innervation of ICx cells was, however, similar as for ICc cells, also dispersed in all direction. The orientations of the intrinsic innervations of ICc and ICx cells were further described in Section 3.2.4.1.

In addition, we found that the intrinsic innervations of IC cells were regionally heterogeneous in their excitation-inhibition ratio. Whereas cells in the dorso-medial ICc had a balanced intrinsic excitation and inhibition, excitation was prevalent in the ventro-lateral ICc and in the ICx.

More regional heterogeneity was also found in the amount of excitatory and inhibitory inputs by comparing paired regions. In particular, we found that in the lateral ICc, there existed a narrow region spanning along the outer boundary of ICc cells that had the weakest excitation, which was significantly different than in the adjacent region the ICx. Besides, ICx neurons were also different compared to ICc neurons in that they received larger amount of excitatory inputs. The regional heterogeneity of intrinsic inputs were described in Section 3.2.4.2.

Moreover, we analyzed the correlations of intrinsic innervation with electrophysiological and morphological parameters. We found that the intrinsic excitatory innervation was related with the apparent surface of the cells, and that the intrinsic inhibitory innervation was related to the membrane conductance of the cells (see Section 3.2.3).

As a consequence, the dorso-medial ICc cells varied most in the amount of inhibitory inputs, i.e. the membrane conductance, whereas the ICx cells were most similar in the amount of inhibitory inputs and membrane conductance respectively. In contrast, the lateral ICc cells were more similar in their cells

surface size compared to cells in the rest of the ICc (see Section 3.2.4.2).

2 Material and Methods

2.1 Slice Preparation

All experiments in this PhD thesis complied with institutional guidelines, national and regional laws. In the experiments, Mongolian gerbils (*Meriones unguiculatus*) of postnatal day 14–16 (P14–P16) were used. In order to prepare the acute slice, animals were anesthetized and decapitated. The brain tissues were moved into ice-cold slicing solution, which was pre-bubbled with 95% O₂ and 5% CO₂ (pH 7.4). The slicing solution contained (in μM) 50 sucrose, 25 NaCl, 25 NaHCO₃, 2.5 KCl, 1.25 NaH₂PO₄, 6 MgCl₂, 0.1 CaCl₂, 25 glucose, 0.4 ascorbic acid, 3 myo-inositol and 2 Na-pyruvate.

Two adjacent transversal IC slices with a thickness of 300 μm were cut with a VT1200S vibratome (Leica, Wetzlar, Germany). Only the adjacent surfaces of the slices were used in order to preserve the consistency and comparability of the presynaptic input maps. The surfaces used for the presynaptic inputs experiments were around 450–500 μm to the caudal boundary of the IC. For all experiments, the dissection direction of the slice was 60° to the horizontal surface with the exception of the presynaptic inputs experiments for comparison, in which the dissection direction was orthogonal to the horizontal

surface. All slicing processes were confined within 15 minutes in order to preserve the vitality of the slices. The slices were incubated at 37°C in the recording solution containing (in μM) 125 NaCl, 25 NaHCO₃, 2.5 KCl, 1.25 NaH₂PO₄, 1 MgCl₂, 2 CaCl₂, 25 glucose, 0.4 ascorbic acid, 3 myo-inositol and 2 Na-pyruvate and incubated for 15 minutes. Afterwards, the slices were incubated at room temperature for at least 45 minutes before being used. All solutions were bubbled with 95 % O₂ and 5 % CO₂.

2.2 Setup

The setup shown in Figure 2.1 had three principal components: a laser system that served for stimulation, a microscope that served for the observation of a recorded neuron and an amplifier for signal recording.

The laser stimulation system (DPSL 355/1000 Rapp Optoelectronic, Germany) contained a diode pumped solid state ultraviolet (UV) laser generator (ND:YVO₄, DPSS laser, Santa Clara, CA, USA), which generated laser pulses with a wavelength of 355 nm and a pulse length of 70 ns. The laser equipment had an average power of 1000 mW at 100 kHz. The laser pulses were modulated and shuttered by an acousto-optic modulator, then guided through a 50 μm quartz light guide and entered the microscope through a mounted spot illumination adaptor (OSI-BX, Rapp Optoelektronik, Wedel, Germany).

The laser beam was focused on the specimen in a recording chamber on the XYZ-shifting table (L&N 380FM-U) of the microscope; the focus point was 30–50 μm under the surface. The patch clamp electrode was fixed to the shifting table so that there was theoretically no relative movement between the specimen and the electrode. This setup produced a spot size with an

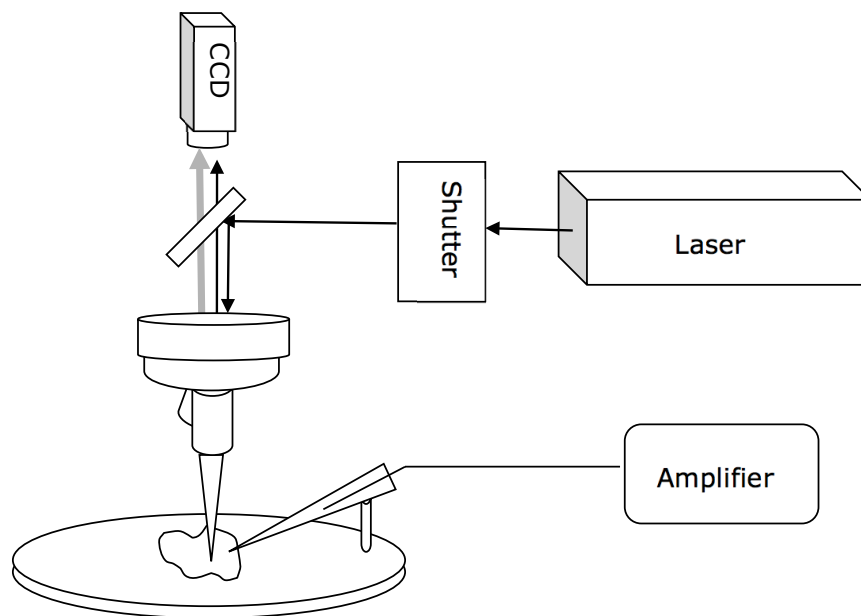


Figure 2.1: Setup and the light pathway. UV light was generated and modulated by a diode pumped solid state laser generator and passed through a shutter, then focused on a probe by an objective. The probe was mounted on a recording chamber located on a XYZ shifting table. A cell in the probe was patched and recorded by an amplifier, while the cell was observed by a CCD camera, which was used while setting the stimulation sites as well. (Figure based on Bendels et al., 2008).

approximate diameter of 3–4 μm .

An upright light microscope (BX51W1, Olympus, Hamburg Germany) was mounted with a halogen light source (Luigs und Neumann, Ratingen, Germany) and a gradient contrast illumination system (Luigs und Neumann, Ratingen, Germany) in order to take the bright field images, and a mercury lamp (X-cite 120, Lumen Dynamics, Mississauga, Canada) together with a quick light shutter (U-FSHA) were mounted in order to take fluorescence images. Images were taken by a IR-CCD camera (VX 55,FEI, Gräfelfing, Germany).

An EPC 10/2 amplifier (HEKA Elektronik, Lambrecht, Germany) was used for the electrophysiological recording. Analog signals acquired by the patch electrode were digitized with a sampling rate of 20 kHz.

The above described setup (also see Figure 2.1) was under control of a custom-made software Morgentau (Morgentau Solutions, Germany), which allowed to define the scanning area, sequence, coordination, stimulation duration and stimulation interval. A detailed description of the generation of the commands and communication between the equipment can be found in Bendels et al. (2008).

2.3 Electrophysiology and UV Uncaging

Five types of experiments were performed in this PhD thesis: the electrophysiological cell characterization (CC) experiments, the miniature postsynaptic current (mPSC) experiments, the effective spot size (ESS) experiments, the scanning resolution (SR) calibration experiments and the pre-synaptic inputs experiments. The former two were pre-experiments, which were performed

solely using the patch clamp without uncaging. The next two calibration experiments, together with the pre-synaptic inputs experiments, were UV-uncaging experiments combining the patch clamp technique with laser stimulation.

All experiments were performed at room temperature. The slices were incubated in recording solution bubbled with 95 % O₂ and 5 % CO₂ before. Then, the slices were cut in half along their medial line, and transferred subsequently into a recording chamber settled on the shifting table (L&N 380FM-U) of the microscope and continuously supplied with bubbled recording solution conjugated with or without pharmacological drugs depending on the experiments. Unless otherwise stated, the general intracellular solution filled in the patch electrode contained (in μM) 145 K-gluconate, 15 HEPES, 3 KCl, 4 Mg₂-ATP, 0.3 Na₂-GTP, 5 Na₂-phosphocreatine, 5 K-EGTA, with 100 Alexa 568 and was adjusted to pH 7.2 by KOH. In current clamp mode, the bridge balance was adjusted to 100 %. In voltage clamp mode, cells were held at -60 mV and the access resistance was compensated to 2.5–3.5 M Ω .

In all UV-uncaging experiments, 10 ml recording solution conjugated with 0.25 μM MNI-caged-L-glutamate (MNI-Glu, Tocris) was recirculated and perfused into the recording chamber with a flow speed of 3–5 ml per minute throughout the experiment. The laser power used 0.25 W, and the duration of the laser stimulation was 4 ms. In all UV-uncaging experiments, stimulation of the neurons started at least after the slices being incubated in the recording solution containing the caged compounds for 25 minutes. The laser scanning time was confined within 70 minutes bath incubation time. By this means, there was enough time in order to scan the whole region of interest (ROI)

while preserving the vitality of the acute slices.

General Cell Characterization

The electrophysiological cell characterization experiments measured the spike train patterns, the rebound characteristics, the membrane capacitance, the input resistance, the membrane conductance, as well as the membrane time constant. The experiments were performed in current clamp mode. No additional pharmacological drugs were added in the intracellular and the recording solution. In order to acquire the spiking train patterns, stepwise increased currents with a duration of 500 ms were injected into the cell starting at -125 pA and increasing by 50 pA in each step. The current thresholds were determined by stepwise increased current injection of 2 ms duration starting at zero and increasing by 25 pA per step. The capacitance, the conductance and the decay time constant were determined by applying -7 pA pulse current injection for a duration of 600 ms (see Fig. 3.2).

Miniature Postsynaptic Current Characterization

The excitatory and inhibitory miniature postsynaptic currents (mEPSCs and mIPSCs) were characterized in voltage clamp mode separately with different pharmacological drugs. For this purpose, slices were put into the recording chamber continuously perfused with 10 ml pre-bubbled recording solution. Intracellular solution containing 130 Cs-gluconate, 10 Cs-HEPES, 20 TEA-Cl, 3.3 MgCl_2 , 2 Na_2 -ATP, 0.3 Na_2 -GTP, 3 Na_2 -phosphocreatine, 5 Cs-EGTA, 5 QX-314 and 100 Alexa 568 (in mM) was added. In the miniature excitatory postsynaptic currents (mEPSCs) experiments, the pharmacological drugs tetrodotoxin (TTX, 1 μM , Alomone) TEA, 4-Aminopyridine (4AP) (2 mM,

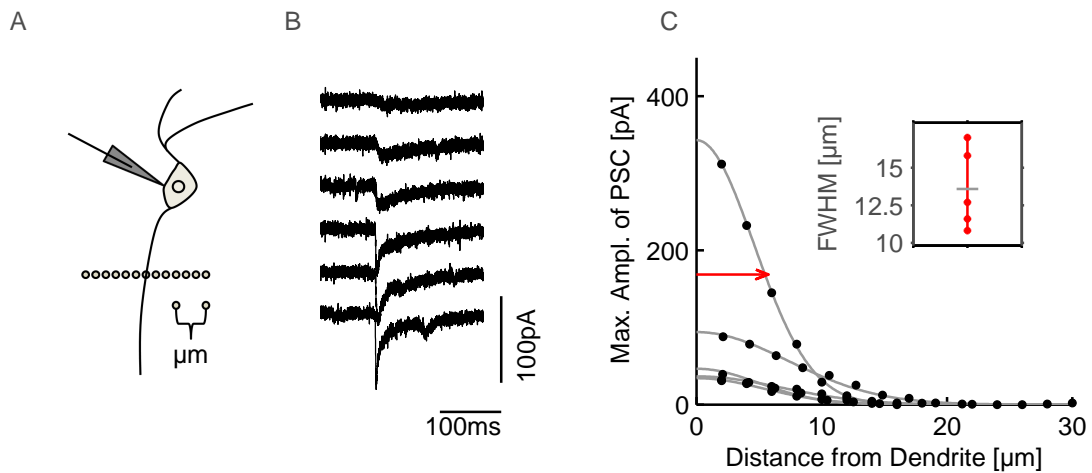


Figure 2.2: Effective spot size (ESS) calibration experiment. **A)** Schematic of experimental paradigm: Uncaging pulses were delivered in 2–3 μm steps successively along the stimulation sites. **B)** Examples of PSC raw traces arranged in accordance with the stimulation sites shown in (A). **C)** Peak responses to the uncaging pulses delivered at the stimulation sites as indicated in (A). Single traces are from $n=5$ cells. FWHM of one cell is shown as a red arrow. Inset shows the FWHM of all cells ($n=5$, red dots) and the average of FWHM (gray bar).

Sigma Aldrich), strychnine hydrochloride (STRY, 1 μM) and SR 95531 (10 mM, Tocris) were added in the extracellular recording solution, and in the mIPSC experiments, 6,7-dinitroquinoxaline-2,3-dione (DNQX) (20 μM , Tocris) and D-AP5 (50 μM , Tocris) were added in the recording solution. 10 s recordings were acquired in ten repetitions for each cell.

Effective Spot Size Calibration

The purpose of this UV uncaging experiment was to calibrate the distance to a dendrite where the applied laser stimulation could still evoke action potentials (APs). The experiments were performed in voltage clamp mode. The intracellular solution was used without any additional pharmacological drugs, and the extracellular solution was conjugated with strychnine hydrochloride (STRY) (1 μM , Sigma), SR95531 (Gabazine) (SR 95531) (10 μM , Biotrend),

and D-AP5 (50 μM , Toris) in order to get AMPA receptor (AMPA) mediated postsynaptic currents (PSCs). The stimulation sites were set on a line orthogonal to a tested dendrite, so that the intersection between the line and the dendrite was within a distance of 20–50 μm to the cell soma, and no other dendrites existed within the half hemisphere with a radius of 30 μm on the side of stimulation. By this means, the ESS of tested dendrites could be measured with neither influence of the soma nor other dendrites. Total five cells were measured with two repetitions for two cells and one repetition for three cells. The mean amplitudes of raw traces plotted against the distances to the dendrites are shown in Figure 2.2 C and are fitted with a Gaussian curve-fitting algorithm. The effective spot size of the dendrites was defined as the average FWHM of the fitted curves, i.e. $\sim 13.58 \pm 2.69 \mu\text{m}$.

Scanning Resolution Calibration

The purpose of this UV-uncaging experiment was to calibrate empirically the best combination of laser intensity and laser pulse duration to uncage the MNI-glutamate compounds while the cell retained its vitality (Figure 2.3). Consequently, it determined how far away from the cell soma that the applied stimulation could cause the cell to fire APs, i.e. the scanning resolution of the mapping inputs experiment. Thus, the SR measurements were performed under the same experimental conditions as the mapping input experiment except that pharmacological drugs were added into the extracellular solution, in order to isolate the patched neuron from the presynaptic inputs.

The SR experiments were performed in current clamp mode. The intracellular solution was without additional pharmacological drugs, and the extracellular solution was conjugated with STRY (1 μM , Sigma), SR 95531 (10 μM ,

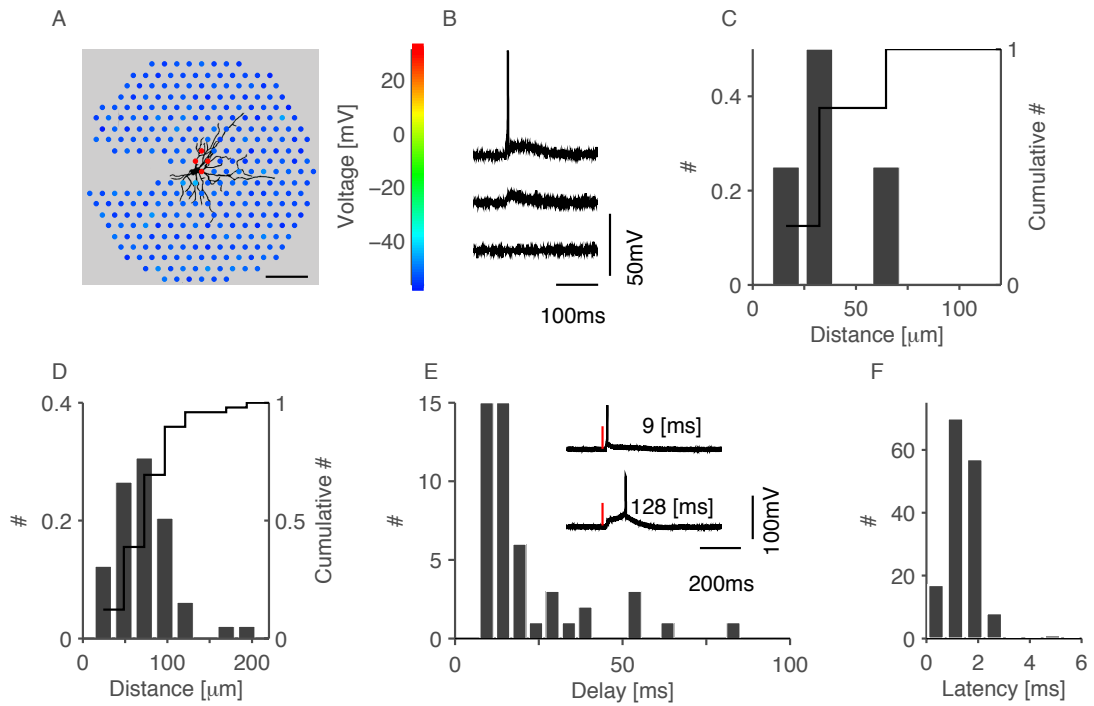


Figure 2.3: Scanning resolution (SR) calibration experiment: A) Example of a scanned neuron from the 3-D reconstruction superimposed with color-coded stimulation sites showing the voltage. Scale bar is 100 μm. **B)** Typical example traces without voltage response (Bottom, dark blue stimulation sites in A), with voltage response below the AP threshold (Middle, light blue stimulation sites in A) and with AP (Top, red stimulation sites in B). **C)** Normalized spike density histogram (left axis) and cumulative histogram (right axis) of example cells showing all spikes that are within a distance of 70 μm. **D)** Normalized spike density histogram (left axis) and cumulative histogram (right axis) of all cells (n=17) showing that 75% of APs occur within a distance of 100 μm. **E)** Histogram of spiking time of all APs showing that the peak of AP spiking delay time after stimulation is at 9.46 ms -19.28 ms. Insets: example traces show the smallest AP spiking time after stimulation at 9 ms, and the largest AP spiking time after stimulation at 128 ms. Red bar: Stimulation start. **F)** Histogram of all AP shows that the majority of latency to depolarization onsets is within 3 ms after stimulation, and the maximum values of the latencies to depolarization onsets are 6 ms.

Biotrend), D-AP5 (50 μM , Toris) in order to isolate AMPAR mediated PSCs. The stimulation area shown in Figure 2.4 A was set to a radius of 300–350 μm around the patched neuron, and the stimulation sites were set up in a hexagonal arrangement using the software Morgentau (Morgentau Solutions, Germany). The distance between the stimulation sites ideally should be equal to two times the effective spot size; however, the limited time available for scanning the whole ROI also had to be taken into account. Thus, a distance of 35 μm between the stimulation sites was used in both the SR experiments and the mapping input experiments with both the calibrated ESS and limited total experiment time allowed for photoscanning without cell toxicity (see Section 4.5)

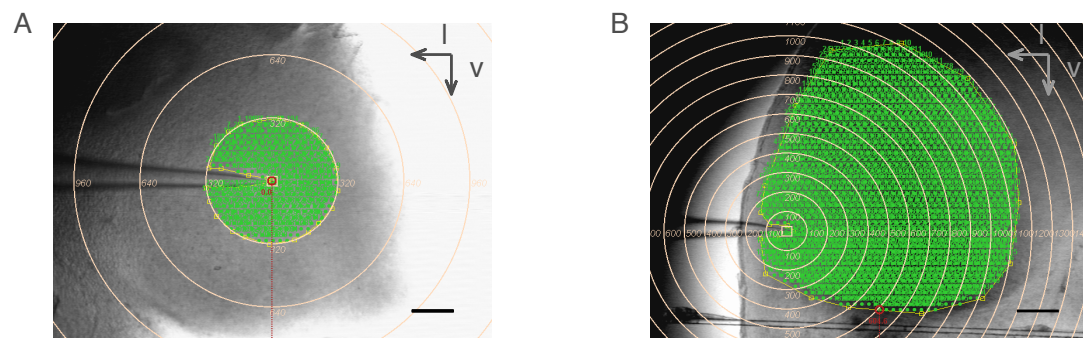


Figure 2.4: Stimulation layouts of SR and mapping input experiments. Layout of SR experiment (A) and mapping input experiments. (B). The distances between the rings are 100 μm . The white points on (B) are preset stimulation points with a distance of 35 μm . l:lateral, v:ventral. Scale bars = 200 μm .

Mapping Input Experiments

The mapping inputs experiment, whose fundamental working mechanism is shown in Figure 2.5 A, is an UV-uncaging experiment performed in voltage clamp mode. In order to detect both EPSC and IPSC inputs, no pharmacolog-

ical drugs were added in both the intracellular solution and the extracellular solution. Patched neurons were from a region of interest (ROI) that contained both the ICc and the lateral nuclei of the IC, which could be observed as a continuously darker area with higher cell density by visual inspection (Figure 2.4 B).

Thus, as shown in Figure 2.4 B, the boundaries of the ROI are defined ventrally using the natural ventral boundary of the IC, laterally using 100 μm distance to the lateral boundary of the slice and dorsally by eyeballing the dark boundary of the middle part of the IC to the dorsal IC cortex. The stimulation area was elliptical shape with a minor diameter of 900 – 1200 μm and a major diameter of 1200 – 1600 μm . The stimulation sites were set up in a hexagonal arrangement using the software Morgentau (Morgentau Solutions, Germany), and the distance between the stimulation sites was 35 μm .

2.4 Slice Fixation and Confocal Microscopy

Standard slice fixation procedures were carried out on free floating slices. Right after the experiment, the brain slices containing the patched neuron were moved into phosphate buffer saline (PBS) containing 4% paraformaldehyde, (0.1 mM Heparin and 155 mM NaCl and incubated for 24–48 h. Subsequently, the slices were washed with PBS for 10 minutes and mounted in Vectashield medium (Vector Laboratories Inc., AXXORA, Lörrach, Germany).

Fluorescence images of the slices and the neurons were taken with an Axiovert inverted microscope H-100 (Carl Zeiss, Germany) using 2.5x objective (0.075 NA) and 10x objective (0.25 NA), in order to determine the direction of the dendritic field of the cell as well as to determine the location of the

cell on the slice. Separately, neurons were confocally scanned with a Leica SP system (Leica, Wetzlar, Germany) using 25x objective (0.75 NA) in order to perform the morphological reconstruction. The scanning resolutions of the confocal image ranged from 0.7–1.516 μm per pixel. Additional fluorescence images were taken during experiments with a microscope (BX51W1, Olympus, Hamburg Germany) in order to control the cell orientation in the experiment.

2.5 Data Analysis

General Data Analysis Cell membrane parameters were analyzed in IGORpro (WaveMetrics Inc, Lake Oswego, OR, USA) and MATLAB (MathWorks, Natick, Massachusetts, USA). The miniature PSCs experiments were also analyzed in IGORpro (WaveMetrics Inc, Lake Oswego, OR, USA). Miniature excitatory presynaptic currents (EPSCs) were pre-extracted using a custom written template matching routine (Taschenberger et al., 2005; Couchman et al., 2010) and then filtered individually by observation. Confocal image stacks were processed with ImageJ. The dendritic field was defined as the area of the polygon connecting the distal ends of the visible dendrites (Fig. 3.3 A, left). The length of the dendritic field was taken as the longest diameter of the polygon, and the width of the dendritic field was measured by drawing a line orthogonal to the length of the dendritic field and intersecting with the center of the soma (Fig. 3.3 A, middle). The soma length and width were defined as the first and second axis of the soma ellipse (Fig. 3.3 A, right). The number of main dendrites was counted manually.

PSC Detection The excitatory and inhibitory postsynaptic currents (EPSCs and IPSCs, respectively) were detected by an iterative algorithm described by Bendels et al. (2008). The detection algorithm, as shown in Figure 2.5 B, is based on four criteria including the absolute peak amplitude (*larger than* criterion in pA), the maximum absolute slope of the rising part of the PSC (*faster than* criterion in pA/ms), the time-interval between the initiation of the PSC and its peak (*shorter than* criterion in ms) and the total amount of electric charge that is transported out of the cell (*negative* for EPSCs and *positive* for IPSCs) (Bendels et al., 2008). The criterion for EPSCs and IPSCs of each cell was adjusted individually based on visual inspection of the raw traces. The raw traces were initially filtered by a low-pass Butterworth filter at a cutoff frequency of 500 Hz (Kudoh and Taguchi, 2002). The time window of 7 ms used for the detection of direct synaptic inputs was based on the AP start times of the SR calibration experiment. The PSCs detection time window ended, when the EPSC rates dropped below three standard deviations above the average spontaneous EPSC rate, which is less than 81 ms according to Bendels et al. (2010). The spontaneous EPSC and IPSC rates were tested for each cell individually, using the the raw trace before stimulation.

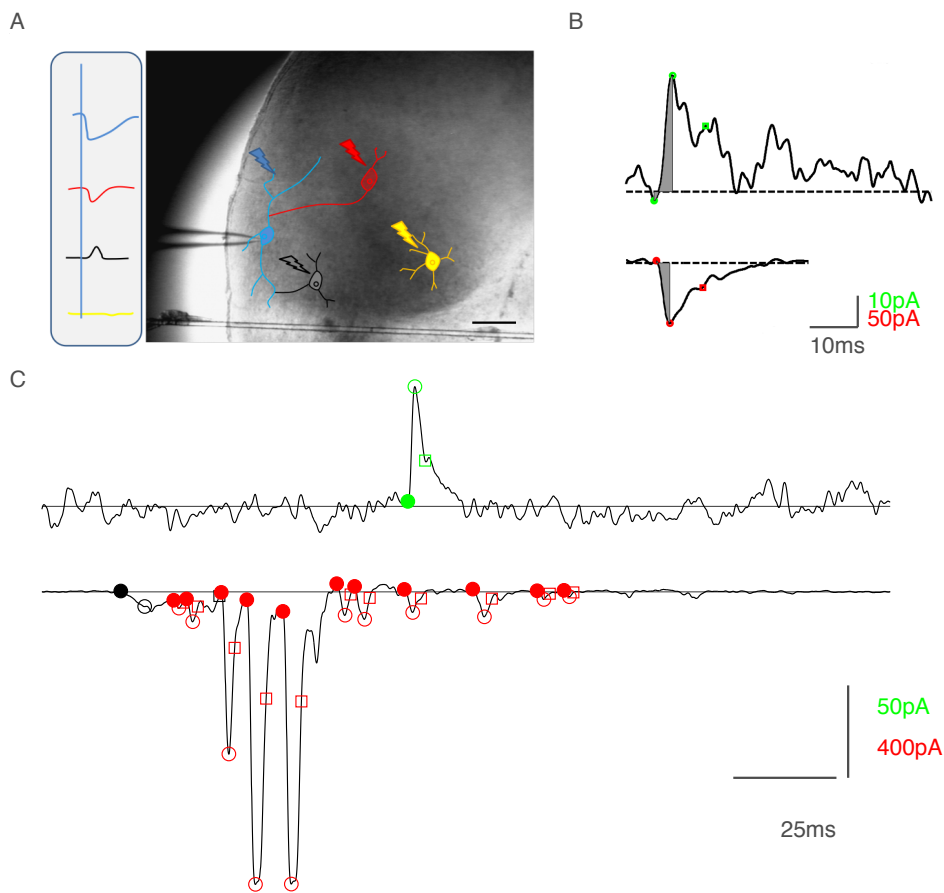


Figure 2.5: Working mechanism of uncaging experiment and PSC detection diagram. **A)** Working mechanism of the mapping inputs experiment. Cells (blue) were patched while the slice was simultaneously photo-stimulated, and the detected PSCs are shown in the left inset. If excitatory presynaptic cells (red) were stimulated, indirect EPSCs (inwards, red, left inset) can be detected by the patch clamp; if inhibitory presynaptic cells (black) were stimulated, indirect IPSCs (outwards, black, left inset) can be detected; if the patched cell (blue) was stimulated, direct PSCs (inwards, blue, left inset) can be detected. The direct PSCs have shorter latency from the stimulation start (same or less than 7 ms) in comparison to the indirect PSCs (larger than 7 ms). If the stimulated cells had no synaptic connections (yellow) with the patched cell (blue), no PSCs (yellow, left inset) can be detected. Scale bar = 200 μm . Diagrams (**B**) and trial examples (**C**) show the initiation times (points), the peaks (ring) and the decays (square) of the direct PSCs (black), the excitatory indirect PSCs (red) and the inhibitory indirect PSCs (green) that are detected based on four criteria: the absolute peak amplitude (*larger than*), the maximum absolute slope of the rising part of the EPSC (*shorter than*), the time interval between the initiation of the PSC (*shorter than*) and its peak and the total amount of electric charge that is transported into the cell (*negative* for EPSCs and *positive* for IPSCs). Horizontal black lines, baseline.

3 Results

In this work, we used the whole-cell patch clamp technique combined with laser scanning photostimulation of caged glutamate (Dantzker and Callaway, 2000; Callaway, 2002; Kötter et al., 2005; Bendels et al., 2008; Sturm et al., 2014) in order to determine the intrinsic structure of neurons from both the ICc and the ICx region in the Mongolian gerbil. The decision to target this specific area, which is hereinafter simply referred to as the *region of interest* (ROI), was motivated by our aim to study regional differences in the neuronal structure, but which was constrained by limitations in the feasible size of the scanning area for our setup at the same time.

Although the existence of both excitatory and inhibitory intrinsic innervation has been reported recently already in the ICc (Sturm et al., 2014), it has not been reported yet how the amount of excitatory and inhibitory inputs varies in different regions within the ICc and in the ICx.

3.1 General Cell Characterization

Beyond the intrinsic structure, we were also interested in analyzing how the intrinsic innervation maps potentially relate to the biophysiology of the cells. For this purpose, we determined a number of electrophysiological and mor-

phological cell parameters.

3.1.1 Electrophysiology

In a first step, we wanted to know the general electrophysiological parameters of the cells, i.e. firing pattern, cell membrane capacitance, membrane conductance, membrane time constant and current threshold of the AP, in order to find out whether certain intrinsic innervation parameters are correlated to the electrophysiology of the cell. For this purpose, each cell in every experiment was characterized at the beginning and, if possible, also at the end to validate the measured results. All 152 cells that were acquired throughout this thesis in the different experiments (except the miniature PSC experiments) were used for analysis of their electrophysiological parameters.

Further, 86 of these 152 cells, for which the location was available from the presynaptic inputs mapping experiment, were used to statistically analyze spatial correlations. Moreover, this subsample of 86 cells was also used to visualize these results by mapping them onto a standardized IC slice under self-fluorescence that was aligned with the ROI (e.g. Fig. 3.1 C1, D1, Fig. 3.2 D).

Firing Pattern

Neuronal firing patterns represent different combinations of specific potassium currents (Wu, 2005), which can be used to classify neurons into onset-bursting, adapting and sustained cells (Xie et al., 2008). The neuronal firing pattern of a cell can be acquired by injecting depolarizing/hyperpolarizing currents into it (Xie et al., 2008). The same as in previous studies (Peruzzi et al., 2000; Wu, 2005), we observed the three main firing patterns for cells from the

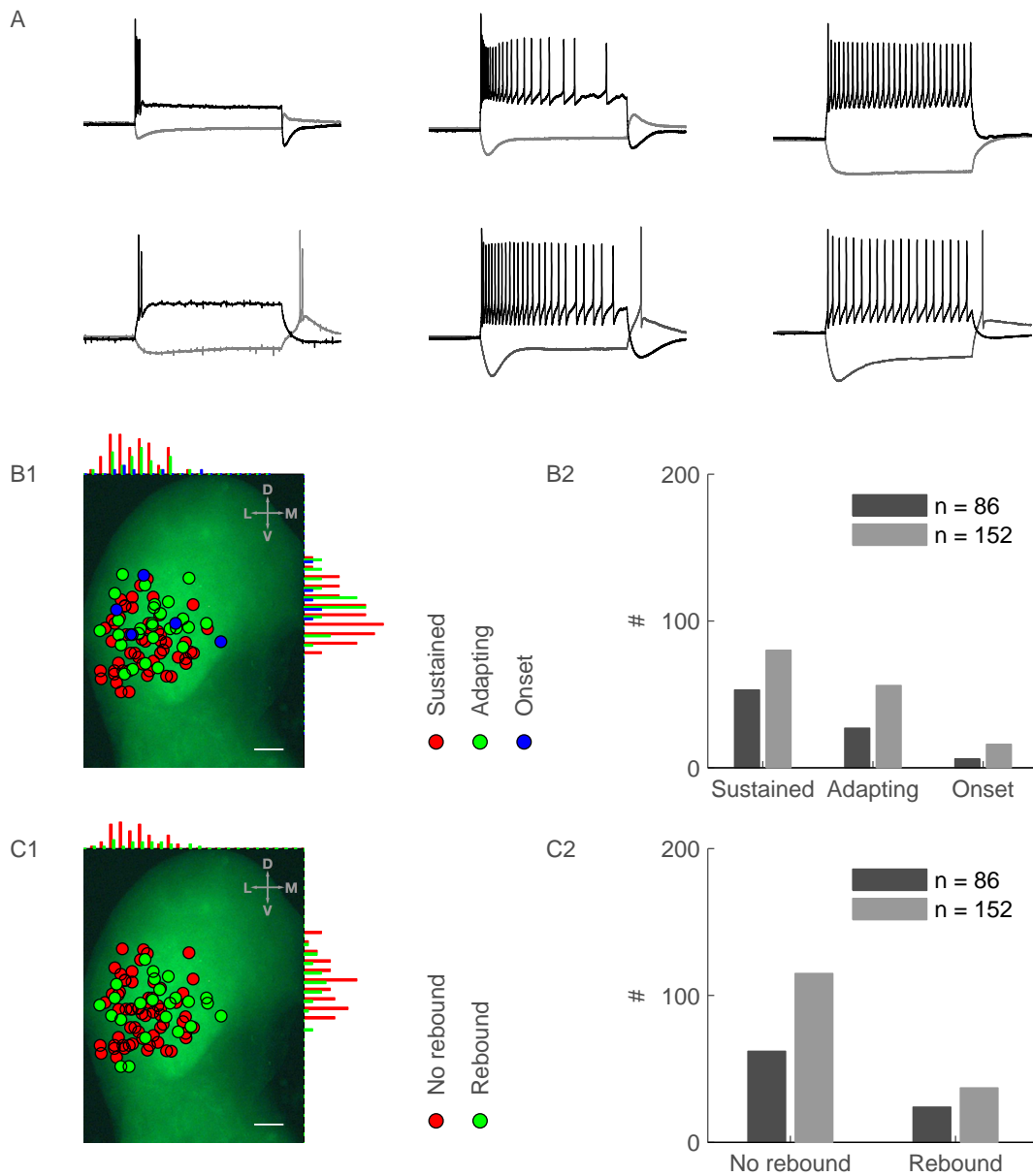


Figure 3.1: Neuronal firing patterns and their spatial distribution. . . (continued on the next page)

Figure 3.1: (continued from the previous page)... **A)** Example of the three major kinds of firing patterns in response to current injections, i.e. onset-bursting (left panel), adapting (middle panel) and sustained (right panel), with rebound spike (upper row) and without rebound spike (lower row). The gray line in each example shows the responses to -125 pA hyperpolarizing current injection, and the black line shows the responses to different depolarizing current injections. **B)** Spatial distribution of cells with onset-bursting (blue circle, ●), adapting (green circle, ●) and sustained (red circle, ●) firing patterns on an IC slice outlining the ROI ($n=86$) (B1), as well as histograms showing the number of cells exhibiting the three major types of firing patterns (B2). The black bars represent the total amount of samples ($n=152$); the gray bars represent all cells with position determined ($n=86$) that were used in (B1). **C)** Spatial distribution of cells with (red circle, ●) and without (green circle, ●) rebound responses (C1) on an IC slice outlining the ROI ($n=86$), as well as histograms showing numbers of neurons with or without rebound responses (C2). Black and gray bar as in (B). D=dorsal, V=ventral, L=lateral, M=medial. Scale bar is $300\ \mu\text{m}$.

ROI: onset-bursting (Fig. 3.1 A, left panel), adapting (Fig. 3.1 A, middle panel) and sustained (Fig. 3.1 A, right panel).

Sustained cells are supposed to encode information about sound duration and intensity (Wu, 2005), whereas onset-bursting cells are especially well suited for coincidence detection of incoming auditory stimuli (Wagner, 1994).

Although almost all studies with the exception of Sivaramakrishnan and Oliver (2001) have shown that the sustained pattern is the most common type (e.g. Reetz and Ehret, 1999; Bal et al., 2002), the fraction of adapting and onset cells is quite different among the different studies (e.g. Reetz and Ehret, 1999; Bal et al., 2002; Li et al., 1998; Bal et al., 2002; Koch and Grothe, 2003; Sivaramakrishnan and Oliver, 2001) *in vitro*. Our results in Fig. 3.1 B2 show that in the main data set ($n=152$), the sustained cells are prevalent ($n=80$), followed by the adapting cells ($n=56$) and the onset-bursting cells at last ($n=16$). Our data contained two cells with a buildup-pause pattern (Xie et al., 2008), which were classified as sustained neurons according to Peruzzi et al. (2000). Three cells in our data that were classified as adapting cells additionally had a slightly gradually decreasing spike amplitude during the current injection,

which have been described as the transient pattern in Sivaramakrishnan and Oliver (2001), but in our case were not as obvious as has been stated there.

The general distribution of the three firing patterns in the main data set was also confirmed in our subsample (n=86, sustained: 53, adapting: 27, onset-bursting : 6). Since for this subsample the location of the cells was available (see 3.1.1), these cells could also be used to analyze the spatial distribution of the three main firing types and to visualize this spatial distribution by plotting color coded cell locations on a standardized IC slice (Fig. 3.1 B1). The onset-bursting cells were excluded from the spatial distribution analysis due to the small amount of samples (n=6). Our results showed that the locations of the adapting cells were more dorsal than the sustained cells (paired student t-test, $p=0.007$), but the locations of the two firing patterns showed no difference on the horizontal axis (paired student t-test, $p=0.297$). The principle component analysis on the whole data set did not show a better significance in analyzing the differences between the locations of the two firing patterns (1st component: paired student t-test, $p=0.006$, 2nd component: paired student t-test, $p=0.585$).

In order to distinguish the differences between subdivisions, cells were further divided into ICc and ICx cells. Cells of the three firing patterns in both the ICc and the ICx held the same distributions as the whole data set (sustained vs. adapting vs. onset, 30:18:2 in the ICc, 23:9:4 in the ICx). The results showed that in the ICc, the locations of adapting cells were also more dorsally than the sustained cells (paired student t-test, $p=0.021$), but no difference in the locations of the two cell types was found on the horizontal axis (paired student t-test, $p=0.641$). However, in the ICx, the locations of firing patterns were neither significantly different on the vertical axis (paired student t-test,

Table 3.1: Paired student t-test on the spatial distribution of the three firing patterns.

		IC (n=86)			ICc (n=50)			ICx (n=36)		
		sustained (n=53)	adapting (n=27)	onset (n=6)	sustained (n=30)	adapting (n=18)	onset (n=2)	sustained (n=23)	adapting (n=9)	onset (n=4)
horz.	mean [μm]	637.43	705.71	733.18	830.33	858.08	-	385.86	403.20	-
axis	SEM [μm]	38.39	54.12	164.21	37.54	46.93	-	22.74	43.15	-
vert.	mean [μm]	1780	1545	1535	1767	1593	-	1797	1591	-
axis	SEM [μm]	40.70	52.96	105.47	46.55	52.80	-	72.62	124.53	-
paired	horz. axis	-	0.297	-	-	0.641	-	-	0.70	/
t-test	vert. axis	-	0.007	-	-	0.021	-	-	0.15	/
sustained	1 st comp	-	0.006	-	-	0.02	-	-	0.73	/
vs.	2 nd comp	-	0.585	-	-	0.74	-	-	0.68	-

1st comp. & 2nd comp.: first and second components of the principal component analysis. Only p-values of the paired student t-tests are shown in the table. $P < 0.05$ represents a significant difference between the tested pairs. The distances were measured to the lateral and dorsal boundary of the standardized IC slice.

$p=0.15$) nor on the horizontal axis (paired student t-test, $p=0.70$). The results were confirmed by a principle component analysis on both subdivisions separately, in that there were significant differences between the locations of the two firing patterns in the ICc (1st component: paired student t-test, $p=0.002$, 2nd component: paired student t-test, $p=0.74$). However, in the ICx, the locations of the two firing patterns had no significant differences (1st component: paired student t-test, $p=0.070$, 2nd component: paired student t-test, $p=0.67$).

Generally, our study showed that most cells in the ROI had the sustained pattern, followed by cells having adapting patterns and the onset-bursting patterns. Cells of different firing patterns were not homogeneously distributed within the ROI. As the spatial distribution of firing pattern types is potentially different in the ICc rostro-caudally (Reetz and Ehret, 1999, Figure 2), experiments measuring at different depths from the caudal end could easily lead to a difference in the distributions, which could explain, why our results

are different from that of a previous study (Yassin et al., 2015, unpublished). Moreover, it is a potential explanation of why other experiments have also resulted in distributions of the three main firing patterns with respect to their amount that are different from each other (Li et al., 1998; Bal et al., 2002; Koch and Grothe, 2003; Sivaramakrishnan and Oliver, 2001; Xie et al., 2008).

Rebound Spike

According to Sivaramakrishnan and Oliver (2001), the rebound depolarization of a cell is defined as a broad depolarization after the anode-break spike in reaction to membrane hyperpolarization (Wu, 2005). Rebound depolarizations in the IC are assumed to be created by the activation of hyperpolarization-activated current I_h (Koch and Grothe, 2003) and may permit precise temporal coding of complex sounds (Kuwada and Batra, 1999; Wu, 2005).

Whereas all comparable studies have observed rebound in sustained patterns (Fig. 3.1 A, middle panel, bottom) and adapting patterns (Fig. 3.1 A, right panel, bottom), some studies have not observed rebound depolarizations in onset-bursting patterns (Bal et al., 2002; Sivaramakrishnan and Oliver, 2001), while others have (Koch and Grothe, 2003). In our results we could find onset-bursting patterns with rebound as well (see example in Fig. 3.1 A, left panel bottom). This is most probably not a contradiction in the results among the different studies, but can be rather explained with the rare occurrence of rebound depolarizations in the onset-bursting pattern in the first place (in our case only 3/152).

The histogram in Figure 3.1 C2 further shows that cells without rebound depolarizations (n=115) are prevalent compared to cells with rebound (n=37), and the subsample confirms this proportion by trend (n=86, no rebound spike:

50, with rebound spike: 36). The subsample cells were also used to analyze the spatial distribution of the two rebound types (Fig. 3.1 C1).

Table 3.2: Paired student t-test on the spatial distribution of cells with and without rebound spike.

		IC (n=86)		ICc (n=50)		ICx (n=36)	
		rebound (n=36)	no rebound (n=50)	rebound (n=16)	no rebound (n=34)	rebound (n=8)	no rebound (n=28)
horz.	mean [μm]	675.06	629.91	947.54	812.36	732.31	666.53
axis	SEM [μm]	69.83	32.47	62.33	32.01	53.47	52.69
vert.	mean [μm]	1540	1720	1629	1735	1543	1623
axis	SEM [μm]	81.71	39.45	50.35	45.93	89.86	24.08
paired	horz. axis	-	0.06	-	0.037	-	0.52
t-test	vert.-axis	-	0.48	-	0.17	-	0.50
rebound	1 st comp.	-	0.48	-	0.04	-	0.72
vs.	2 nd comp.	-	0.06	-	0.14	-	0.74

1st comp. & 2nd comp.: first and second components of the principal component analysis. Only p-values of the paired student t-tests are shown in the table. $P < 0.05$ represents a significant difference between the tested pairs. The distances were measured to the lateral and dorsal boundary of the standardized IC slice.

Statistically, our results showed that the locations of cells with and without rebound spikes were not significantly different on the vertical axis (paired student t-test, $p=0.48$). However, cells with rebound spike were located more medially than cells without rebound spike by trend (paired student t-test, $p=0.06$). The principle component analysis applied on the whole data set did not show better significance in analyzing the differences between the locations of the two firing patterns (1st component: paired student t-test, $p=0.06$, 2nd component: paired student t-test, $p=0.48$).

In order to distinguish the differences between subdivisions, cells were fur-

ther divided into ICc and ICx cells. Cells with and without rebound spike held the same distributions as the whole data set (rebound spike vs. without rebound spike, 16:34 in the ICc, 8:28 in the ICx). The results showed that in the ICc, the locations of cells with rebound spike were also more medially than the cells without rebound spike (paired student t-test, $p=0.04$), but no significant difference of the locations of the two cell types was found on the vertical axis (paired student t-test, $p=0.17$). In contrast to the ICx, the locations of cells with and without rebound spike showed no difference both on the vertical axis (paired student t-test, $p=0.50$) and on the horizontal axis (paired student t-test, $p=0.52$). The principle component analysis on both subdivisions separately did not show a better significance in analyzing the differences between the locations of the cells with and without rebound spike in the ICc (1st component: paired student t-test, $p=0.04$, 2nd component: paired student t-test, $p=0.14$) and in the ICx (1st component: paired student t-test, $p=0.72$, 2nd component: paired student t-test, $p=0.74$). The results indicated that the cells with and without rebounds were distributed differently only in the ICc but not in the ICx.

Intrinsic Membrane Parameters

Among the intrinsic membrane parameters, the input resistance of the IC cells is the most well studied property (Li et al., 1998; Peruzzi et al., 2000; Bal et al., 2002; Sivaramakrishnan and Oliver, 2001; Koch and Grothe, 2003; Basta and Vater, 2003; Ahuja and Wu, 2007), followed by the membrane time constant (Reetz and Ehret, 1999; Koch and Grothe, 2003; Basta and Vater, 2003; Ahuja and Wu, 2007). However, the other intrinsic membrane parameters, i.e. the membrane capacitance (Yassin et al., 2015), the membrane time constant

(Basta and Vater, 2003) and the AP current threshold (Basta and Vater, 2003) have been rarely reported, as most studies have measured AP voltage threshold, same as the regional dependency of the intrinsic membrane parameters in general (Li et al., 1998; Yassin et al., 2015).

Table 3.3: Membrane properties of IC neurons from the ROI

	n=152					n=86					correlation ^a X		correlation ^a Y	
	mean	SEM	min	max	90%	mean	SEM	min	max	90%	r	p	r	p
C_m [pF]	101.8	4.9	15	379	190	118	6.99	15	379	153.5	-0.224	0.035	-0.30	0.004
R_m [M Ω]	308.7	16.65	54.8	1224	1065	283.9	16.68	61	821	1065	/	/	/	/
G_m [nS]	4.97	0.28	0.88	18.24	9.39	4.9	0.33	1.22	16.29	9.39	/	/	/	/
τ [ms]	27.9	1.47	1.7	157	52.2	29.2	1.72	3	82	49.7	-0.289	0.006	/	/
I_{thr} [pA]	380.01	18.22	62.5	1470	596	330.42	17.57	65	980	505	/	/	/	/

^a according to Pearson's. Experiments were in vitro and at room temperature.

In our work, we therefore determined all fundamental intrinsic membrane parameters and additionally analyzed their correlations with spatial position (Fig. 3.2, Table 3.3). In order to visualize these spatial correlation values, the results are again mapped onto standard slices (that are aligned with our ROI) as shown in Fig. 3.2 D. This mapping illustrates that a significant correlation of a cell parameter to the cell position on the horizontal axis could indicate sub-divisional differences of the cell parameter between ICc and ICx, and a significant correlation of a cell parameter to the cell position on the vertical axis could hint at ventral–dorsal regional differences in this parameter. In our case we observed negative significant correlations of cell membrane capacitance (C_m , Fig. 3.2 D1) to both their locations on the horizontal axis (Pearson's $r=-0.224$, $p=0.035$) and on the vertical axis (Pearson's $r=-0.30$, $p=0.004$), which indicated that cells with larger membrane capacitance, i.e. the apparent cell surface (Rall, 1969), were probably located more ventro-laterally in the ICx

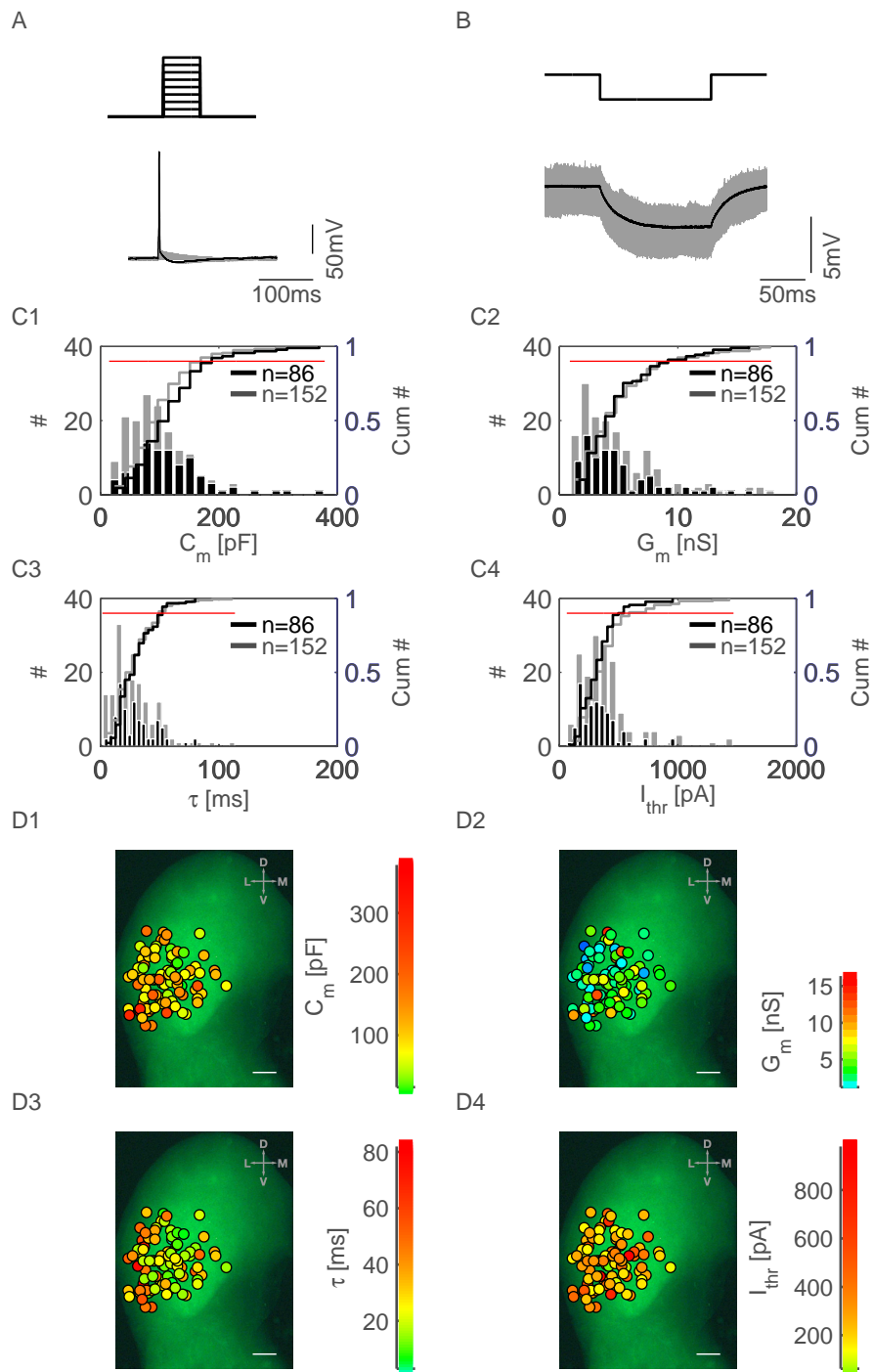


Figure 3.2: Intrinsic membrane properties and their spatial distribution. ... (continued on the next page)

Figure 3.2: (continued from the previous page)... **A)** Example traces of voltage responses (lower panel) to short depolarization steps (upper panel, 25 pA/step) under (gray lines) and above (black lines) the current threshold of the AP. **B)** Example traces (lower panel) of membrane voltage responses (grey lines) to hyperpolarizing current injection (7 pA, upper panel) and the average trace (black line). **C)** Histograms and cumulative histograms from the whole data set (grey, n=152) and the data subsample (black, n=86) show the cell membrane capacitance (C1), the membrane conductance (C2), membrane time constant (C3) and the AP current threshold (C4). Red lines show 90% of the cumulative histogram. **D)** Spatial distributions of neurons on an IC slice outlining the ROI (n=86). Color codes represent the values of the membrane capacitance (D1), the membrane conductance (D2), the membrane time constant (D3) and the current threshold of the AP (D4). D=dorsal, V=ventral, L=lateral, M=medial. Scale bar is 300 μ m.

than dorso-medially in the ICc. However, a comparison with a previous study (Yassin et al., 2015) with respect to membrane capacitance is difficult, since they have measured capacitance only in the ICc. Thus, we separated cells further into ICc and ICx. The separation of cells confirmed the assumption that the membrane capacitance of ICx cells (n=36, 143.52 ± 12.30 pF) were remarkable larger than that of the ICc (n=50, 99.90 ± 7.19 pF, paired student t-test, p=0.002).

Another observation was that our results showed the same (Sivaramakrishnan and Oliver, 2001) or higher input resistance (Li et al., 1998; Peruzzi et al., 2000; Bal et al., 2002; Koch and Grothe, 2003; Ahuja and Wu, 2007) compared to previous studies. An explanation is that, in general, the input resistance is higher at room temperature, which was used for our experiments, and lower at biological temperatures (Griffin and Boulant, 1995). The input resistance of cells, together with its reciprocal value, i.e. the membrane conductance, both had no significant correlation with the cell location on the horizontal and vertical axis (see Table 3.3).

The membrane time constant of cells (τ , Figure 3.2 D3) had a negative significant correlation to the cell location on the horizontal axis (Pearson's $r=-0.14$,

$p=0.006$) but not on the vertical axis (see Table 3.3). This suggests that cells in the ICc (dorsal-medially in the ROI) probably govern rapid equalization of membrane potential to react faster to changes of inputs (Rall, 1969) than cells in the ICx (ventro-laterally in the ROI), which has been also shown in a previous study (Li et al., 1998). The firing ability of cells, i.e. the current threshold of the AP (I_{thr} , Figure 3.2 D4), and the remaining electrical cell parameters, i.e. the membrane conductance (G_m , Figure 3.2 D2) or the input resistance of cells, showed no spatial correlations (see Table 3.3), which means that the values of the parameters are homogeneously distributed in the ROI without regional differences. The regional homogeneity of the input resistance and the membrane conductance has been also reported in Li et al. (1998).

Generally, our study of the electrophysiological parameters of the cells indicated that the membrane capacitance was spatially heterogeneous, whereas the input resistance, the membrane conductance and the membrane time constant were spatially homogeneous. The comparison of our main data set with the subsample showed that the latter one had a slightly higher mean value for cell capacitance, which was a cell parameter with spatial correlation, but not for the membrane time constant and other cell parameters that have no spatial correlations. This could mean that the subsample (which was acquired from the presynaptic input experiment) contains a higher percentage of cells from the ICx, which are located in the ventral-lateral parts of the ROI, and contains a larger amount of medium and large size cells (Rockel and Jones, 1973a; Mylius et al., 2014), which was confirmed by the separation of data into ICc and ICx.

3.1.2 Morphology

In a next step, we were interested in the morphological properties of the cells, i.e., the dendritic field area, length and width, soma length and width, as well as the numbers of main dendrites, in order to find out, whether the intrinsic innervations and electrophysiological properties are correlated to the morphology of the cell. For this purpose, the morphological parameters were measured on confocally reconstructed images of fluorescence dye filled cells (n=53) in ImageJ (see methods 2.5). The dendritic field area was defined according to Wallace et al. (2012) as the area of the polygon connecting the distal ends of the visible dendrites (Fig. 3.3 A, left). The two main axes of an ovoid shape enveloping the polygon were defined as the length and width of the dendritic field (Fig. 3.3 A, middle). Analogously, the two main axes of the soma ellipse were defined as the length and width of the soma (Fig. 3.3 A, middle). The number of main dendrites was counted manually (Fig. 3.3 A, right).

Our results (see Table 3.4) were consistent with previous studies with regard to the range of the dendritic field and the soma size in cats (Rockel and Jones, 1973b,c; Oliver, 1984; Oliver et al., 1991; Malmierca et al., 2005), which have been suggested slightly larger in human (Geniec and Morest, 1971) but smaller in rats and mice (Zook and Casseday, 1985; Meininger et al., 1986). However, according to these studies, cells can be clustered into different groups according to the cell morphology, whereas our data in the Mongolian gerbil was rather continuous in all measured parameters, i.e. the dendritic field area (Fig. 3.3 B1), the length and width of the dendritic field (Fig. 3.3 B2), the length and width of soma (Fig. 3.3 B3), as well as the dendritic field and soma

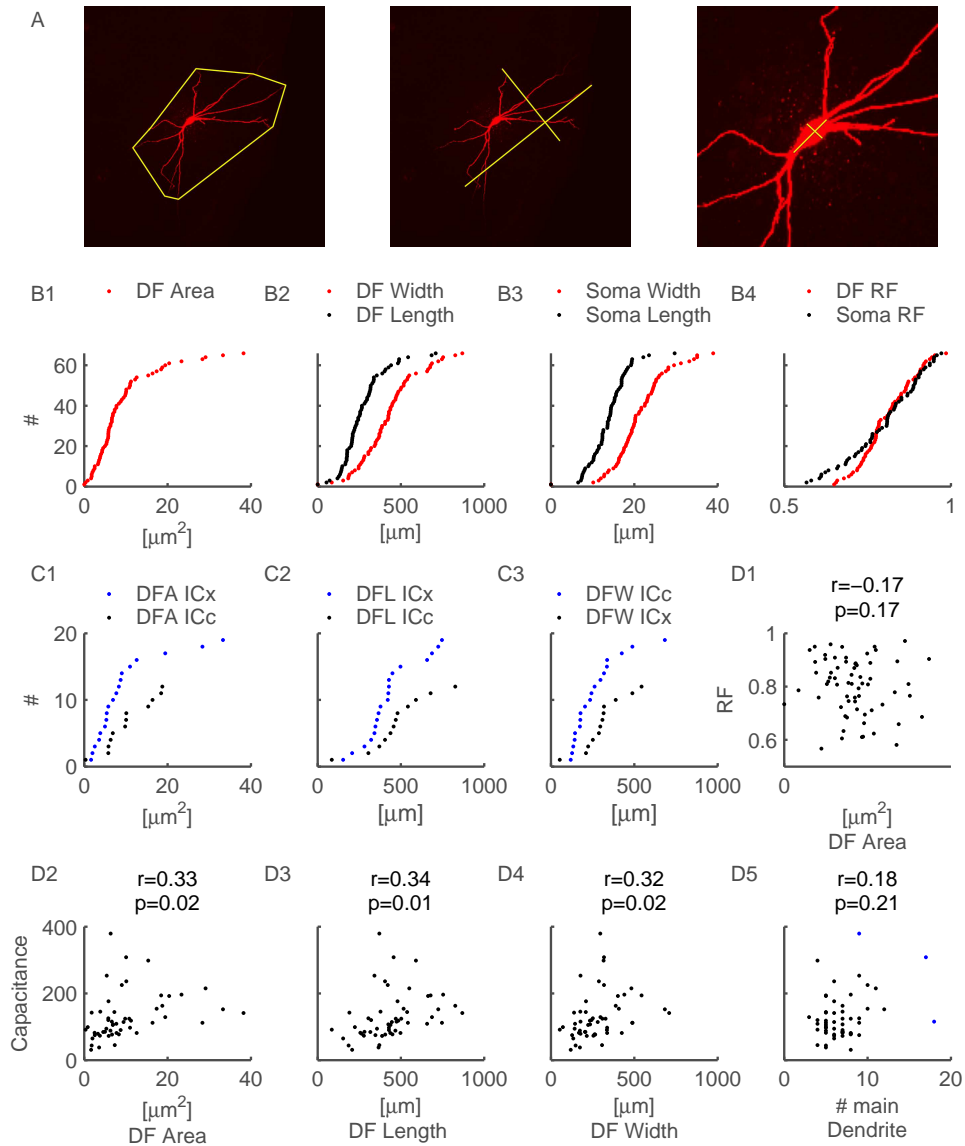


Figure 3.3: Morphological properties and their correlations to electrophysiology. **A)** Illustrations showing the landmarks (yellow lines) of measurements of the neuronal dendritic field (left), length and width of the dendritic field (middle) and soma length and width (right) on the maximum-intensity projection of the confocal image of an example neuron from the ROI. **B)** Cumulative histograms ($n=53$) of dendritic field area (B1), length and width (B2), soma length, width (B3) and roundness (B4). **C)** Cumulative histograms ($n=31$) of dendritic field area (C1), length (C2) and width (C3) in the ICc ($n=19$) and ICx ($n=12$) separately. **D)** Correlations of dendritic field area vs. roundness factor (D1), and capacitance vs. dendritic field area (D2), dendritic field length (D3), dendritic field width (D4) and number of main dendrites (D5) ($n=53$). R-values and p-values from the Pearson's correlation. Blue points: outliers. DF: dendritic field, DFA: dendritic field area, DFL, dendritic field length, DFW, dendritic field.

Table 3.4: Morphological properties and the correlations to electrophysiology

	n=53				Correlation ^a C_m	
	mean	sem	min	max	r	p
Soma Width [μm]	13.9	0.62	6.57	29.7	0.31	0.02
Soma Length [μm]	21.6	0.87	10.2	39	0.25	0.06
DF Width [μm]	280	19.1	52.9	708	0.29	0.03
DF Length [μm]	442	23.7	85.7	869	0.30	0.03
DF Area [μm^2]	$1.00 \cdot 10^5$	$0.12 \cdot 10^5$	$3.48 \cdot 10^3$	$3.83 \cdot 10^5$	0.32	0.02
Soma RF	0.65	0.02	0.42	0.97	/	/
DF RF	0.64	0.02	0.64	0.94	/	/
# Main Dent.	6.98	0.39	3	18	/	/

^a Threshold of p-value in paired student t-test: $p=0.05$. All p-values smaller than 0.90 or larger than 0.30 are shown as "-" in the table.

roundness factor (Fig. 3.3 B4).

In contrast to our results, previous studies have reported that the neurons can be clustered according to their dendrite field or soma size (Geniec and Morest, 1971; Rockel and Jones, 1973b,c; Oliver, 1984; Faye-Lund, 1985; Meininger et al., 1986; Oliver et al., 1991; Malmierca et al., 2005). In our results, however, all parameters were only discrete towards the maximum and minimum values, which was most likely due to the small amount of samples at the extreme ends of the distribution. An assumption is that the continuity in our data could be explained by the pooling of all cell types, including the suggested disc-shape and stellate neurons from the ICc (e.g. Rockel and Jones, 1973b) and including the suggested large, medium and small cells from the ICx (e.g. Rockel and Jones, 1973a). While it might be possible to cluster cells of the individual cell types into groups according to their morphologi-

cal parameters, the non continuous intervals between these groups might be compensated for by the measurements of another group of cell types, so that finally no gaps can be found in the pooled data. Of course, the continuity in the parameters could also be an indication that there is probably no distinct grouping in cell size once a sufficiently large amount of cells is sampled.

In order to test this assumption, cells that had been confocally reconstructed and where positions in the ROI were available (n=31), were further sorted into ICc (n=19) and ICx (n=12) cells. By this way, only the histograms of two parameters had discontinuities: firstly, the length of the dendritic fields of ICc cells (Fig. 3.3 C2) jumped from 500 to 700 μm , but not the width (Fig. 3.3 C3) or area of the dendritic fields (Fig. 3.3 C1). Nevertheless, the discontinuities shown might be related to the small sample size of cells with dendritic fields longer than 500 μm . Further, the dendritic field area of ICx cells (Fig. 3.3 C1) jumped between 1×10^5 and 1.5×10^5 μm^2 , whereas the other parameters were distributed continuously. Thus, the data most probably suggests that both cells in the ICc and in the ICx can not be classified by their size or shapes. However, to conclude, whether these results argue against the disc-shaped and stellate cells classifications in gerbils would need more data in the ICc and studies that would also consider the orientation of the cells.

While we tried to patch different sized cells during our experiment, we found only two cells that had a dendritic field width of less than 72 μm , which was close to the width reported as typical for disc-shaped neurons (50–70 μm) in some earlier studies using the Golgi staining method (FitzPatrick, 1975; Malmierca et al., 1993; Meininger et al., 1986). A possible reason for this discrepancy to our results is that the Golgi-method is known for problems

with incomplete impregnation in individual processes (Malmierca et al., 1993). Comparably, a more recent study (Wallace et al., 2012) measuring the morphology of laminar cells in the ICc also has reported a rather low proportion (6/38) of cells with a dendritic field width below 75 μm . These results are closer to our results, since our data was acquired from both the ICc and the ICx, which effectively doubles the investigated area while disc-shaped neurons could only be found in the ICc. Additionally, in contrast to all other studies, we used a confocal microscope. The higher optical resolution and contrast of a confocal microscope might have helped to identify the very thin dendrites at the distal ends of dendritic field, which could potentially have led to a larger (and more accurate) measurement of the dendritic field. Therefore, it indicated that the differences were not a sampling bias in our experiments.

Comparing the morphology and electrophysiology of the cells, our results showed obvious significant correlations of cell capacitance to the dendritic field area (Pearson's correlation, $r=0.33$ $p=0.03$, Fig. 3.3 D2), and the dendritic field length (Pearson's correlation, $r=-0.34$ $p=0.01$, Fig. 3.3 D3) and width (Pearson's correlation, $r=-0.32$ $p=0.02$, Fig. 3.3 D4), but not to the number of main dendrites (Pearson's correlation, $r=-0.18$ $p=0.21$, Fig. 3.3 D5). Additionally, we showed that the roundness of the cell had no significant correlation with the dendritic field area (Pearson's correlation, $r=-0.17$ $p=0.17$), which means the round cells are not necessarily having larger dendritic fields (Fig. 3.3 D1).

Because the membrane capacitance has a linear relationship with the cell surface area, capacitance has been often measured experimentally as a way of determining the cell surface area (Hille, 2001). The actual surface area of neurons is almost always distributed over surfaces that are intricate and com-

plex (Hille, 2001), including the cell soma surface, the dendrites surfaces, etc. With respect to the other electrophysiology parameters: the input resistance, the membrane conductance and the membrane time constant, no significant correlations with morphological parameters were found.

3.1.3 Miniature Postsynaptic Currents Study

In addition to the morphological and electrophysiological studies, we also characterized the amplitudes and time constants of miniature postsynaptic currents (mPSCs). The mPSCs arise from random releases of presynaptic vesicles (Berretta and Jones, 1996; Zhang et al., 2005) and are not induced by photoactivation. Therefore, the mPSCs are one source of noise existing in intrinsic PSC input recordings that needs to be excluded. Besides that, mPSCs are also the quantal events underlying PSCs (Uteshev and Pennefather, 1996). The variation in the amplitude of mPSCs is a major contributor to the variance of evoked synaptic responses (Uteshev and Pennefather, 1996). Thus, determining the frequency, amplitudes and decays of mPSCs can lead to a prediction of the features of PSCs signals and their accompanying noise.

For recording mEPSCs and mIPSCs, sodium and potassium channels were blocked using tetrodotoxin (TTX). TEA and 4AP were added in the extracellular solution in order to avoid AP induced spontaneous releases from the recorded neuron. For recording mEPSCs, STRY and SR 95531 were added in the intracellular solution in order to block the glycine receptors and the GABA receptors. For recording miniature inhibitory postsynaptic currents (mIPSCs), DNQX and AP5 were added in the intracellular solution in order to block the AMPA channel and the NMDA channel, respectively (Porres, 2012).

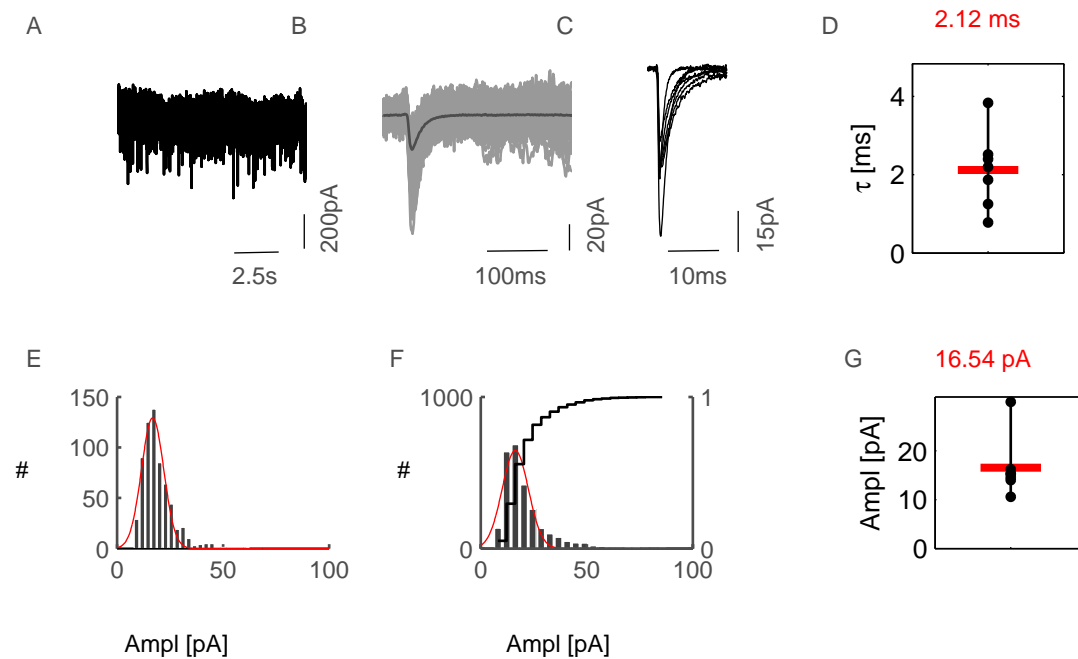


Figure 3.4: Miniature EPSC analysis in IC neurons from the ROI. **A)** Example of a raw data trace with recorded mEPSCs. **B)** For each recorded cell (n=7), mEPSCs were extracted off-line and aligned using a threshold template matching routine. An average (black line) was generated to determine the amplitude and the decay time constant of mEPSCs. **C)** Averaged mEPSCs for all recorded cells. **D)** Mean (red bar) of decay time constant of all averaged mEPSCs (dots) shown in C. **E)** Frequency histogram of the mEPSC amplitudes from the example recording, and a Gaussian fit (red line) was used to determine the median value of the mEPSC amplitude. **F)** Frequency histogram (left axis) and cumulative frequency histogram (right axis) of all pooled mEPSC amplitudes for each cell (n=7). **G)** Mean (red bar) of the medians (dots) of mEPSC amplitudes (n=7).

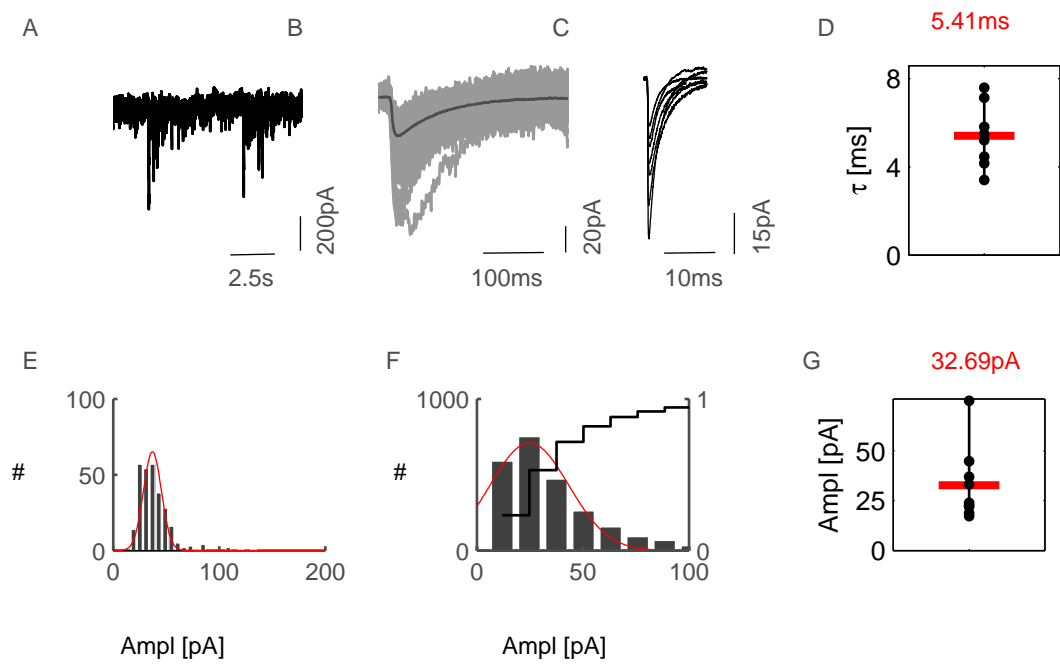


Figure 3.5: Miniature IPSC analysis in IC neurons from the ROI. analog to Figure 3.4 for IPSC (n=7).

Figure 3.4 D and Figure 3.5 D show mEPSCs and mIPSCs, respectively. On average, mEPSCs had a shorter time constant than mIPSCs (paired student t-test, $p=2 \times 10^{-4}$). The average time constant of mEPSCs of all cells ($n=7$) aligned was 2.12 ± 0.36 ms, and the average time constant of mIPSCs ($n=7$) was 5.41 ± 0.51 ms. In contrast, the average amplitudes of mEPSCs of all cells ($n=7$, 16.54 ± 7.40 pA) had no significant difference compared to the average amplitude of mIPSCs ($n=7$, 32.7 ± 18.3 pA, paired student t-test, $p=0.0545$). Moreover, the peaks of the amplitude histogram of the pooled mEPSCs were 16.80 ± 0.13 pA and that of mIPSCs were 24.80 ± 0.24 pA, which were in the same range of the average amplitude. Due to that the amplitudes depend on the holding potential and ion concentrations, therefore, the results were not directly relevant to the mapping experiments rather than the controls of the mEPSCs experiments.

Thus, we expected that in the PSC input mapping experiments, the decay of mIPSCs was in general slower than those of mEPSCs. We used these results in the PSCs detection algorithm for the PSCs inputs mapping experiments as references to exclude the spontaneous activities, based on the absolute peak amplitude of the PSC, the maximum absolute slope of the rising part of the PSC, the time-interval between the initiation of the PSC and its peak (Bendels et al., 2008).

3.2 Organization of Intrinsic Innervations

In order to study the intrinsic structure of the IC, the cells were recorded in voltage clamp, while a laser beam was used to stimulate the caged-glutamate incubated acute slices at the preset stimulation spots. Hence postsynaptic cur-

rents (PSCs) could be measured, if there were intrinsic connections between the laser beam affected area and the recorded neuron. The cells were clamped at a membrane potential in between the reversal potential for chloride (Sturm et al., 2014) and the reversal potential of glutamatergic responses (Sturm et al., 2014) in order to acquire both the EPSCs and IPSCs within one pass. By this means, the EPSC inputs could be measured as inward currents, and the IPSC inputs could be measured as outward currents (Fig. 3.6 B).

The arriving time of the PSCs contained the temporal characteristics of the intrinsic innervations (see 3.2.1), whereas the locations of the stimulation sites, for which PSCs were detected, suggested the spatial arrangements of the intrinsic innervations (see 3.2.2). However, PSCs detected in this way might contain not only the signals induced by the stimulation of a presynaptic partner of the recorded cell, but also three kinds of noise that needed to be excluded to determine a more precise amount of innervation: firstly, the current responses to direct glutamate stimulation of the recorded cell itself (direct response); secondly, the spontaneous release of mPSCs on the synapses; thirdly, the spontaneous firing of a presynaptic partner of the recorded cell.

After a successful noise removal, the unbiased intrinsic innervations could be determined. This allowed us to analyze the correlations of intrinsic innervations to the electrophysiological and morphological parameters (Section 3.2.3), which further enabled us to show regional differences in the structure of the intrinsic innervations (Section 3.2.4).

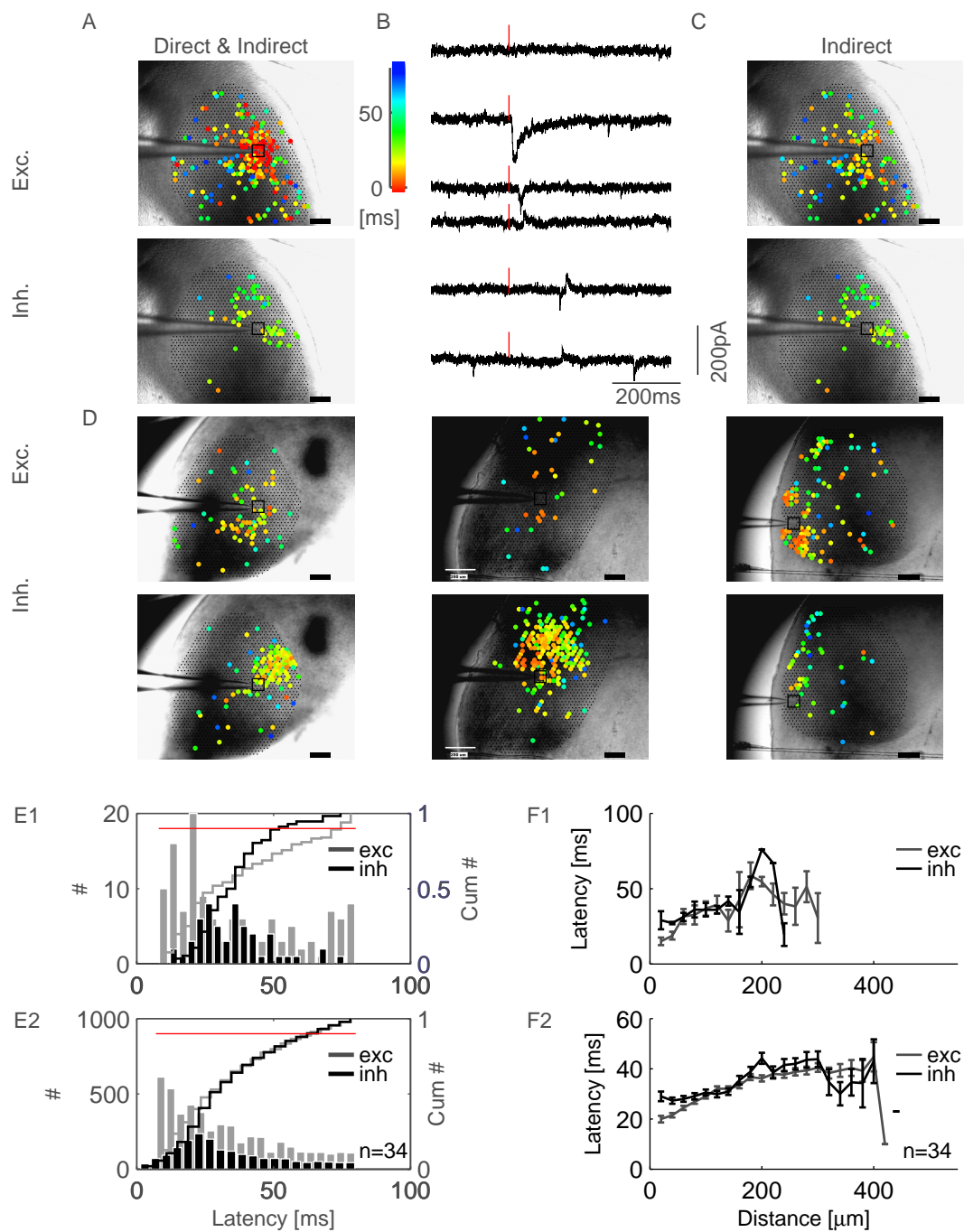


Figure 3.6: Latency map of direct and indirect PSCs. ... (continued on the next page)

Figure 3.6: (continued from the previous page) ...Color-coded latency map showing the temporal distribution and the location of direct and indirect PSCs **A)** Example of a latency map with color-coded direct (<7 ms latency), indirect (between 7 and 81 ms) EPSCs (upper) and IPSCs (lower) superimposed onto the stimulation sites (black dots) on a bright field image. Colors indicate latency values of 0–81 ms (red to green). Scale bar=200 μm . **B)** Example of raw data traces showing traces without PSCs (top), with direct PSC (2nd), indirect EPSCs (3rd), indirect IPSCs (4th), indirect EPSCs prior to IPSCs (5th) and indirect EPSCs prior to IPSCs (6th). **C)** Latency maps of only indirect EPSCs (top) and indirect IPSCs (bottom) (i.e. on-points). **D)** Further examples of indirect EPSC (upper row) and IPSC (lower row) latency maps. **E)** Histogram showing the distribution of latency of the first EPSC (black bar) and the first IPSC (grey bar) after stimulation for the example cell (E1) and for all cells (E2) **F)** The mean EPSC (grey line) and IPSC (black line) latencies vs. distance for the example cell (F1) and for all cells (F2).

3.2.1 Temporal Organization

The temporal characteristics of the intrinsic inputs were contained in the latencies of the PSCs. In this work, the PSC latency was defined as the occurrence of the first EPSC/IPSC after the start of the laser stimulation at each site (Bendels et al., 2010). The amount of latency of a PSC could be used to distinguish between current responses to direct glutamate stimulation of the recorded cell itself (direct response) and the PSCs elicited by the presynaptic input neurons (indirect response).

PSCs were defined as indirect, if they occurred in the time interval that started right after the time window (7 ms) of direct activation and ended when the EPSC rate dropped below three standard deviations above the average spontaneous EPSC rate. In our recordings, the time interval in which EPSCs were classified as indirect had a duration of 81 ms (see methods 2.5).

We constrained our observation to latencies within a time window, for that the EPSC rates were higher than three standard deviations above the average spontaneous EPSC rate (81 ms), which was considered as the effective time of the laser stimulation for our type of setup (Bendels et al., 2008). Within

this time window, the indirect responses could be distinguished from direct responses by using a threshold (onset latency), which was determined in the calibration experiment of the scanning resolution (3 ms, see methods 2.3). To be certain, we used a rather conservative onset latency of 7 ms. This had the disadvantage that a few indirect responses might get lost. However, the advantage was that we could be sure that all direct responses were definitely excluded in order to get a more precise amount of intrinsic inputs (Section 3.7).

As a result we detected raw PSC traces of six different typical cases (see examples in Figure 3.6 B): 1. Traces with no intrinsic PSC inputs; 2. Traces with direct inputs that are caused by stimulating the recorded cells (direct response); 3. Traces with only excitatory PSC inputs; 4. Traces with only inhibitory synaptic inputs; 5. Traces with an excitatory PSC input prior to an inhibitory PSC input; 6. Traces with an inhibitory PSC input prior to an excitatory PSC input.

Figure 3.6 A is an example, where the latencies of the first EPSCs/IPSCs detected at a stimulation site are color-coded and superimposed on a map of the stimulation sites, which creates a latency map of EPSCs/IPSCs respectively (exc. Figure 3.6 A, upper row; inh. Figure 3.6 A, lower row). Direct inputs (<7 ms) are still shown in red spots that overlay the stimulation sites mostly around the recorded neurons.

Figure 3.6 C shows the latency map of the example cell after removal of direct PSCs, containing only the sites with indirect intrinsic PSC inputs. (Exc: Fig. 3.6 C1, Fig. 3.6 D, upper row, Fig. 3.6 C2, Fig. 3.6 D, lower row). Such stimulation sites for which an indirect PSC input was measured were termed *on-points* (Bendels et al., 2010).

Figure 3.6 E2 shows that the total amount of excitatory stimulation sites for all cells (n=34) exceeded that of inhibition (Fig. 3.6 F2), which suggests the dominance of EPSCs over IPSCs in sum. Further Fig. 3.6 F2 shows that both latencies of EPSCs and IPSCs increased over distance. Since we measured the monosynaptic events (Bendels et al., 2008), this increase in PSC latency represents the fact that the axonal conduction delays increased with distance, i.e. the longer the axonal distance is, the more time it takes for the currents to arrive at the recorded cell. Generally, the EPSCs (31.16 ± 0.29 ms) arrived prior to the IPSCs (33.00 ± 0.44 ms) (paired student t-test, $p=0.001$) up to a distance of approx. 300 μm from the distal end of the dendrites to the soma (see Fig. 3.6 F2).

Further, Fig. 3.6 F2 shows that the initial latency values (delay) of IPSCs in close proximity to the cell are higher than that for EPSCs, suggesting that in close distance to the cells, the intrinsic connections for the EPSCs are probably short and direct axonal connections to the dendrites of the recorded neuron, whereas the axonal conduction of the IPSCs go a more winding way. However, this can also be caused by multisynaptic excitation, or the excitability difference of excitatory and inhibitory neurons. In contrast, with increasing distance, both latencies of EPSCs and IPSCs increase and are getting closer to each other, which suggests that further distally from the cell, EPSCs and IPSCs seem to have a similar way of connecting to the recorded cells.

The standard error of the mean (SEM) of the latencies was also increasing with distance. It can further be seen in Figure 3.6 F2 that there is a sudden drop in the rate of EPSCs at a distance of 300 μm . The large SEM after that suggests that from this distance on, spontaneous activities are prevalent. Comparably,

IPSCs existed up to a distance of 400 μm , and with less spontaneous activities detected in general.

3.2.2 Spatial Organization

In the previous section, indirect PSCs have been distinguished from direct PSCs using their latencies to acquire the principal temporal organization and the *on-points*. However, the indirect PSCs detected in this way still could contain noise, i.e. the spontaneous presynaptic spikes (Dickson et al., 1997) and the spontaneous release of vesicles, i.e. mPSCs (Berretta and Jones, 1996; Zhang et al., 2005). Thus, these kinds of noise could result in a bias when determining the total amount of intrinsic inputs for a cell (Bendels et al., 2008).

In order to determine a more precise amount of intrinsic inputs and its spatial organization without this bias, we used an algorithm based on spatial correlations and statistical significance calculation (Bendels et al., 2008). Briefly, the algorithm starts by using the spatial distribution of *on-points*, i.e. using the stimulation sites displaying only the indirect PSCs (Fig. 3.7 A1). In each stimulation site, a p-value is then calculated based on the null hypothesis, that the detection of *on-points* measured within the area of scanning resolution (100 μm , see materials 2.3) is triggered exclusively by noise, i.e. the spontaneous presynaptic spikes or the mPSCs instead of the laser stimulation.

The significance is calculated by the algorithm based on the rate of spontaneous activities, which is measured at the beginning of each trace before the actual laser stimulation. If the p-value calculated for a stimulation site is low ($p < 0.05$), which means that the null hypothesis is declined, this effectively means that the detected *on-points* around the stimulation site are caused by ac-

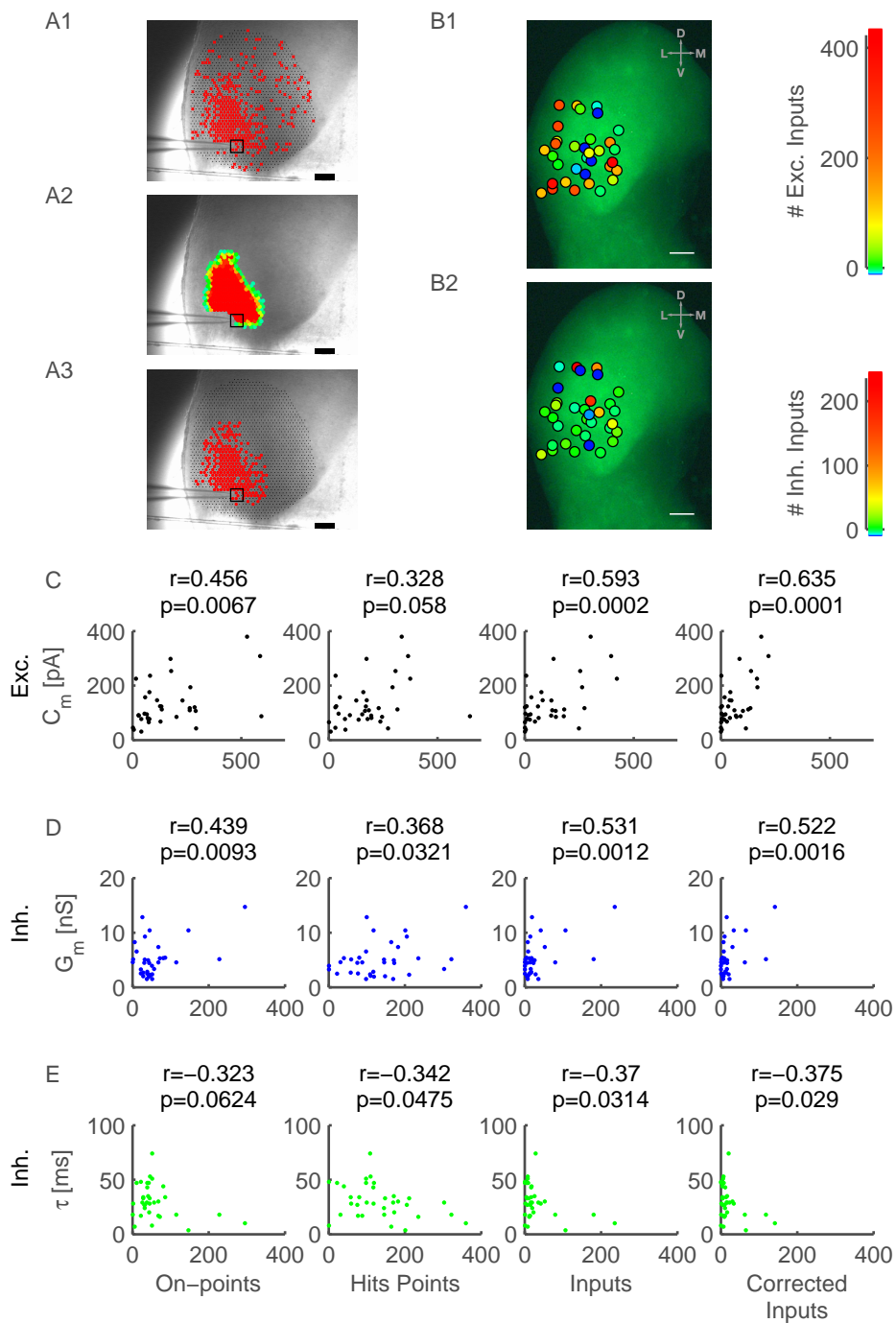


Figure 3.7: Spatial distribution of the amount of intrinsic inputs and their correlations to electrophysiological parameters. . . . (continued on the next page)

Figure 3.7: (continued from the previous page) ... textbfA) Example of *on-points* (A1, red cross), *hit-points* (A2, color-coded points, significance <0.05) and inputs (A3, red cross, significance <0.05) acquired. Colors of the *hit-points* indicate p values of 0.05 (green) or smaller (yellow to red). The area that the *hit-points* are located in, forms the significance field. Black points are the stimulation sites. The black square indicates the location of the recorded cell. Scale bar=200 μm . **B)** Amount of excitatory inputs (B1) and inhibitory inputs (B2) of all samples from the PSC input mapping experiment are color-coded, and spatially plotted on an IC slice outlining the ROI. Blue circle=no inputs, D=dorsal, V=ventral, L=lateral, M=medial, Scale bar=300 μm . **C)** Correlation of membrane capacitance of a cell to the number of *on-points*, *hit-points*, *intrinsic inputs* and *intrinsic input correction* in the case of excitation. R-values and p-values according to Pearson's correlation. **D & E)** Correlation of membrane conductance (D) and membrane time constant (E) of a cell to the number of *on-points*, *hit-points*, *intrinsic inputs* and *intrinsic input correction* in the case of inhibition. (r and p as in C; B-E, n=34).

tual stimulation instead of noise. Such a stimulation site is taken as a *hit point* (Fig. 3.7 A2) (Bendels et al., 2010). The spatial arrangement of all *hit points* further constitutes a field, which is called significance field or *input field* in this work. This field represents the area of stimulation sites that are significant ($p < 0.05$) (Fig. 3.7 A2). The *on-points* having a p-value of less than 0.05 (within the significance field) are termed *inputs*.

These intrinsic inputs represent the locations that the intrinsic innervations are coming from. However, since the intrinsic inputs are counted based on the number of stimulation sites as units, a value that is more meaningful for showing the number of innervation can be acquired mathematically by further subtracting the expected occurrence of the spontaneous events (significant *on-points*, i.e. intrinsic inputs minus the expected number of noises) for all sites. This value is termed *corrected inputs*.

In Figure 3.7 the spatial distribution of intrinsic innervations is visualized by the color-coded amount of inputs of cells mapped onto a standardized IC slice (Exc.: Fig. 3.7 B1, Inh.: Fig. 3.7 B2). Statistically, there were no significant correlations between the amount of excitatory intrinsic inputs and the cell

location on the horizontal or vertical axis. Considering these results mapped onto the standard slice again that was aligned with our ROI, a correlation to the horizontal axis would indicate sub-divisional differences between ICc and ICx, whereas a correlation to the vertical axis would indicate ventral–dorsal regional differences. On the contrary, no significant correlation to both axes, as in the case of excitatory intrinsic inputs, could indicate that there were either absolutely no correlations in the ROI, or that there were regional compensations. The number of inhibitory intrinsic inputs, however, was significantly correlated to the vertical axis (Pearson's $r=0.34$, $p<0.05$), which suggests that inhibitory intrinsic inputs probably exist more in the dorsal than the ventral part of the ROI. However, in our results, we could only show a larger variance of inhibitory inputs in the dorsal than in the ventral subregions of the ROI (for more details about regional differences see Section 3.2.4.2)

3.2.3 Correlation to Electrophysiology and Morphology

Photostimulation is a common technique in order to study neuronal circuits and the location of functional synaptic inputs. Many of such studies have classified the synaptic inputs according to morphological neuronal types (e.g. Sawatari and Callaway, 2000; Zarrinpar and Callaway, 2014) or to the electrophysiological firing patterns (Dantzker and Callaway, 2000). However, studies that correlate synaptic inputs to electrophysiological membrane properties or morphology are still absent in the IC. We studied the correlations between the amount of intrinsic inputs of cells, their electrophysiological and morphological parameters, with the intention that it might help to reveal the biophysical origin of the intrinsic inputs.

Correlation to Electrophysiological Properties

Figure 3.7 C shows that in case of excitation, all innervation parameters, i.e. the numbers of excitatory *on-points*, the *hit points*, the excitatory intrinsic inputs and the corrected intrinsic inputs have significant positive correlations with the membrane capacitance. As the cell membrane capacitance is proportional to the apparent cell surface (Hille, 2001), the positive correlation with excitation parameters suggests that the larger the surface of a cell is, the more excitatory intrinsic inputs it gets.

In the case of inhibition, however, the innervation parameters showed significant positive correlation with the membrane conductance (Figure 3.7 D). As the membrane conductance represents the permeability of the membrane that depends on a combination of ion channels and ion pumps (Hille, 2001), this means that a cell membrane with more dense ion channels, and thus more leaks, gets more inhibitory intrinsic inputs. The inhibitory innervation parameters were also significantly negatively correlated with the membrane time constant (Figure 3.7 E), which suggests that the more rapid the cells membrane needs to reach equilibrium (Hille, 2001), the more inhibition it gets.

Additionally, it was interesting to know whether there were dependencies between the intrinsic innervation and the cell type, since in the study of Callaway (2002) for the visual cortex, it has been indicated that the functional inputs have been different for cells with sustained and bursting firing patterns. However, the data of this thesis (n=33) showed no significant differences in the amount of inputs between sustained (n=21) and adapting cells (n=11) both in the case of excitation (paired student t-test, $p=0.81$) and in the case of inhibition (paired student t-test, $p=0.68$). Also no significant differences of inputs

were found between cells with and without rebound spikes in the case of excitation (paired student t-test, $p=0.26$) and in the case of inhibition (paired student t-test, $p=0.87$). Onset-bursting cells were excluded due to the small amount of samples ($n=1$).

Correlation of Intrinsic Innervation to Morphological Properties

To directly visualize the relation between cell morphology and intrinsic inputs, the confocal reconstructions of two example cells (Fig. 3.8 A and B) were brought to their original positions under the patch clamp, and superimposed with the excitatory (Fig. 3.8 A2 and B2) and inhibitory intrinsic input maps separately (Fig. 3.8 A3 and B3).

By using the Pearson's correlation, we showed that the amount of excitatory inputs had a significant positive correlation with almost all measured morphological parameters, i.e. the dendritic number, dendritic field length, dendritic field width, soma width and soma length (Fig. 3.8 D1, D3–D6). The excitatory inputs did not show significant correlation to the dendritic field area (Pearson's correlation, $r=0.31$, $p=0.12$); however, the excitatory inputs correction again did show a significant correlation to the dendritic field area (Pearson's correlation, $r=0.41$, $p=0.04$, Fig. 3.8 D2). These measured morphological parameters were all directly correlated to the actual cell surface, suggesting that the larger the cell surfaces are, the more excitatory inputs they get. These results also validated the previous indirect conclusion that the excitatory inputs were correlated with the membrane capacitance and, consequently, the cell surface (see Section 3.2.3).

All together, the significant correlation of the intrinsic inputs with the electrophysiological and morphological parameters suggests that the excitatory

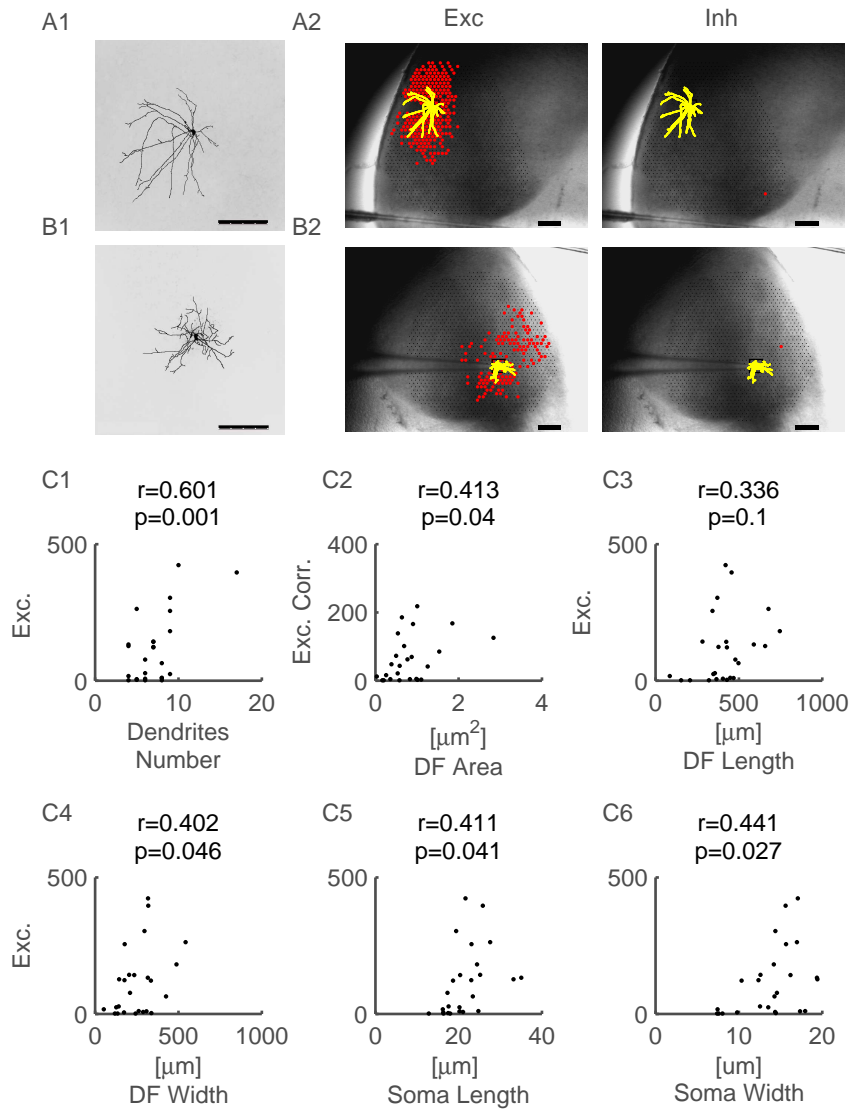


Figure 3.8: Intrinsic inputs related to morphological properties: **A & B**) Examples of confocal reconstructions of cells (A1, B1) superimposed with the excitatory input maps (A2, B2, left panel) and the inhibitory input maps (A2, B2, right panel). **C**) Correlation of the amount of excitatory intrinsic inputs (EPSCs, n=25) to dendritic number (C1), dendritic field length (C3), dendritic field width (C4), soma length (C5) and soma width (C6). Moreover, Correlation of the amount of excitatory inputs correction to dendritic field area (C2). Scale bars are 200 μm

innervations are at least to some extent depending on the parts of the cell that can receive the excitatory neuron transmitters, i.e. the cell surface size; the inhibitory innervations are depending on the types and density of the ion pumps and ion channels on the cell membrane, i.e. the membrane conductance.

3.2.4 Regional Heterogeneity

So far, our data has shown that intrinsic inputs were significantly correlated with morphological and electrophysiological parameters. Next we asked how the IC's intrinsic innervation of cells depends on their location within the ROI. Our study was done with respect to the amount of inputs, the distribution of inputs over distance, the innervation size and the innervation orientation. We had tested several ways of clustering cells according to their anatomical locations, and found that a partitioning into the dorso-medial region of the ICc (n=9), the ventro-lateral region of the ICc (n=7), the lateral region of the ICc (n=7) and the ICx (n=10) resulted in the most obvious regional heterogeneity as described in the following subsections. One cell was excluded from the regional difference statistic, because it was located on the boundary of the lateral ICc and ICx, which made it difficult to classify it into a specific region.

3.2.4.1 Innervation Orientation

We have defined the intrinsic inputs as the on-points within the significance field (Section 3.2.2, $p < 0.05$), which means that the significance field serves to build an outline for the intrinsic inputs. Thus, we can refer to the significance field as the intrinsic innervation field, in short *innervation field*. The orientation

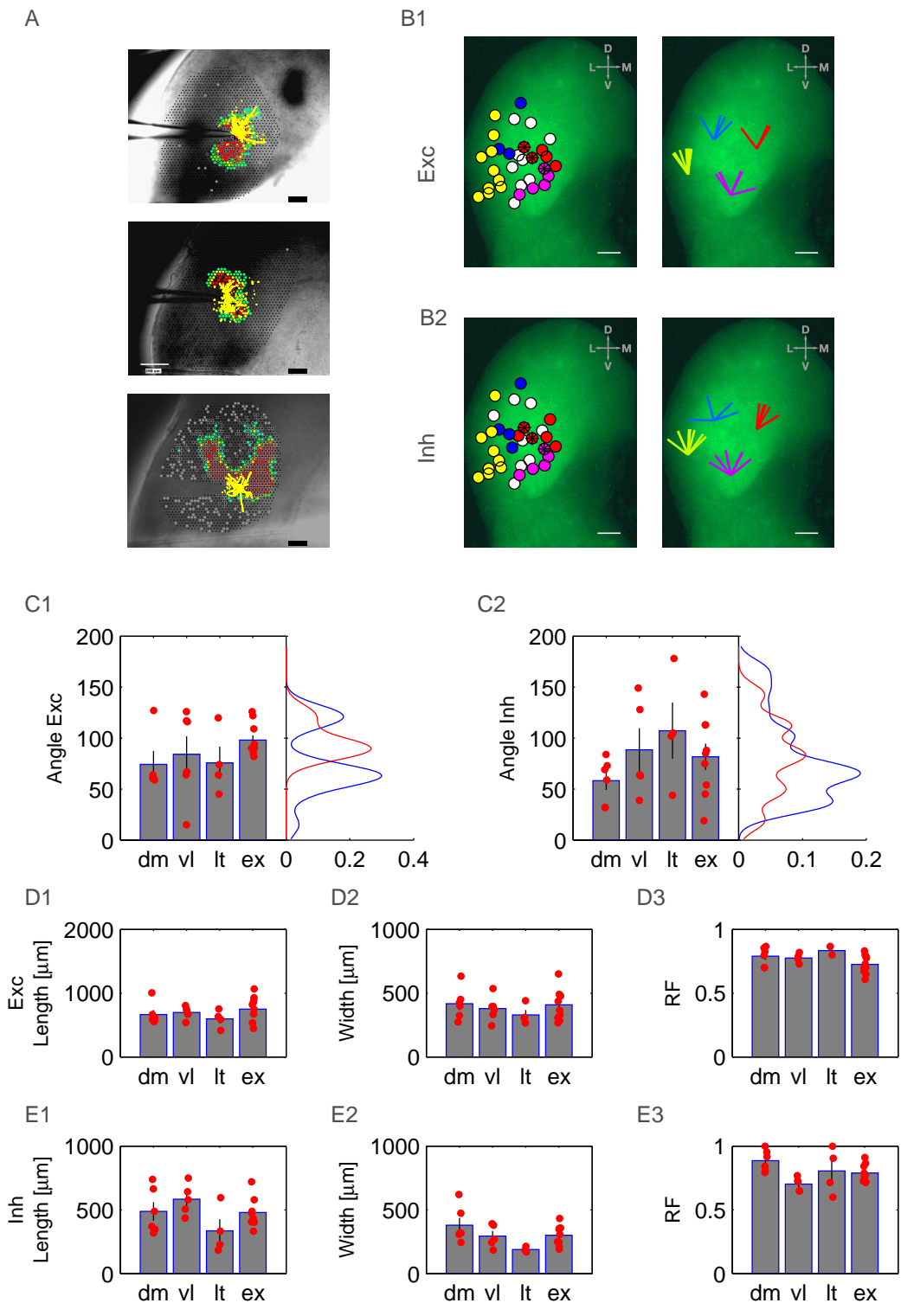


Figure 3.9: Orientations of intrinsic innervations ... (continued on the next page)

Figure 3.9: (continued from the previous page)... **A)** Examples of cell innervation orientations oriented along approx. 60° (top), oriented along approx. 120° (middle) and cells with two innervation orientations at both angles (bottom). Scale bar = $200\ \mu\text{m}$ **B)** Cells in different regions ($n=33$) are color-coded and mapped onto a standard IC slice with excitatory innervations (B1, left panel) and inhibitory innervations (B2, left panel); red: dorso-medial ICc, magenta: ventro-lateral ICc, blue: lateral ICc, yellow: ICx, white: cells have no significance map (or too diffused significance map to measure innervation orientations). The three example cells in (A) are marked in addition with black stars (B1 and B2, left panel). Orientations of cells were plotted as unit vectors in the case of excitation (B1, right panel) and inhibition (B2, right panel). D=dorsal, V=ventral, L=lateral, M=medial. Scale bar is $300\ \mu\text{m}$. **C)** Bar graphs show the mean values of orientation (red points) for different regions (left). dm: dorso-medial ICc, vl: ventro-lateral ICc, lt: lateral ICc, ex: ICx. The distribution of orientation (right) in the ICc (blue) and ICx (red) in the case of excitation (C1) and inhibition (C2). **D, E)** Bar graphs show mean values of innervation field length (D1, E1), width (D2, E2) and roundness (D3, E3) of different regions in the case of excitation (D) and inhibition (E). B-E, dm ($n=9$), vl ($n=7$), lt ($n=7$), ex ($n=10$).

of an intrinsic innervation can be defined as the orientation of the longest axis of the innervation field.

A large amount of morphological studies in the ICc have shown the existence of fibrodendritic laminae, spanning from ventro-lateral to dorso-medial in the ICc (Geniec and Morest, 1971; Rockel and Jones, 1973a; Oliver, 1984; Faye-Lund, 1985; Zook and Casseday, 1985; Meininger et al., 1986; Oliver et al., 1991; Malmierca et al., 1993; Mylius et al., 2014). The physiological frequency-band laminae are built on the basis of these fibrodendritic laminae. The orientation of the fibrodendritic laminae (Rockel and Jones, 1973b) and frequency-band laminae (Merzenich and Reid, 1974) have been estimated to be 40° – 60° in the central regions, due to the laminae being curved (Rockel and Jones, 1973b; Merzenich and Reid, 1974). Additionally, it has been suggested in some electrophysiological studies that there is a main tonotopic axis spanning dorso-laterally – ventro-medially in the ICc (Oliver, 2005; Merzenich and Reid, 1974). We asked the question whether the intrinsic innervation pathways have preferred orientations or not, and if such orientations exist, how

they are arranged, especially in the ICc compared to the orientation of the isofrequency laminae sheets and the tonotopic axis.

In order to get an overview, cells were again mapped onto a standard IC slice (Fig. 3.9 B left panels) according to the four anatomical regions initially defined, i.e. dorso-medial ICc (red), ventro-lateral ICc (magenta), the lateral boundary of the ICc (blue) and the ICx (yellow). The innervation orientations of cells were simplified as unit vectors showing only the orientation regardless of the length of the innervation fields (Fig. 3.9 B right panels). For the cells that had two preferred orientations (2/33), each of the two orientations was used as if they were two separate cells originating from the same place. Cells that had no intrinsic inputs or too diffused intrinsic inputs to measure innervation orientations were excluded (Fig. 3.9 B, exc.: n=9, inh.: n=8). The innervation orientations were shown separately for excitation (Fig. 3.9 B1) and inhibition (Fig. 3.9 B2).

In addition, the measurements of each cell were plotted as red points in the column of their respective anatomical region to show the interval of orientation angles (exc.: Fig. 3.9 C1, inh.: Fig. 3.9 C2 left insets). In order to analyze the innervation orientations of cells in the ICc with a sufficient amount of samples, we first grouped the cells with innervation orientations from dorso-medial of ICc, ventro-lateral of ICc and the lateral boundary of the ICc together (n=13); the remaining cells were ICx cells (n=11). Then each orientation measurement was plotted as the expectation value of a normal distribution and with the measurement uncertainty as the deviation.

By summing up all measurements, we found that ICc cells had two preferred excitatory orientations, which appeared as two distinctly separated

peaks (Hartigan's dip test: $\text{dip}=0.132$, $p=0$, Fig. 3.9 C1, right inset, blue curve). The largest peak was oriented along $61 \pm 15^\circ$ and the second peak was oriented along $121 \pm 15^\circ$. The first orientation of 61° was similar to the orientation of the isofrequency laminae sheets documented in Rockel and Jones (1973b). The second orientation was in the direction dorso-laterally – ventro-medially, presumably in the direction of the tonotopic axis (Oliver, 2005; Merzenich and Reid, 1974). For the sake of better understanding, examples of typical excitatory innervation fields of ICc cells are shown in Figure 3.9 A, i.e. cells that prefer the first orientation (Fig. 3.9 A, top), the second orientation (Fig. 3.9 A, middle) and both orientations (Fig. 3.9 A, bottom). In case of inhibition, the innervation orientations were more dispersed (Hartigan's dip test: $\text{dip}=0.074$, $p=0.533$), which manifested in the data as two adjacent insignificance peaks at $34 \pm 15^\circ$ and $68 \pm 15^\circ$; however, the two peaks were insignificantly separated. (Fig. 3.9 C2, right inset, blue curve).

The ICx is reported to have three layers that are parallel to the surface of the IC (Rockel and Jones, 1973b; Mylius et al., 2014). Fig. 3.9 C1 (right inset, red curve) shows that most ICx cells are oriented unimodally along $90 \pm 15^\circ$ in case of excitation (Hartigan's dip test: $\text{dip}=0.0813$, $p=0.9$), which is in parallel to the boundary of the IC. In case of inhibition, the orientations seems to be more evenly distributed (Hartigan's dip test: $\text{dip}=0.102$, $p=0.10$), which shows as regular peaks distributing over all directions in 3.9 C2 (right inset, red curve).

In summary, we found that both ICc and ICx cells had preferred intrinsic orientation directions. The ICc in gerbils presumably got excitatory intrinsic inputs from both the direction of the fibrodendritic laminae and from the

tonotopic axis. The ICx cells presumably got excitatory intrinsic inputs from the direction parallel to the surface of the IC (Rockel and Jones, 1973b; Mylius et al., 2014), i.e. from along the orientation of the morphological layers in the ICx. Both The ICc and the ICx cells did not have a preferred direction for the inhibitory intrinsic inputs (Fig. 3.9 D,E).

3.2.4.2 Innervation Profiles

Apart from studying just the innervation orientation itself, we went one step further by analyzing also the regional differences in intrinsic innervation profiles, i.e. their parameters in terms of the amount of inputs, the distribution over distance the innervation size and roundness. For this, cells are clustered again into four regions according to their anatomical location as described in Section 3.2.4: the dorso-medial part of the ICc (n=9), the ventro-lateral part of the ICc (n=7), the lateral boundary of the ICc (n=7), and the ICx (n=10). The mean values and SEMs for the different regions can be found in Table 3.5 and will not be referenced in every sentence.

Amount of Intrinsic Innervation

Due to the large variance of the amount of inputs within some regions, an Anova test was not suitable for directly analyzing the significance of differences in the intrinsic inputs between regions (Fig. 3.11). However, our results indicated that the regions were heterogeneous with respect to their excitation-inhibition ratio. In addition, paired student t-tests applied to each pair of regions in some cases indicated additional regional heterogeneity with respect to the amount of intrinsic inputs. The p-values of these paired student t-tests can be found in Table 3.6.

Table 3.5: Regional heterogeneity of intrinsic inputs along with electrophysiological parameters, and their values for Pearson's correlation.

length [μm]	exc (n=33)						inh (n=33)									
	dm (n=9)		vl (n=7)		lt (n=7)		ex (n=10)		dm (n=9)		vl (n=7)		lt (n=7)		ex (n=10)	
	mean	SEM	mean	SEM	mean	SEM	mean	SEM	mean	SEM	mean	SEM	mean	SEM	mean	SEM
#input	62.22	24.12	146.86	57.18	24.85	10.82	190.70	39.51	47.56	20.75	19.86	6.31	10.43	3.82	17.30	4.21
length [μm]	665.00	69.85	695.66	37.13	596.50	70.20	748.60	63.21	487.66	72.40	583.00	54.33	335.25	91.90	478.89	37.88
width [μm]	417.50	50.65	378.50	39.02	329.75	37.99	408.50	37.97	380.00	57.09	294.20	39.97	189.25	9.14	299.67	26.66
RF	0.79	0.0302	0.78	0.0189	0.83	0.0330	0.72	0.0228	0.886	0.0338	0.702	0.0237	0.804	0.0906	0.78	0.0232
	dm (n=9)			vl (n=7)			lt (n=7)			ex (n=10)						
mean	SEM	mean	SEM	mean	SEM	mean	SEM	mean	SEM	mean	SEM	mean	SEM			
C_m [pF]	89.33	11.65	136.43	27.51	123.57	26.88	170.40	37.12								
R_m [M Ω]	311.11	59.60	183.29	25.44	332.57	44.89	290.70	61.25								
G_m [nS]	4.37	0.9	6.11	0.83	3.38	0.47	5.28	1.18								
τ [ms]	26.52	5.56	24.28	3.50	38.14	7.72	34.10	3.59								
Pearson's correlation	dm (n=9)			vl (n=7)			lt (n=7)			ex (n=10)						
exc	inh	exc	inh	exc	inh	exc	inh	exc	inh	exc	inh					
C_m	0.39	-	0.83	-	0.22	-	0.55	-								
p	0.30	-	0.02	-	0.63	-	0.10	-								
R_m	-	-0.52	-	0.21	-	0.18	-	$2 \cdot 10^{-4}$								
p	-	0.14	-	0.64	-	0.70	-	0.99								
G_m	-	0.54	-	0.15	-	-0.08	-	0.30								
p	-	0.14	-	0.75	-	0.75	-	0.40								
τ	-	-0.52	-	0.58	-	0.77	-	-0.53								
p	-	0.14	-	0.16	-	0.04	-	0.11								

In cases where no differences in the mean values of the intrinsic inputs in the paired regions were found, F-tests were applied (Table 3.7) to further see, whether these regions were different in the variance of the intrinsic inputs. This was done, because it has been previously shown that the excitatory inputs were correlated to the effective cells size. Thus a significantly larger variance of excitatory inputs within a region compared to another region could mean that in this region, cells also have a larger variance in the effective cell surface, whereas in the compared region, the effective cell surface are more similar. Analog in the case of inhibitory inputs, which are correlated to the membrane conductance of the cells, a significantly larger variance of inhibitory inputs within a region compared to another thus could mean that in this region, cells have a larger variance in their membrane conductance than compared region.

In the dorso-medial ICc, cells were almost balanced in the amount of excitatory and inhibitory inputs (mean values: exc.:inh. = 1.3:1, paired student t-test, $p=0.65$), and the radial density of excitatory inputs and inhibition inputs were similar as well (Fig. 3.10 A). Therefore, the dorso-medial ICc region was used as a reference point when comparing the differences in the amount of intrinsic inputs with the other regions.

Cells in the ventro-lateral ICc showed a prevalence in the amount of excitatory inputs compared to the inhibition (mean values: exc.:inh. = 7.39:1, paired student t-test, $p<0.05$). This could also be observed in the radial density of excitatory inputs over distance being much higher than the inhibitory one (Fig. 3.10 B). We found no significant difference of the ventro-lateral ICc cells to the dorso-medial ICc cells both in the amount of excitatory inputs (paired student t-test, $p=0.16$) and in the amount of inhibitory inputs (paired

student t-test, $p=0.27$). However, in the case of inhibition, the ventro-lateral ICc cells showed a significantly smaller variance in the amount of inhibitory inputs (F-test, $p=0.005$) than the dorso-medial ICc cells. This suggests that the dorso-medial ICc cells vary a lot in their membrane conductance, whereas the ventro-lateral ICc cells are more similar in their membrane conductance.

Table 3.6: Paired student t-tests on the intrinsic inputs and electrophysiological parameters according to regions

paired t-test p-values	dm vs.			vl vs.		dl vs.		ex vs.
	vl	dl	ex	dl	ex	ex	dm&vl	IC
#exc	0.16	0.22	0.15	0.06	0.05	$4 \cdot 10^{-3}$	0.11	0.01
#inh	0.27	0.14	0.15	0.22	-	0.26	0.06	-
#diff	0.09	-	0.11	0.06	-	0.06	-	$9 \cdot 10^{-3}$
C_m	0.10	0.22	0.06	-	-	-	-	-
G_m	0.18	-	-	0.21	-	0.21	0.10	0.24
R_m	0.09	-	-	0.01	0.18	-	0.24	-
τ	-	0.23	0.25	0.12	0.07	-	0.09	-

Only p-values of the paired student t-tests are shown if $p < 0.05$, i.e. the pairs have a significant difference in mean values. P-values larger than 0.3 are shown as "-". Dorso-medial ICc (dm, $n=9$), ventro-lateral ICc (vl, $n=7$), lateral ICc (lt, $n=7$), ICx (ex, $n=10$)

Cells in the lateral ICc showed no significant difference in the amount of excitatory and inhibitory inputs (paired student t-test, $p=0.44$), as well as the radial density of inputs were similar for excitation and inhibition over distance as in the dorso-medial ICc (Fig. 3.10 A). Even without significant difference to the dorso-medial ICc with respect to the mean values of both the excitatory inputs (paired student t-test, $p=0.22$) and the inhibitory inputs (paired student t-test, $p=0.14$), however, cells in the lateral ICc had a smaller variance in both the cases of excitation (F-test, $p=4 \times 10^{-2}$) and inhibition (F-test, $p=3 \times 10^{-4}$) compared to the dorso-medial ICc. This suggests that

Table 3.7: F-tests on the intrinsic inputs and electrophysiological parameters according to regions

F-test p-values	dm vs.			vl vs.		dl vs.		ex vs.
	vl	dl	ex	dl	ex	ex	dm&vl	IC
#exc	0.06	0.04	-	$7 \cdot 10^{-4}$	-	-	0.02	-
#inh	$5 \cdot 10^{-3}$	$3 \cdot 10^{-4}$	$1 \cdot 10^{-4}$	-	-	-	$1 \cdot 10^{-3}$	0.01
C_m	0.06	0.07	$2 \cdot 10^{-3}$	-	-	-	-	-
G_m	-	0.07	-	-	-	0.02	0.08	0.07
R_m	0.03	-	-	-	0.02	-	-	-
τ	-	-	-	0.08	-	-	-	-

Tests were only made on the paired subdivisions that showed no significant difference in mean values. Only p-values of the F-test are shown if $p < 0.05$, i.e. the pairs have a significant difference in the variance. P-values larger than 0.1 or no F-test performed are shown as "-". . Dorso-medial ICc (dm, n=9), ventro-lateral ICc (vl, n=7), lateral ICc (lt, n=7) , ICx (ex, n=10)

cells in the lateral ICc are more similar in the effective cell surface and in their membrane conductance than cells in the dorso-medial ICc. Compared to the other regions, cells in the lateral ICc showed a trend of acquiring smaller amounts of excitatory inputs than in the ventro-lateral ICc (paired student t-test, $p=0.06$), and smaller amounts of inhibitory inputs than in the rest of the ICc, i.e. the combined data of the dorso-medial ICc and the ventro-lateral ICc (paired student t-test, $p=0.06$).

The cells in the ICx showed a dominance of local excitation over inhibition (mean values: exc.:inh. = 11:1, paired student t-test, $p=0$), which could also be observed in the comparison of radial density of excitatory inputs and inhibitory inputs in the ICx (Fig. 3.10, C). Compared to cells in the rest of the ICc (the combined data of the dorso-medial ICc, the ventro-lateral ICc and the lateral ICc), the cells in the ICx had a significantly larger amount of excitatory inputs (paired student t-test, $p=0.01$). Especially, the ICx and the adjacent region, i.e. the lateral ICc, are parallel to each other, but could be

distinguished from each other (paired student t-test, $p=0.004$) by the high difference in the excitatory inputs (mean values, ICx:lateral ICc = 8:1). Besides, the ICx cells showed a trend of receiving larger excitatory inputs than the cells in the ventro-lateral ICc (paired student t-test, $p=0.05$), but they showed no significantly different to the the dorso-medial ICc cells (paired student t-test, $p=0.15$) in the case of excitation.

In contrast, in the case of inhibition, the ICx cells showed neither a significant difference to individual regions within the ICc nor to the combined data of the ICc (Table 3.6). However, cells in the ICx showed a smaller variance in the case of inhibition compared to the combined data of the ICc (F-test, $p=0.01$). Compared to individual regions, the variance was especially different to the dorso-medial ICc (F-test, $p=1 \times 10^{-4}$). This suggests that cells in the ICx have less variance in membrane conductance compared to cells in the ICc, especially compared to cells in the dorso-medial ICc in the case of inhibition.

Thus in summary, cells received a balanced ratio of excitatory and inhibitory inputs in the dorso-media ICc, whereas in the ICx and the ventro-lateral ICc, the excitations were dominant. In the lateral ICc, cells showed no significant difference with respect to the excitatory-inhibitory ratio. Additionally, cells showed different variances in most paired-regions in both the cases of excitation and inhibition.

Intrinsic Innervation Distance

As previous studies have shown that the width of the fibro-dendritic lamina within the ICc is around 150 μm (Zook and Casseday, 1985; Malmierca et al., 1993), we were interested in the question, whether the intrinsic inputs are constrained within the lamina. For this purpose, we studied the length and width of the intrinsic input fields.

The mean values of the excitatory innervation field length were approx. 600–750 μm , and the mean values of the field width 330–420 μm (Fig. 3.9 D, Table 3.5) in both ICc and ICx. The length measurements of the innervation field were corresponding to the innervation distances (see Figure 3.10), i.e. the radius of the innervation field was between 300 and 350 μm . Since our data indicated that a majority of cells in the ICc were orientated in the direction of the isofrequency lamina, i.e. approx. 61° (some were oriented at 120°), the results thus suggest that the excitatory innervation field is covering more isofrequency laminae. The inhibitory innervation fields were 330–600 μm in length and 300–380 μm in width, apart from 189 μm in the lateral ICc (Fig. 3.9 E, Table 3.5). Because the inhibitory innervation in the ICc have been suggested to be dispersed, also in the directions approximately perpendicular to the fibro-dendritic lamina, it is thus possible that the inhibitory innervations are not constrained within the isofrequency band, or fibro-dendritic lamina, which is 100–150 μm wide (Sturm et al., 2014; Shneiderman and Henkel, 1987; Malmierca et al., 1993; Fathke and Gabriele, 2009; Wallace et al., 2013). Thus, ICc cells received both excitation and inhibition not only from the same frequency band, but also from bands of neighbouring frequencies.

Further we analyzed the regional differences in the dendritic field length,

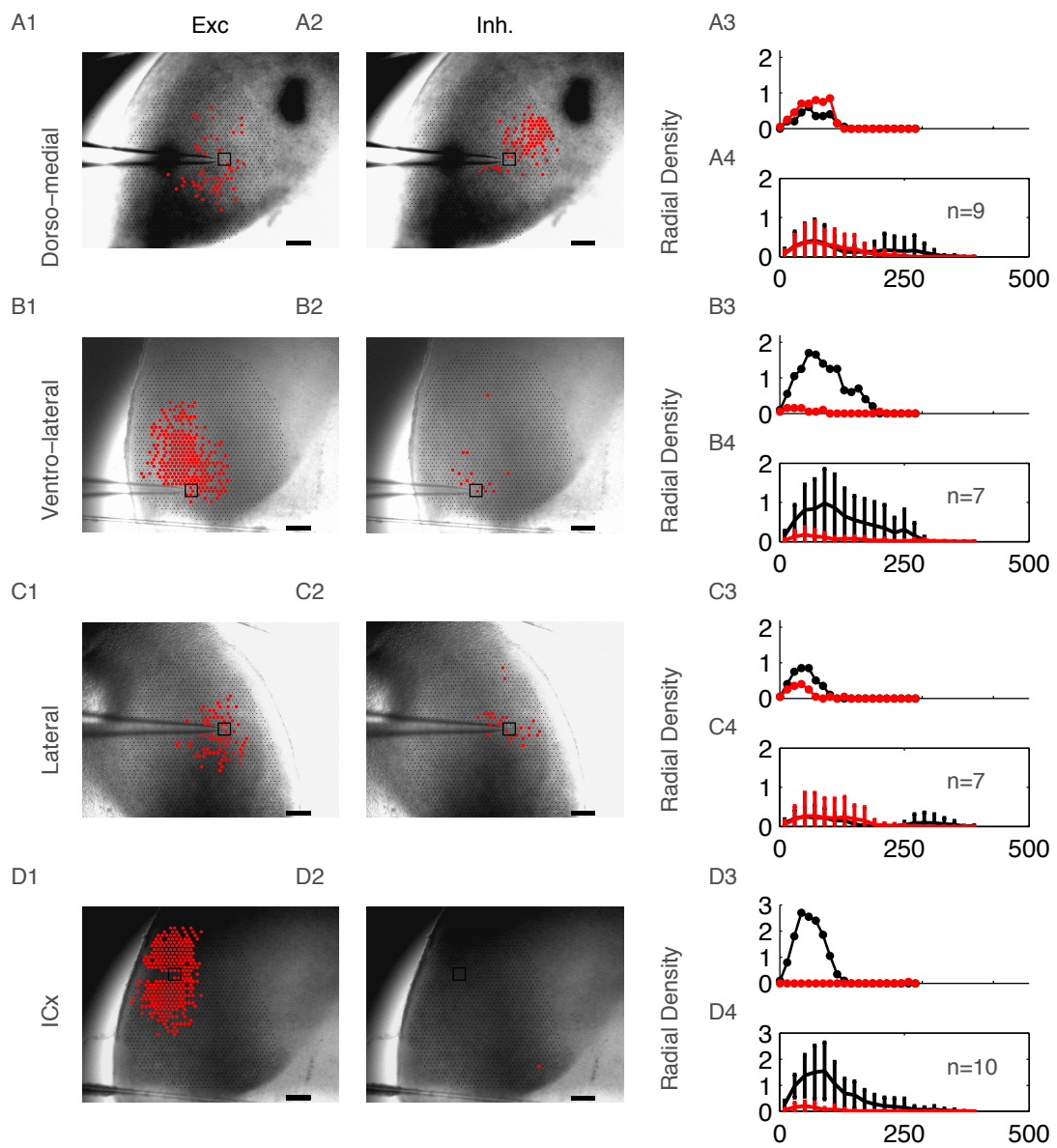


Figure 3.10: Radial density of intrinsic inputs according to regions. Examples of EPSC (A1, B1, C1, D1) and IPSC (A2, B2, C2, D2) input maps of a dorso-medial (A), a ventro-lateral (B), a lateral ICc (C) and an ICx (D) cell. Black dots are the stimulated points. Red dots are the intrinsic inputs. Scale bars=200 μm . Distance distribution of significant inputs for the example maps (A3, B3, C3, D3), and average distance distribution (A4, B4, C4, D4) for dorso-medial (A4, n=9), ventro-lateral (B4, n=7), lateral (C4, n=7) ICc and ICx cells (C4, n=10); black for excitation, red for inhibition. Error bars indicate SEM (Yassin et al., 2015).

width and the roundness factors, which are shown in Fig. 3.9. We found that the dendritic field width of the lateral ICc cells was significantly smaller than that of dorso-medial ICc (paired student t-test, $p=0.03$) and ICx cells (paired student t-test, $p=0.02$). Besides, the input field length of the lateral ICc cells was significantly smaller than that of ventro-lateral ICc cells (paired student t-test, $p=0.002$), however, showed only a trend of a smaller input field width than that of ventro-lateral ICc cells (paired student t-test, $p=0.06$). This indicated that even if there were no significant differences between the lateral ICc, the ventro-lateral ICc and the dorso-medial ICc in the amount of inhibitory inputs, however, the input fields differed in their form between the regions.

Besides that, the input field roundness factor of the dorso-medial ICc cells was significantly larger than that of the ventro-lateral ICc (paired student t-test, $p=0.002$) and ICx cells (paired student t-test, $p=0.03$) in case of inhibition. In more detail, the mean values of the input fields of the ventro-lateral ICc cells were $583 \pm 54 \mu\text{m}$ in length and $294 \pm 40 \mu\text{m}$ in width, which resulted in a roundness factor (RF) of 0.49 ± 0.03 (Fig. 3.9 E1, E2), and a very sparse radial density as shown in (Fig. 3.10, B). Dorso-medial cells had a slightly shorter ($487 \pm 72 \mu\text{m}$) and wider input field in mean values ($380 \pm 57 \mu\text{m}$), which led to an almost round input field (RF: 0.79 ± 0.06) and a high radial density (Fig. 3.10, A), even though the mean amount of inhibitory inputs in the dorso-medial ICc varies two times more. Thus, this means that the dorso-medial ICc cells are not only different in the variance of the inhibitory inputs, but also different in the form of the inhibitory inputs field.

Moreover, the input field roundness factor of the ventro-lateral ICc cells

(RF: 0.49 ± 0.03) was significantly smaller than that of the ICx cells (RF: 0.63 ± 0.04) in case of inhibition, which showed that the roundness factors of the input fields were different in the two regions. Thus, these results confirmed that the inputs were distributed differently in some regions. Besides of these, all other regions showed no significant difference between each other in the dendritic length, width and roundness factors.

Thus, we can conclude that the innervations of excitation and inhibition can have quite different organizations in terms of their orientation, amount, form and distance of the innervation fields.

Innervation Heterogeneity Compared with Electrophysiology

In order to get a deeper understanding of the regional differences of the intrinsic inputs, we also analyzed the correlations of intrinsic inputs to electrophysiological parameters, i.e. the membrane capacitance, the input resistance, the membrane conductance and the membrane time constant in the different regions (Table 3.5). Additionally, the electrophysiological parameters between regions were compared pairwise using paired student t-test in order to find regional differences in the electrophysiological parameters themselves. The p-values of the paired student t-tests can be find in Table 3.6 and the mean values are shown in Fig.3.11, which will not be referenced in every sentence.

Cells in the dorso-medial ICc showed only a trend of larger input resistances than in the ventro-lateral ICc (paired student t-test, $h=0$, $p=0.09$); however, this trend was confirmed by a previous electrophysiological study ((Yassin et al., 2015, unpublished)). The difference in the results was that with a larger sample size ($n=16$ for each region), Yassin et al. (2015, unpublished) have shown that the p-value of the differences in input resistance between the two

regions have been less than 0.001. Additionally, they also have found that the membrane time constant has been significantly larger in the dorso-medial ICc cells than in the cells in the ventro-lateral ICc, however, no significant difference could be found in our results (see Table 3.6). The difference in the results can also be due to the previous study ((Yassin et al., 2015, unpublished)) having been conducted at a different temperature.

Cells in the ventro-lateral ICc did not show any significant difference to any other region electrophysiologically (see Table 3.6). However, whereas our results have already shown correlations between electrophysiological parameters and the amount of intrinsic inputs (see Section 3.2.3) for the whole data set of the IC in general, only the cells in the ventro-lateral ICc showed a correlation between the membrane capacitance and excitatory inputs significantly (Pearson's correlation, $r=0.827$, $p=0.02$). Cells in the dorso-medial ICc (Pearson's correlation, $r=0.39$, $p=0.30$), the lateral ICc (Pearson's correlation, $r=0.22$, $p=0.63$) and ICx (Pearson's correlation, $r=0.55$, $p=0.10$) did not show significant correlations between the two parameters. The results indicated that the excitatory inputs of the ventro-lateral ICc cells had strong correlations with the effective cell surface than the compared regions.

The lateral ICc cells had significantly less input resistance than the ventro-lateral ICc cells (paired student t-test, $p=0.01$). Besides, The lateral ICc cells showed a trend of a larger membrane time constant compared to the rests of the ICc (the combined data of the ventro-lateral ICc and the dorso-medial ICc) (paired student t-test, $p=0.09$). Moreover, it was already generally shown that the membrane time constant had a weak negative correlation with the inhibitory inputs ($r=-0.37$, Fig.3.7, E); however, the lateral ICc was the only

region that showed a positive correlation significantly (Pearson's correlation, $r=0.77$, $p=0.04$). In all other regions, the correlations were not significant. Moreover, the lateral ICc was the only region that cells did not show the positive correlation (Pearson's correlation, $r=0.22$, $p=0.63$) between their amount of excitatory inputs and membrane capacitance as they are in general. The rest of ICc (the combined data of the dorso-medial ICc the ventro-lateral ICc) showed this correlation with high significance (Pearson's correlation, $r=0.77$, $p=5e-4$), as well as the ICx showed a trend of significant correlation (Pearson's correlation, $r=0.55$, $p=0.096$).

Cells in the ICx showed only a trend of larger membrane capacitance (paired student t-test, $p=0.06$) compared to the dorso-medial ICc, and they also showed a trend of larger membrane time constant compared to the ventro-lateral ICc (paired student t-test, $p=0.07$).

Our overall results hence indicated that even if in general the apparent cell surface, i.e. the membrane capacitance and the cell membrane permeability were correlated with the intrinsic excitatory and inhibitory inputs, respectively, this correlation was not consistent in all regions. Thus, cells with different effective size and synaptic properties could be distributed differently within the ROI, which might help the cells to perform different functions.

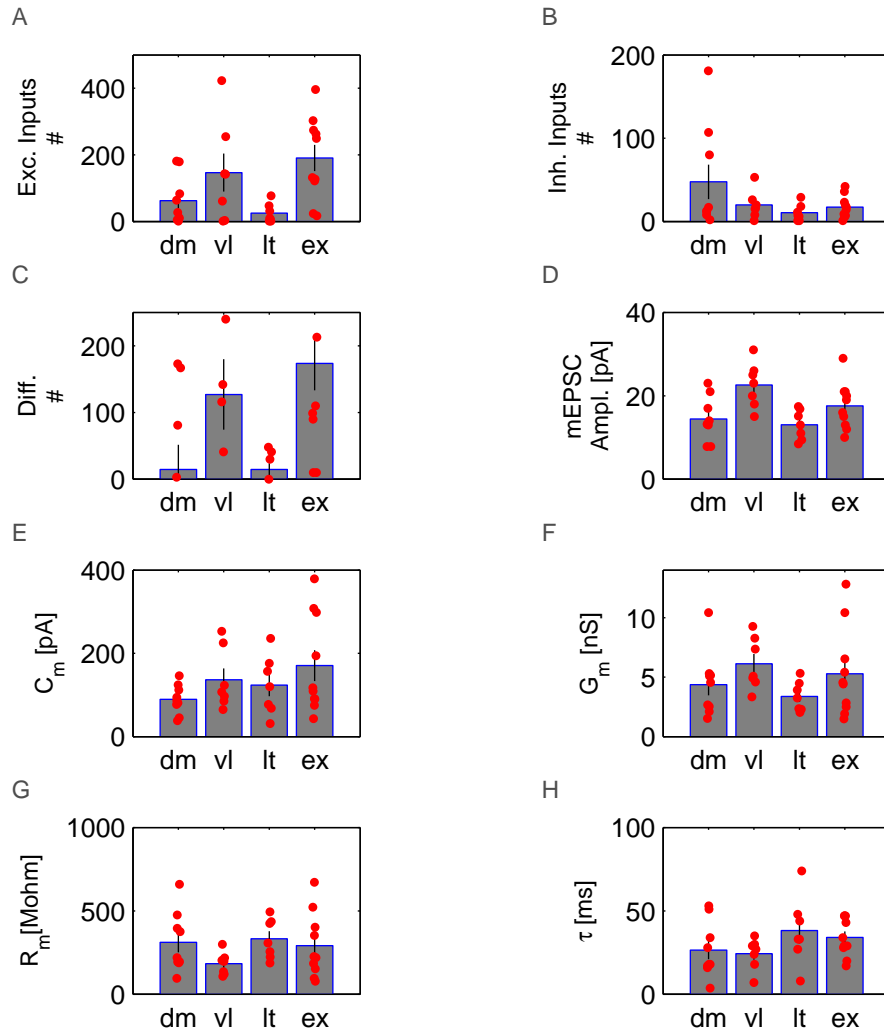


Figure 3.11: Regional heterogeneity of intrinsic inputs and electrophysiological parameters. Bar graphs show the mean values of the amount of excitatory intrinsic inputs (A), the amount of excitatory intrinsic inputs (B), the difference in amount of excitatory and inhibitory inputs (C), the mEPSC amplitudes (D), the membrane capacitance (E), the membrane conductance (F), the input resistance (G) and the membrane time constant (H) of cells from the four anatomical regions, i.e. the dorso-medial (dm, n=9), ventro-lateral (vl, n=7), lateral (lt, n=7) ICc as well as the ICx (ex, n=10) neurons.

4 Discussion

The IC is known as an important integration center in the auditory ascending and descending pathways (Faye-Lund, 1985), and has a pivotal computational role in the auditory system. Despite this fact, the intrinsic functional structure, i.e. the synaptic connectivity in the IC, which is underlying the neuronal computations, is still poorly understood. Several studies so far have given indications on the intrinsic structure of the IC (Chen et al., 2012; Mei et al., 2013; Ress and Chandrasekaran, 2013). However, only one recent study has reported the synaptic connectivity in more detail: The intrinsic maps of the individual ICc neurons have an ellipse form, are continuous, span over a few frequency bands and align solely in the direction of the isofrequency axis of the ICc (Chandrasekaran et al., 2013).

This thesis made further efforts to assess the intrinsic structure of the IC neurons using scanning photostimulation of caged glutamate (Bendels et al., 2010), so that with this method, the locations of all pre-synaptic partners of the neurons from the region of interest (ROI) form an intrinsic map. The first main aspect of our study specifically aimed at investigating the regional differences of such intrinsic networks. For this purpose, the ROI was divided into four morphological subregions that showed the most regional heterogeneity in the

aspects of size, shape, amount and orientation of the intrinsic networks as well as the ratio between excitatory and inhibitory inputs.

Another main aspect of this study was to find the correlations between the neuronal intrinsic networks and the electrophysiological and anatomical properties of the neurons. For this purpose, we at first determined the electrophysiological properties of the neurons, the morphology of the neurons and the anatomical position of the neurons. Then, we calculated the correlations of all parameters as well.

Our ROI had to be restricted to a part of the IC due to technical reasons. Therefore, we focused on the ICc and the ICx as they deemed most interesting being the regions receiving integrative inputs from both the lower brainstem and the multi-sensory system respectively.

4.1 Intrinsic Innervation Organization:

Dorso-medial ICc vs. Ventro-lateral ICc

Although the ventro-lateral ICc and the dorso-medial ICc subregions are similar in terms of morphological fibro-dendritic laminae (e.g. Rockel and Jones, 1973c) and tonotopic organization, and although both get ascending inputs from all nuclei in the lower auditory brainstem, they are also different in some aspects.

Anatomically, different studies have shown that the primary auditory cortex projects mainly to the dorso-medial ICc, but less to the ventro-lateral ICc (Bajo et al., 2007; Saldana and Merchan, 1992). Electrophysiologically, a latency gradient of evoked responses in the ICc along the isofrequency axis has been

reported in vivo (Hattori and Suga, 1997) and in vitro (Reetz and Ehret, 1999; Chandrasekaran et al., 2013), with the assumption of intrinsic cascaded ICc feed-forward networks (Miller et al., 2005; Chandrasekaran et al., 2013). This means for example, that neurons in the dorso-medial ICc experience long latencies in response to stimulation compared to cells in the ventro-lateral ICc (Yassin et al., 2015, unpublished).

In addition to the results of previous studies, this thesis found that the intrinsic innervations of dorso-medial ICc and ventro-lateral ICc cells had a similar innervation distance of approx. 200–300 μm . However, whereas the dorso-medial ICc cells were almost equal in excitation and inhibition in terms of the mean number of inputs (see Section 3.2.4.2), in the ventro-lateral ICc, cells showed a strong prevalence of excitation (see Section 3.2.4.2 and Yassin et al. (2015, unpublished)). Additionally, the ventro-lateral ICc cells had a larger variance in the number of inhibitory inputs compared to the dorso-medial ICc cells. This suggests that the dorso-medial ICc cells vary large in their membrane conductance, whereas the ventro-lateral ICc cells are more similar in their membrane conductance. Differences had also been shown electrophysiologically, as cells in the ventro-lateral ICc had a significant correlation between the membrane capacitance and the amount of excitatory inputs, whereas cells in the dorso-medial ICc did not show such a significant correlation.

As there have been no direct studies of the regional differences in intrinsic inputs in the IC so far, we were looking for indications from other studies that would indirectly support the observation of differences between the dorso-medial ICc and the ventro-lateral ICc. For inhibition, some studies have shown relatively higher levels of glutamate decarboxylase (GAD) (Adams and

Wenthold, 1979) or gamma-aminobutyric acid (GABA) receptors (Fubara et al., 1996) in the dorso-medial ICc compared to the ventro-lateral ICc, whereas the glycine levels are almost the same ventro-laterally to dorso-medially (Fubara et al., 1996; Merchan et al., 2005). Consequently, these can suggest the prevalence of inhibition in the dorso-medial ICc cells compared to the ventro-lateral ICc.

In contrast, for excitation, Adams (1979) has shown that the glutamate transmitter level is slightly lower in the ventro-lateral than in the dorso-medial ICc. This could be due to the feed-forward network in the ventro-lateral ICc relaying the glutamate projections into the dorso-medial ICc, whereas the dorso-medial ICc has more recurrent networks that retain the projections in itself. Another possibility is that the excitatory inputs are related more to the effective size of the neurons (Fig. 3.8 D1-D3, Fig. 3.7 C) than the membrane conductance, so that the level of the excitatory neurotransmitters can not be used to explain the amount of excitatory inputs.

Nevertheless, we found no significant difference between the dorso-medial ICc and the ventro-lateral ICc, neither in case of excitation nor inhibition. Moreover, a comparison of the levels of excitatory and inhibitory neurotransmitters does not directly correspond to the excitation-inhibition ratio within a region. Thus, the excitation-inhibition ratio differences between the dorso-medial ICc and the ventro-lateral ICc shown in our results can not be supported directly by the biochemical studies.

Morphologically, there have been two studies that particularly pay attention to the differences between the two regions. Reetz and Ehret (1999) have reported that the dendritic tree of the ventral cells is larger than that of the

dorsal cells, and Rockel and Jones (1973b) have reported that the dorso-medial ICc consists mainly of large cells, and the ventro-lateral ICc consists of mainly medium and small cells but with some intermingled larger types. Due to the positive correlation of the effective cells sizes and the excitatory inputs in our results, indications of a large variance of cells size in previous studies could hence suggest also a large variance of excitatory inputs of ventro-lateral ICc cells compared to dorso-medial ICc cells.

However, how the differences in intrinsic inputs between the dorso-medial ICc and the ventro-lateral ICc are potentially related to their functions is unclear. What can be presumed so far from the neuronal projections is that as the ventro-lateral ICc is the entry point of ascending inputs (Chandrasekaran et al., 2013), a combination of large excitatory innervation and small inhibitory innervation there could favor the integration of different pathways, in order to relay in the cascade feed-forward network upstream further. In contrast, anatomically, the primary auditory cortex projects mainly to the dorso-medial ICc, but not to the ventro-lateral ICc or at least only to a limited extent (Bajo et al., 2007; Saldana and Merchan, 1992). Therefore, as a region receiving cortical feedback (Bajo and King, 2012), it can be assumed that the dorso-medial ICc is a region with more interaction between the excitation and inhibition, and thus more inhibition exists than in the other regions of the IC. This matches our results of a balanced excitation and inhibition in the dorso-medial ICc and dominant excitation in the ventro-lateral ICc.

4.2 Region of Distinct Intrinsic Innervation:

Lateral ICc?

Compared to the just discussed terms *ventro-lateral ICc* and *dorso-medial ICc*, which have been already referred to in some previous studies before (e.g. Adams, 1979; Rockel and Jones, 1973b; Yassin et al., 2015), the term *lateral ICc* has not been directly mentioned yet, even though there have been already some studies hinting at a regional heterogeneity in this area both morphologically (Saldana and Merchan, 1992) and functionally (Cant and Benson, 2006). Our data now has confirmed that a lateral ICc region, which is located at the lateral boundary of the ICc, directly adjacent and parallel to the ICx, is clearly distinguishable from other parts of the ICc not only in terms of the profile of the intrinsic innervation of the cells there, but also in terms of their correlations to some electrophysiological membrane properties.

In case of inhibition, the lateral ICc was the only region that did not show the same negative correlation between the inhibitory inputs and membrane time constant as observed in the whole dataset of the IC. In case of excitation, the lateral ICc was the only region that largely contradicted the correlation between the amount of excitatory inputs and membrane capacitance. All other regions were consistent with the correlation in that the rest of the IC, i.e. the combined data of ventro-lateral ICc and the dorso-medial ICc, showed this correlation with high significance as well as the ICx showed a trend of correlation (see Section 3.2.4.2).

There have been no morphological studies about ICc cells so far that would point at cells in the lateral ICc being any different than in other regions within

the ICc, at least not with respect to morphological cell type, dendritic fields size or soma morphology (Mylius et al., 2013; Rockel and Jones, 1973b). There have been also no other electrophysiological studies that have pointed out any differences in the membrane properties of lateral ICc cells in comparison to other regions (e.g. Li et al., 1998), which could mean that either the region is not specific in the distribution of cell size and membrane parameters, or that none of these studies has attempted to find out the specific differences of this particular region. Hence, we cannot draw a final conclusion with respect to the cell properties itself.

However, there have been a few studies that have shown that the lateral ICc region might be different in other aspects. Studies of the intrinsic connections of the cells (Saldana and Merchan, 1992) by means of injecting anterograde tracer have shown that observable differences in this area can indeed be found in the rat IC. The isofrequency bands have been labeled this way appear to be getting narrower and even disappearing towards the area that is corresponding to the area of our lateral ICc. This could be an indication towards a narrower intrinsic input area that is based on smaller dendritic fields of cells, but this indication is still far away from providing enough supporting evidence of less intrinsic innervations in this area.

Nevertheless, biochemical studies of inhibitory receptors have shown a comparably clear difference between the lateral ICc and the rest of the ICc. Fubara et al. (see Fubara et al., 1996, Figure 3) have shown an almost complete lack of GABA receptors in the lateral ICc area, which would be consistent to our observation of the trend of a lack of intrinsic inhibitory inputs in the lateral ICc compared to the rest of the ICc (see Section 3.2.4.2).

Another important support for a dedicated lateral ICc subregion is the fact that the lateral ICc region can be distinguished from other regions of the ICc in terms of their potential functional sub-domains. By labelling IC cells of gerbils with retrograde tracer, Cant and Benson (2006) have shown that even if all ICc cells receive inputs from the CN, the LL and the superior paraolivary nuclei, cells receiving additional ascending inputs from the LSO and the MSO are located more laterally in the ICc in gerbils (Cant and Benson, 2006). Especially on the transverse slices cut through the middle of the IC (see Cant and Benson, 2006, Figure 5, T720), which is corresponding to the depth of our slices, the regions receiving additional ascending inputs from LSO and MSO inputs are very narrow areas in the lateral part of the ICc (Cant and Benson, 2006). This area corresponds to the notion of a lateral ICc in this thesis.

The above studies indicate that the lateral ICc distinguishes itself from the other regions of the ICc, because it receives integration from more afferent nuclei, which means that it integrates more different types of afferent inputs from different sources. It is supposed that an integration of multiple innervation inputs might be enhanced by slow processing (Robards, 1979; Zhou and Shore, 2006; Chandrasekaran et al., 2013), i.e., the large membrane time constant of cells in this region compared to the rest of the ICc in our results. This leaves questions for future work to see whether the small amount of innervation in the lateral ICc is related to frequency processing, due to overlapping of multiple functional domains or due to completely different reasons.

A further implication of the finding of the lateral ICc as a clearly distinguishable innervation subregion in this thesis is that it provides another possibility of defining the border between ICc and ICx, in addition to the commonly used

anatomical definition of the ICc, using fibro-dendritic laminae.

4.3 Intrinsic Innervation Orientation:

Iso-frequency Axis, Tonotopy Axis or both?

As initially mentioned, studies on intrinsic innervations in the ICc are rare. The most related study from Sturm et al. (2014) recently has reported that both excitatory and inhibitory intrinsic networks in the rat ICc are oriented solely following the direction of the curvature of the isofrequency contour in the rat (Sturm et al., 2014). In this thesis we found that in fact ICc cells had two preferred innervation orientations. In the case of excitation, the majority of cells from the ICc had intrinsic innervations aligned approx. 60° to the horizontal axis, which is presumably the isofrequency axis (Rockel and Jones, 1973c), whereas the minority of cells had an orientation of approx. 120° to the horizontal axis, which is presumably in line with the tonotopic axis in gerbils (Oliver, 2005; Merzenich and Reid, 1974). Additionally there were a few cells taking intrinsic innervations from both axes. On the contrary, the inhibition innervation orientation of the ICc cells was dispersed without specific preferred directions.

The studies so far commonly have agreed morphologically (Miller et al., 2005), functionally (Sturm et al., 2014), and electrophysiologically on the theory that the intrinsic innervation orientations are primarily in the direction of the isofrequency axis (Chandrasekaran et al., 2013), so that a cascaded feed-forward neuronal network (Miller et al., 2005; Chandrasekaran et al., 2013; Sturm et al., 2014) is formed combining similar frequencies (Sturm et al.,

2014). At this point, our results were consistent with the results of previous studies in the case of excitation, i.e. in that the first preferred orientation was aligned in the direction of the fibrodendritic laminae, spanned over a distance of as far as 800 μm and with a mean width of approx. 400 μm , which is likely to contain 2–3 layers of isofrequency sheets.

However, we also found that excitatory innervations from a minority of cells were oriented 120° to the horizontal axis, i.e. presumably the tonotopic axis in gerbils (Oliver, 2005; Merzenich and Reid, 1974). Additionally, the inhibitory innervations had no strong preferred orientations. These characteristics of intrinsic innervations had, however, not yet been found by other studies, although, we could find the following facts supporting our results both morphologically and physiologically.

First, by looking into the morphological arrangement of the neurons within the ICc, it is widely known that there are two principle cell types: There are disc-shaped cells with the dendritic field (Wallace et al., 2012) oriented in the direction of the fibro-dendritic laminae, i.e. in the direction of the isofrequency axis; Further, there are stellate cells with typically a dendritic field intersecting the fibro-dendritic laminae (Oliver and Morest, 1984; Oliver et al., 1991; Meininger et al., 1986; Ribak and Roberts, 1986; Zook and Casseday, 1985; Faye-Lund, 1985; Malmierca et al., 1993; Geniec and Morest, 1971; Kuwada et al., 1997). To start with, the thickness of the fibro-dendritic laminae is reported to be approx. 120 – 180 μm , and the thickness of the isofrequency sheets is reported to be non-uniform with a mean value of 175 μm on average over frequencies (Schreiner and Langner, 1997). Further, the dendritic fields of stellate cells are reportedly ranging from 100 – 600 μm (e.g. Rockel and Jones,

1973b). As a consequence, it can be concluded that even if some stellate cells are confined within a lamina (FitzPatrick, 1975), typically, the dendrites of stellate cells extend outside of the isofrequency lamina (Miller et al., 2005), and are likely to receive input from other isofrequency contours (Miller et al., 2005).

This conclusion is also in accordance with the experiments of Miller et al. (2005), who have used antero- and retrograde tracer to trace the intrinsic morphological connections of ICc cells, and at the same time determined the isofrequency laminae of the cells electrophysiologically (Miller et al., 2005). Miller et al. have shown that cells have been labeled mainly within the sheet of the tracer that indicates the fibrodendritic lamina. However, there have been a few multipolar cells, i.e. stellate cells that have been labelled in regions well outside of the sheet of the label, with their dendrites projecting towards the labelled sheet (Miller et al., 2005, Figure 8: the distance of the stellate cell from the soma to the midline of the fibrodendritic lamina can be estimated to be over 200 μm according to scale bar), which indicates that such stellate cells can receive inputs from a direction approximately perpendicular to the fibrodendritic sheets.

Support for our observation of an innervation orientation along the tonotopic axis can also be found in a recent electrophysiological study (Chandrasekaran et al., 2013). They have observed neuronal activity propagation on the responses to a single lateral lemniscus (LL) stimulation detected by voltage sensitive dyes in a coronal slice, and have reported the possible cross-lamina activity propagation with boosting by local circuits, besides the main propagation along the fibrodendritic laminae. Since the primary focus of the

study has been different, the authors have not further elaborated on local circuits. However, it can be read from their data that the presumably intralaminar response can propagate along the tonotopic axis within a time-frame of 0.6 ms with a distance of one third of the ventro-lateral to dorso-medial ICc dimension (Chandrasekaran et al., 2013, Figure 7B frame 379–380), which would be approximately 200–300 μm according to the scale bar offered on the same figure (Chandrasekaran et al., 2013, Figure 2). On that account, we assume that this fast cross-frequency propagation would be difficult, if only intrinsic innervation in the direction of isofrequency would exist.

The general reason for intrinsic innervations along the tonotopy axis not having been pointed out clearly yet can be assumed to be owing to the resolution of the experimental methods or/and the existence of spontaneous activity. For example, Chandrasekaran et al. (2013) have observed the spatial and temporal patterns macroscopically across the whole IC. However, the observation that connections are not confined within, but reaching out of the isofrequency sheet in the direction of the tonotopy axis, exists in most of the frames (e.g. Chandrasekaran et al., 2013, Figure 7, e.g. frame 388-403) but has not been discussed. The reason for this is presumably due to a low resolution of the voltage sensitive dyes and the existence of noise that have prevented a discussion of local changes.

In the study of Sturm et al. (2014), the signals of a presynaptic neuron have been indicated using electrical charges, whereas spontaneous activities, i.e. the spontaneous firing of presynaptic neurons (Dickson et al., 1997) and the mPSCs (Berretta and Jones, 1996) have been excluded by repeating and averaging over the experiments (Sturm et al., 2014). The experience gained

in our study (in our work we used P14–P16), indicated that the spontaneous activity rates in the ICc were particularly high in that age group. The same conclusion can be drawn from the results of Sturm et al. (2014) for all four age groups based on the observation that the electrical charges do not fully cease to zero over distance, especially for the age group of P13–P15 in the ventro-lateral ICc. Thus, we have to consider that the spontaneous activities could have possibly influenced the results in Sturm et al. (2014).

Under the assumption of high background spontaneous activities, the average electrical charge detected as a function of distance from the soma to the distal end of the dendrite can usually not cease to zero. We found that, as expected, this high rate of spontaneous activities could have been indirectly observed in the results of Sturm et al. (2014) in their diagram of electrical charge over distance (Sturm et al., 2014, Figure 6B P13–P15), in which they have shown that electrical charges have not been ceasing to zero but instead even have increased after a certain distance. Under such circumstances, the decision for the electrical charge thresholds, which had been used to distinguish the area of intrinsic and external inputs, could influence the results. That is to say, if the thresholds chosen were too high, some input areas might get lost, but if the threshold chosen were too low, some areas with high spontaneous activities would have been taken as input areas. Another example can be made in the cases where multiple orientation cells were observed in our study. If the spontaneous activities were too high, and the threshold of the electrical charges chosen were low, the empty area between the two orientations may have been included, and would have led to round or elliptical innervation fields instead of cells with multiple orientations. In our experiment, however,

we used a statistical algorithm combining four criteria including amplitudes and identified spontaneous activities using a significance value, which was a clear cut criteria and hence not affected by this problem (additional details will be discussed in the technical considerations in Section 4.5).

In addition, as our results showed that cells orienting solely in the tonotopic axis were rare (12.5%), the monopoly of innervation orientation observed from Sturm et al. (2014) thus could also be attributed to the small sample group (Sturm et al., 2014, 9–11 samples per age group) or on species differences between gerbils and mice.

4.4 Differences in the Innervation Organization of the ICx

The external cortex is one of the major subdivisions of the inferior colliculus, which is receiving both auditory and somatosensory input, but it is also the least understood (Loftus et al., 2008). Studies have been made on the neuronal organization (Rockel and Jones, 1973c), cytoarchitecture (Loftus et al., 2008) and afferent inputs (Shneiderman and Henkel, 1987; Shneiderman et al., 1988; Schofield and Cant, 1992, 1996; Oliver et al., 1997, 1999; Cant and Benson, 2003; Loftus et al., 2004; Cant and Benson, 2006) so far; however, no dedicated studies have been conducted specifically on the intrinsic innervations of the ICx, yet.

In our study we reported for the first time that ICx cells received a larger amount of intrinsic excitatory innervations compared to the ICc, with an elongated ellipse orienting in a direction parallel to the outer boundary of the IC

(lateral and ventro-lateral borders), extending to a mean distance of 700 μm in diameter and spanning over multiple ICx layers. In the case of inhibition, ICx cells received small amounts of innervations compared to the case of excitation, formed ellipses with dispersed orientations in all directions. This characteristic intrinsic innervation profile of the ICx distinguished it clearly from all three subregions in the ICc, especially from the most adjacent region, the lateral ICc, in terms of orientation, amount of inputs and innervation area.

At first, we want to elaborate on how the orientation of the dendritic field of the ICx cells is related to the orientation of intrinsic inputs. Cells in the ICx are more sparsely packed (Morest and Oliver, 1984), and almost all recent literature agrees that the ICx consists of three layers: layer one containing small cells, layer two containing small and a few medium size cells and layer three containing cells of all sizes but most prominently large multipolar cells (Mylius et al., 2014). However, previous descriptions of the orientations of the dendritic field of ICx cells are rare, inconsistent, species dependent, and also depend on the exact position of the cells in the ICx, and thus are difficult to compare. Of these descriptions, Malmierca et al. (2011) have studied the dorsal part of the ICx in the rat, and have described that all cells are oriented either in the direction towards the ICc or towards the border of the IC. Some earlier studies have described, that the dendrites of the medium-sized cells often point towards the brachium or ventro-laterally towards the tegmentum (Morest and Oliver, 1984; Faye-Lund and Osen, 1985), i.e. along the outer boundary of the IC. Thus, the orientation of the dendritic fields of cells in these studies is inconsistent with the orientation of the excitatory innervations. Because most ICx cells received both excitation and inhibition, and the

inhibitory inputs were diffused in all directions, we assume that the inhibitory inputs are not directly related to the orientation of the dendritic field.

Next, we want to compare the neurotransmitter levels of the ICx to the amount of innervation found in this thesis. Previous biochemical studies have shown that the ICx has a lower level of decarboxylase, which is an indicator of the neurotransmitter GABA, compared to other regions within the ICc, especially the medial ICc (Adams, 1979). This is consistent with our finding of a trend of smaller amounts of inhibitory inputs in the ICx compared to the combined data of the ventro-lateral and dorso-medial ICc (excluding the lateral ICc). In contrast, the ICx has also the same or lower levels of glutamate (Adams, 1979) compared to the rest of the ICc cells. However, in our results, the cells in the ICx received the largest amount of mean excitatory inputs among all IC regions. We have discussed the same anomaly already in the ventro-lateral ICc (see Section 4.1), where the lower levels of glutamate might be explained by the feed-forward network relay causing the glutamate projection into other regions, or by the assumption that the level of excitatory neurotransmitters cannot be used to explain the amount of excitatory inputs (see Section 4.1).

Finally, it is interesting to discuss how the large amount of excitatory and small amount of inhibitory innervations might facilitate the function of the ICx. Unlike the ICc, the ICx receives only limited ascending projections from the lower auditory brainstem (Coleman and Clerici, 1987; Ahuja and Wu, 2007), but rather descending inputs that originate from the auditory cortex. Recent studies have suggested that the ICx may play a unique role in the descending auditory system (Groff and Liberman, 2003; Ota et al., 2004; Loftus

et al., 2008). Moreover, the largest sources of ascending inputs in the ICx arise from the brainstem somatosensory groups, e.g. cuneate, gracile nuclei and spinal trigeminal nucleus in the tactile system, and are indirectly connected to the motor system via the SC (Coleman and Clerici, 1987). For example, one experiment in the cat has shown that the ICx has a large receptive field to skin stimulation, i.e. the whole tactile sensory system is represented in the ICx (Aitkin and Boyd, 1978). We can therefore assume that the purpose of the ICx is to converge information from auditory, visual, motor and tactile systems. A large amount of intrinsic excitatory innervations in combination with a small amount of inhibitory innervations in general facilitates the integration, which is similar in the ventro-lateral ICc that is an integration region with inputs from all nuclei in the lower brainstem. Additionally, our results showed that similar to the lateral ICc cells, the ICx cells also had a large membrane time constant (compared to the combined data of dorsal-medial ICc and ventro-lateral ICc) that facilitates slow processing, which also has been reported by Chandrasekaran et al. (2013) based on the observation of the ceasing of temporal activities upon LL stimulation. As in the case of the ventro-lateral ICc, slow processing may enhance integration of the different sensory inputs (Robards, 1979; Zhou and Shore, 2006), and a large amount of intrinsic excitatory and a small amount of inhibitory innervations may facilitate the integration of the multiple inputs (Chandrasekaran et al., 2013).

4.5 Technical Considerations

Recently, Sturm et al. (2014) also have used scanning photostimulation of caged glutamate to study the intrinsic network in the rat. However, their

study differs from this thesis in both experimental and statistical methods, which not only results in certain advantages and disadvantages between both approaches, but also might explain the differences in some of the results.

The main difference in results between the two studies is concerning the innervation orientations within the ICc. Sturm et al. (2014) have reported that the intrinsic networks in the rat ICc orient solely following the direction of the curvature of the isofrequency contour, both in excitation and in inhibition, with an average width of the maps corresponding to the fibro-dendritic laminae (Sturm et al., 2014). Our results, however, suggest that for the excitatory innervation, the majority of cells from the ICc have inputs oriented presumably in the direction of the isofrequency axis (Rockel and Jones, 1973c), whereas a minority of cells presumably is aligned with the tonotopic axis in gerbils (Oliver, 2005; Merzenich and Reid, 1974). Additionally, a few cells in our study took intrinsic innervations from both axes. On the contrary, the orientation of inhibitory innervation of the ICc cells in our results was dispersed without a certain preferred direction.

The setup and detailed experimental methods of our study and the work of Sturm et al. (2014) are not exactly the same. They have held their cells first at the chloride reverse potential (-65 mV), recording excitatory responses and then have changed to the reverse potential of AMPA and NMDA channels (0 mV), recording inhibitory responses, in order to acquire excitatory and inhibitory maps separately. Their galvanometer controlled mirror system has made this approach possible and time-saving. This is crucial, because an over-time incubation of caged glutamate can lead to cytotoxicity of the cells. According to our experience, the best experimental time was only between

20–30 minutes until 60–70 minutes after the caged-glutamate incubation, thus the total time of the experiment is quite limited. Because of this restriction of the experimental time and the setups available, we developed another approach by holding the membrane potential in between the chloride (-98 mV) and AMPA and NMDA reverse potential (approx. 10 mV) in order to acquire inputs of both excitatory and inhibitory type within one repetition. Consequently, the EPSC and IPSC had different amplitudes due to the holding potential (-60 mV), thus a comparison between the excitatory and inhibitory charges as in previous work (e.g. Sturm et al., 2014) would not have been meaningful. Instead, we used an additional algorithm to determine the significance of the stimulation sites in order to distinguish noise, i.e. the spontaneous firing of presynaptic neurons and mPSCs, from the signals. This algorithm brought us some advantages in the resolution and accuracy of our intrinsic input detection.

It has been well discussed already in Bendels et al. (2010) that the disadvantage of the general photo-stimulation methods is that they cannot deliver the exact amount of input sites, and that the results are influenced by spontaneous activities (Bendels et al., 2010). The algorithm from Bendels et al. has already been proven to successfully detect the PSC inputs in single trials, i.e. stimulating each site only once in the entorhinal cortex (Bendels et al., 2010). The fidelity of this method has been also proven in our experiments, in that we could acquire high correlations with extremely low significance values for correlations between corrected excitatory and inhibitory inputs (significant input sites minus the expected number of spontaneously evoked PSCs), and biophysiological and morphological cell parameters. This principle disadvan-

tage of the general photo-stimulation technique also has been shown in the result of related work. For example, the method has led to the conclusion that the map is not 'patched', as described in Sturm et al. (2014). Thus we can also assume that the empty area without presynaptic inputs between two innervation orientations of the cells might simply not be possible to be observed when using general photo-stimulation methods, which would have led to the conclusion of a round intrinsic innervation area in Sturm et al. (2014).

However, we think that our experiment could still be improved, when removing the time restriction of our setup, e.g. by using the scanning method of Sturm et al. (2014). The scanning then could be repeated three times and a map of average raw inputs could be used, before conducting the actual algorithm. Thus, the best method is probably a combination of both approaches, with a galvanometer controlled mirror system to acquire one single trail to save time and using our approach of detection and the significance algorithm to acquire the precise number of PSC input sites.

4.6 Conclusion

To summarize, this work provided an overview of the intrinsic networks within the IC. We found that both excitatory and inhibitory networks existed in all subregions of the ICc and the ICx with an innervation distance of about 200–350 μm . Moreover, it was shown that in case of excitation, the innervation directions of neurons in the ICc oriented mostly in the direction of the fibro-dendritic laminae and isofrequency axis, and neurons in the ICx oriented along the outer boundary of the IC. In contrast, the inhibitory innervations of both ICc and ICx neurons dispersed in different directions. Furthermore, this

work provided a first outline of the regional heterogeneity of IC neurons with respect to their intrinsic excitatory-inhibitory ratio. In particular, whereas for neurons in the dorsal-medial ICc, the average innervation profiles of excitation and inhibition were rather similar, the neurons in the ventro-lateral ICc and ICx showed a prevalence of excitation, whereas neurons in the lateral ICc showed no significant differences, neither in case of excitation nor inhibition. Additionally, regional heterogeneity was also shown for the amount of excitatory inputs and inhibitory inputs in some paired regions, from which especially ICx neurons were receiving larger excitatory inputs than ICc neurons. Moreover, it was shown that the amount of excitatory innervations was correlated with the apparent neuron surface and that the amount of inhibitory innervations was correlated with the synaptic properties. Hence, whereas in some regions cells probably vary largely in their apparent cell surfaces and synaptic properties, they probably are rather similar in other regions.

Bibliography

- Adams, J. C. (1979). Ascending projections to the inferior colliculus. *J Comp Neurol*, 183(3):519–38.
- Adams, J. C. and Wenthold, R. J. (1979). Distribution of putative amino acid transmitters, choline acetyltransferase and glutamate decarboxylase in the inferior colliculus. *Neuroscience*, 4(12):1947–51.
- Ahuja, T. K. and Wu, S. H. (2007). Intrinsic membrane properties and synaptic response characteristics of neurons in the rat's external cortex of the inferior colliculus. *Neuroscience*, 145(3):851–65.
- Aitkin, L. M. and Boyd, J. (1978). Acoustic input to the lateral pontine nuclei. *Hear Res*, 1(1):67–77.
- Aitkin, L. M., Kenyon, C. E., and Philpott, P. (1981). The representation of the auditory and somatosensory systems in the external nucleus of the cat inferior colliculus. *J Comp Neurol*, 196(1):25–40.
- Appell, P. P. and Behan, M. (1990). Sources of subcortical gabaergic projections to the superior colliculus in the cat. *J Comp Neurol*, 302(1):143–58.
- Bajo, V. M. and King, A. J. (2012). Cortical modulation of auditory processing in the midbrain. *Front Neural Circuits*, 6:114.

- Bajo, V. M., Nodal, F. R., Bizley, J. K., Moore, D. R., and King, A. J. (2007). The ferret auditory cortex: descending projections to the inferior colliculus. *Cereb Cortex*, 17(2):475–91.
- Bal, R., Green, G. G., Rees, A., and Sanders, D. J. (2002). Firing patterns of inferior colliculus neurons-histology and mechanism to change firing patterns in rat brain slices. *Neurosci Lett*, 317(1):42–6.
- Basta, D. and Vater, M. (2003). Membrane-based gating mechanism for auditory information in the mouse inferior colliculus. *Brain Res*, 968(2):171–8.
- Bekhterev, V. M. (1908). *Die Funktionen der Nervencentra*. G. Fischer.
- Bendels, M. H., Beed, P., Leibold, C., Schmitz, D., and Jochenning, F. W. (2008). A novel control software that improves the experimental workflow of scanning photostimulation experiments. *J Neurosci Methods*, 175(1):44–57.
- Bendels, M. H. K., Beed, P., Schmitz, D., Jochenning, F. W., and Leibold, C. (2010). Detection of input sites in scanning photostimulation data based on spatial correlations. *J Neurosci Methods*, 192(2):286–95.
- Berretta, N. and Jones, R. S. (1996). A comparison of spontaneous epscs in layer ii and layer iv-v neurons of the rat entorhinal cortex in vitro. *J Neurophysiol*, 76(2):1089–100.
- Brückner, S. and Rübsamen, R. (1995). Binaural response characteristics in isofrequency sheets of the gerbil inferior colliculus. *Hear Res*, 86(1-2):1–14.
- Callaway, E. M. (2002). Cell type specificity of local cortical connections. *J Neurocytol*, 31(3-5):231–7.

- Cant, N. B. and Benson, C. G. (2003). Parallel auditory pathways: projection patterns of the different neuronal populations in the dorsal and ventral cochlear nuclei. *Brain Res Bull*, 60(5-6):457–74.
- Cant, N. B. and Benson, C. G. (2005). An atlas of the inferior colliculus of the gerbil in three dimensions. *Hear Res*, 206(1-2):12–27.
- Cant, N. B. and Benson, C. G. (2006). Wisteria floribunda lectin is associated with specific cell types in the ventral cochlear nucleus of the gerbil, meriones unguiculatus. *Hear Res*, 216-217:64–72.
- Cant, N. B. and Benson, C. G. (2008). Organization of the inferior colliculus of the gerbil (meriones unguiculatus): projections from the cochlear nucleus. *Neuroscience*, 154(1):206–17.
- Casparly, D. M., Milbrandt, J. C., and Helfert, R. H. (1995). Central auditory aging: Gaba changes in the inferior colliculus. *Exp Gerontol*, 30(3-4):349–60.
- Casseday, J. H. and Covey, E. (1992). Frequency tuning properties of neurons in the inferior colliculus of an FM bat. *J Comp Neurol*, 319(1):34–50.
- Casseday, J. H., Covey, E., and Grothe, B. (1997). Neural selectivity and tuning for sinusoidal frequency modulations in the inferior colliculus of the big brown bat, eptesicus fuscus. *J Neurophysiol*, 77(3):1595–605.
- Casseday, J. H., Ehrlich, D., and Covey, E. (1994). Neural tuning for sound duration: role of inhibitory mechanisms in the inferior colliculus. *Science*, 264(5160):847–50.
- Casseday, J. H., Ehrlich, D., and Covey, E. (2000). Neural measurement of sound duration: control by excitatory-inhibitory interactions in the inferior colliculus. *J Neurophysiol*, 84(3):1475–87.

- Casseday, J. H., Fremouw, T., and Covey, E. (2002). *The inferior colliculus: a hub for the central auditory system*, pages 238–318. Springer.
- Casseday, J. H., Kobler, J. B., Isbey, S. F., and Covey, E. (1989). Central acoustic tract in an echolocating bat: an extralemniscal auditory pathway to the thalamus. *J Comp Neurol*, 287(2):247–59.
- Chandrasekaran, B. and Kraus, N. (2010). The scalp-recorded brainstem response to speech: neural origins and plasticity. *Psychophysiology*, 47(2):236–46.
- Chandrasekaran, L., Xiao, Y., and Sivaramakrishnan, S. (2013). Functional architecture of the inferior colliculus revealed with voltage-sensitive dyes. *Front Neural Circuits*, 7:41.
- Chen, C., Read, H. L., and Escabi, M. A. (2012). Precise feature based time scales and frequency decorrelation lead to a sparse auditory code. *J Neurosci*, 32(25):8454–68.
- Chernock, M. and Winer, J. (2003). Intrinsic and commissural connections of the rat inferior colliculus. In *Association for Research in Otolaryngology Abstracts*, volume 26, page 787.
- Clopton, B. M. and Winfield, J. A. (1973). Tonotopic organization in the inferior colliculus of the rat. *Brain Res*, 56:355–8.
- Coleman, J. R. and Clerici, W. J. (1987). Sources of projections to subdivisions of the inferior colliculus in the rat. *J Comp Neurol*, 262(2):215–26.
- Couchman, K., Grothe, B., and Felmy, F. (2010). Medial superior olivary neurons receive surprisingly few excitatory and inhibitory inputs with balanced strength and short-term dynamics. *The Journal of Neuroscience*, 30(50):17111–17121.
- Dantzker, J. L. and Callaway, E. M. (2000). Laminar sources of synaptic input to cortical inhibitory interneurons and pyramidal neurons. *Nat Neurosci*, 3(7):701–7.

- Dickson, R. M., Cubitt, A. B., Tsien, R. Y., and Moerner, W. E. (1997). On/off blinking and switching behaviour of single molecules of green fluorescent protein. *Nature*, 388(6640):355–8.
- Druga, R. and Syka, J. (1984). Projections from auditory structures to the superior colliculus in the rat. *Neurosci Lett*, 45(3):247–52.
- Edwards, S. B., Ginsburgh, C. L., Henkel, C. K., and Stein, B. E. (1979). Sources of subcortical projections to the superior colliculus in the cat. *J Comp Neurol*, 184(2):309–29.
- Ehret, G. (1997). The auditory midbrain, a ‘shunting yard’ of acoustical information processing. *The central auditory system*, pages 259–316.
- Ehret, G. and Schreiner, C. E. (2005). *Spectral and intensity coding in the auditory midbrain*, pages 312–345. Springer.
- Fathke, R. L. and Gabriele, M. L. (2009). Patterning of multiple layered projections to the auditory midbrain prior to experience. *Hear Res*, 249(1-2):36–43.
- Faye-Lund, H. (1985). The neocortical projection to the inferior colliculus in the albino rat. *Anat Embryol (Berl)*, 173(1):53–70.
- Faye-Lund, H. and Osen, K. K. (1985). Anatomy of the inferior colliculus in rat. *Anat Embryol (Berl)*, 171(1):1–20.
- Feldman, S. G. and Kruger, L. (1980). An axonal transport study of the ascending projection of medial lemniscal neurons in the rat. *J Comp Neurol*, 192(3):427–54.
- Feng, A. S., Simmons, J. A., and Kick, S. A. (1978). Echo detection and target-ranging neurons in the auditory system of the bat *ptesicus fuscus*. *Science*, 202(4368):645–8.

- FitzPatrick, K. A. (1975). Cellular architecture and topographic organization of the inferior colliculus of the squirrel monkey. *J Comp Neurol*, 164(2):185–207.
- Franzen, D. L., Gleiss, S. A., Berger, C., Kümpfbeck, F. S., Ammer, J. J., and Felmy, F. (2015). Development and modulation of intrinsic membrane properties control the temporal precision of auditory brain stem neurons. *J Neurophysiol*, 113(2):524–36.
- Frisina, R. D., Walton, J. P., Lynch-Armour, M. A., and Klotz, D. A. (1997). Efferent projections of a physiologically characterized region of the inferior colliculus of the young adult cba mouse. *J Acoust Soc Am*, 101(5 Pt 1):2741–53.
- Fubara, B. M., Casseday, J. H., Covey, E., and Schwartz-Bloom, R. D. (1996). Distribution of gabaa, gabab, and glycine receptors in the central auditory system of the big brown bat, *eptesicus fuscus*. *J Comp Neurol*, 369(1):83–92.
- Geniec, P. and Morest, D. K. (1971). The neuronal architecture of the human posterior colliculus. a study with the golgi method. *Acta Otolaryngol Suppl*, 295:1–33.
- Gonzalez Hernandez, T. H., Meyer, G., and Ferres-Torres, R. (1986). The commissural interconnections of the inferior colliculus in the albino mouse. *Brain Res*, 368(2):268–76.
- Gonzalez-Hernandez, T. H., Meyer, G., and Ferres-Torres, R. (1989). Development of neuronal types and laminar organization in the central nucleus of the inferior colliculus in the cat. *Neuroscience*, 30(1):127–41.
- Griffin, J. D. and Boulant, J. A. (1995). Temperature effects on membrane potential and input resistance in rat hypothalamic neurones. *J Physiol*, 488 (Pt 2):407–18.
- Groff, J. A. and Liberman, M. C. (2003). Modulation of cochlear afferent response by the lateral olivocochlear system: activation via electrical stimulation of the inferior colliculus. *J Neurophysiol*, 90(5):3178–200.

- Hattori, T. and Suga, N. (1997). The inferior colliculus of the mustached bat has the frequency-vs-latency coordinates. *J Comp Physiol A*, 180(3):271–84.
- Herrera, M., Correa, J., Sanchez del Campo, F., and Ruiz, A. (1988a). Stellate cells and their axonal patterns in the central nucleus of the inferior colliculus of the cat (*felis domesticus*). *J Hirnforsch*, 29(4):393–402.
- Herrera, M., Sanchez del Campo, F., Puchades, A., and Correa, J. (1989). Axonal patterns of disc-shaped cells in the central nucleus of the cat inferior colliculus. *Z Mikrosk Anat Forsch*, 103(3):515–25.
- Herrera, M., Sanchez del Campo, F., and Puchades Orts, A. (1988b). Cytoarchitecture and axonal systems in the commissural nucleus of the inferior colliculus in the albino rat. a golgi study. *J Hirnforsch*, 29(2):165–74.
- Hille, B. (2001). *Ion Channels of Excitable Membranes (3rd Edition)*. Sinauer Associates Inc 2001-07, 3rd edition edition.
- Hind, J. E., Goldberg, J. M., Greenwood, D. D., and Rose, J. E. (1963). Some discharge characteristics of single neurons in the inferior colliculus of the cat. ii. timing of the discharges and observations on binaural stimulation. *J Neurophysiol*, 26:321–41.
- Hirsch, J. A. and Oertel, D. (1988). Intrinsic properties of neurones in the dorsal cochlear nucleus of mice, in vitro. *J Physiol*, 396:535–48.
- Kelly, J. B., Liscum, A., van Adel, B., and Ito, M. (1998). Projections from the superior olive and lateral lemniscus to tonotopic regions of the rat's inferior colliculus. *Hear Res*, 116(1-2):43–54.
- King, A. J., Jiang, Z. D., and Moore, D. R. (1998). Auditory brainstem projections to the ferret superior colliculus: anatomical contribution to the neural coding of sound azimuth. *J Comp Neurol*, 390(3):342–65.

- Kitzes, L. M. (1984). Some physiological consequences of neonatal cochlear de-struction in the inferior colliculus of the gerbil, *Meriones unguiculatus*. *Brain Res*, 306(1-2):171–8.
- Koch, U. and Grothe, B. (2003). Hyperpolarization-activated current (ih) in the infe-rior colliculus: distribution and contribution to temporal processing. *J Neurophysiol*, 90(6):3679–87.
- Kötter, R., Schubert, D., Dyhrfeld-Johnsen, J., Luhmann, H. J., and Staiger, J. F. (2005). Optical release of caged glutamate for stimulation of neurons in the in vitro slice preparation. *J Biomed Opt*, 10(1):11003.
- Kudo, M. and Niimi, K. (1980). Ascending projections of the inferior colliculus in the cat: an autoradiographic study. *J Comp Neurol*, 191(4):545–56.
- Kudoh, S. N. and Taguchi, T. (2002). A simple exploratory algorithm for the accurate and fast detection of spontaneous synaptic events. *Biosens Bioelectron*, 17(9):773–82.
- Kuwada, S. and Batra, R. (1999). Coding of sound envelopes by inhibitory rebound in neurons of the superior olivary complex in the unanesthetized rabbit. *J Neurosci*, 19(6):2273–87.
- Kuwada, S., Batra, R., Yin, T. C., Oliver, D. L., Haberly, L. B., and Stanford, T. R. (1997). Intracellular recordings in response to monaural and binaural stimulation of neurons in the inferior colliculus of the cat. *J Neurosci*, 17(19):7565–81.
- Langner, G. and Schreiner, C. E. (1988). Periodicity coding in the inferior colliculus of the cat. i. neuronal mechanisms. *J Neurophysiol*, 60(6):1799–822.
- Li, L., Korngut, L. M., Frost, B. J., and Beninger, R. J. (1998). Prepulse inhibition following lesions of the inferior colliculus: prepulse intensity functions. *Physiol Behav*, 65(1):133–9.

- Loftus, W. C., Bishop, D. C., Saint Marie, R. L., and Oliver, D. L. (2004). Organization of binaural excitatory and inhibitory inputs to the inferior colliculus from the superior olive. *J Comp Neurol*, 472(3):330–44.
- Loftus, W. C., Malmierca, M. S., Bishop, D. C., and Oliver, D. L. (2008). The cytoarchitecture of the inferior colliculus revisited: a common organization of the lateral cortex in rat and cat. *Neuroscience*, 154(1):196–205.
- Malmierca, M. S., Blackstad, T. W., and Osen, K. K. (2011). Computer-assisted 3-D reconstructions of golgi-impregnated neurons in the cortical regions of the inferior colliculus of rat. *Hear Res*, 274(1-2):13–26.
- Malmierca, M. S., Blackstad, T. W., Osen, K. K., Karagulle, T., and Molowny, R. L. (1993). The central nucleus of the inferior colliculus in rat: a golgi and computer reconstruction study of neuronal and laminar structure. *J Comp Neurol*, 333(1):1–27.
- Malmierca, M. S., Hernandez, O., and Rees, A. (2005). Intercollicular commissural projections modulate neuronal responses in the inferior colliculus. *Eur J Neurosci*, 21(10):2701–10.
- Malmierca, M. S., Izquierdo, M. A., Cristaudo, S., Hernandez, O., Perez-Gonzalez, D., Covey, E., and Oliver, D. L. (2008). A discontinuous tonotopic organization in the inferior colliculus of the rat. *J Neurosci*, 28(18):4767–76.
- Malmierca, M. S., Rees, A., Le Beau, F. E., and Bjaalie, J. G. (1995). Laminar organization of frequency-defined local axons within and between the inferior colliculi of the guinea pig. *J Comp Neurol*, 357(1):124–44.
- Mei, H. X., Cheng, L., and Chen, Q. C. (2013). Neural interactions in unilateral colliculus and between bilateral colliculi modulate auditory signal processing. *Front Neural Circuits*, 7:68.

- Meininger, V., Pol, D., and Derer, P. (1986). The inferior colliculus of the mouse. a nissl and golgi study. *Neuroscience*, 17(4):1159–79.
- Merchan, M., Aguilar, L. A., Lopez-Poveda, E. A., and Malmierca, M. S. (2005). The inferior colliculus of the rat: quantitative immunocytochemical study of gaba and glycine. *Neuroscience*, 136(3):907–25.
- Merzenich, M. M. and Reid, M. D. (1974). Representation of the cochlea within the inferior colliculus of the cat. *Brain Res*, 77(3):397–415.
- Miller, K. E., Casseday, J. H., and Covey, E. (2005). Relation between intrinsic connections and isofrequency contours in the inferior colliculus of the big brown bat, *ptesicus fuscus*. *Neuroscience*, 136(3):895–905.
- Moore, D. R. (1985). Postnatal development of the mammalian central auditory system and the neural consequences of auditory deprivation. *Acta Otolaryngol Suppl*, 421:19–30.
- Moore, D. R. (1991). Anatomy and physiology of binaural hearing. *Audiology*, 30(3):125–34.
- Morest, D. K. and Oliver, D. L. (1984). The neuronal architecture of the inferior colliculus in the cat: defining the functional anatomy of the auditory midbrain. *J Comp Neurol*, 222(2):209–36.
- Moriizumi, T. and Hattori, T. (1991). Pallidotectal projection to the inferior colliculus of the rat. *Exp Brain Res*, 87(1):223–6.
- Muller-Ribeiro, F. C., Dampney, R. A., McMullan, S., Fontes, M. A., and Goodchild, A. K. (2014). Disinhibition of the midbrain colliculi unmasks coordinated autonomic, respiratory, and somatomotor responses to auditory and visual stimuli. *Am J Physiol Regul Integr Comp Physiol*, 307(8):R1025–35.

- Mylius, J., Brosch, M., Scheich, H., and Budinger, E. (2013). Subcortical auditory structures in the Mongolian gerbil: I. golgi architecture. *J Comp Neurol*, 521(6):1289–321.
- Mylius, J., Happel, M. F., Gorkin, A. G., Huang, Y., Scheich, H., and Brosch, M. (2014). Fast transmission from the dopaminergic ventral midbrain to the sensory cortex of awake primates. *Brain Struct Funct*.
- Nakamoto, K. T., Mellott, J. G., Killius, J., Storey-Workley, M. E., Sowick, C. S., and Schofield, B. R. (2014). Ultrastructural characterization of gabaergic and excitatory synapses in the inferior colliculus. *Front Neuroanat*, 8:108.
- Nieuwenhuys, R., Voogd, J., and Van Huijzen, C. (2007). *The human central nervous system: a synopsis and atlas*. Springer Science & Business Media.
- Oertel, D., Fay, R. R., and Popper, A. N. (2002). *Integrative functions in the mammalian auditory pathway*, volume 15. Springer Science & Business Media.
- Oliver, D. L. (1984). Dorsal cochlear nucleus projections to the inferior colliculus in the cat: a light and electron microscopic study. *J Comp Neurol*, 224(2):155–72.
- Oliver, D. L. (2005). *Neuronal organization in the inferior colliculus*, pages 69–114. Springer.
- Oliver, D. L., Beckius, G. E., Bishop, D. C., and Kuwada, S. (1997). Simultaneous anterograde labeling of axonal layers from lateral superior olive and dorsal cochlear nucleus in the inferior colliculus of cat. *J Comp Neurol*, 382(2):215–29.
- Oliver, D. L., Beckius, G. E., Bishop, D. C., Loftus, W. C., and Batra, R. (2003). Topography of interaural temporal disparity coding in projections of medial superior olive to inferior colliculus. *J Neurosci*, 23(19):7438–49.

- Oliver, D. L., Kuwada, S., Yin, T. C., Haberly, L. B., and Henkel, C. K. (1991). Dendritic and axonal morphology of hrp-injected neurons in the inferior colliculus of the cat. *J Comp Neurol*, 303(1):75–100.
- Oliver, D. L. and Morest, D. K. (1984). The central nucleus of the inferior colliculus in the cat. *J Comp Neurol*, 222(2):237–64.
- Oliver, D. L., Ostapoff, E. M., and Beckius, G. E. (1999). Direct innervation of identified tectothalamic neurons in the inferior colliculus by axons from the cochlear nucleus. *Neuroscience*, 93(2):643–58.
- Ota, Y., Oliver, D. L., and Dolan, D. F. (2004). Frequency-specific effects on cochlear responses during activation of the inferior colliculus in the Guinea pig. *J Neurophysiol*, 91(5):2185–93.
- Peruzzi, D., Bartlett, E., Smith, P. H., and Oliver, D. L. (1997). A monosynaptic gabaergic input from the inferior colliculus to the medial geniculate body in rat. *J Neurosci*, 17(10):3766–77.
- Peruzzi, D., Sivaramakrishnan, S., and Oliver, D. L. (2000). Identification of cell types in brain slices of the inferior colliculus. *Neuroscience*, 101(2):403–16.
- Porres, C. (2012). *Neural circuit analysis of the dorsal nucleus of the lateral lemniscus and new viral approaches to neural circuit analysis in Mongolian gerbils*. PhD thesis, Ludwig-Maximilians-Universität München.
- Prus, J. (1899). Bemerkungen zu dem aufsatze des herr docenten dr. bernheimer: Die beziehungen der vorderen vierhügel zu den augenbewegungen. *Wiener klinische Wochenschrift*, 112:1311–1312.
- Rall, W. (1969). Time constants and electrotonic length of membrane cylinders and neurons. *Biophys J*, 9(12):1483–508.

- Ramón y Cajal, S. (1911). Histologie du système nerveux de l'homme et des vertébrés. *Maloine, Paris*, 2:415–426.
- Rasmussen, G. L. (1946). The olivary peduncle and other fiber projections of the superior olivary complex. *Journal of Comparative Neurology*, 84(2):141–219.
- Reetz, G. and Ehret, G. (1999). Inputs from three brainstem sources to identified neurons of the mouse inferior colliculus slice. *Brain Res*, 816(2):527–43.
- Ress, D. and Chandrasekaran, B. (2013). Tonotopic organization in the depth of human inferior colliculus. *Front Hum Neurosci*, 7:586.
- Ribak, C. E. and Roberts, R. C. (1986). The ultrastructure of the central nucleus of the inferior colliculus of the sprague-dawley rat. *J Neurocytol*, 15(4):421–38.
- Robards, M. J. (1979). Somatic neurons in the brainstem and neocortex projecting to the external nucleus of the inferior colliculus: an anatomical study in the opossum. *J Comp Neurol*, 184(3):547–65.
- Rockel, A. J. and Jones, E. G. (1973a). The neuronal organization of the inferior colliculus of the adult cat. i. the central nucleus. *J Comp Neurol*, 147(1):11–60.
- Rockel, A. J. and Jones, E. G. (1973b). The neuronal organization of the inferior colliculus of the adult cat. ii. the pericentral nucleus. *J Comp Neurol*, 149(3):301–34.
- Rockel, A. J. and Jones, E. G. (1973c). Observations on the fine structure of the central nucleus of the inferior colliculus of the cat. *J Comp Neurol*, 147(1):61–92.
- Romand, R. and Ehret, G. (1990). Development of tonotopy in the inferior colliculus. i. electrophysiological mapping in house mice. *Brain Res Dev Brain Res*, 54(2):221–34.

- Roth, G. L., Aitkin, L. M., Andersen, R. A., and Merzenich, M. M. (1978). Some features of the spatial organization of the central nucleus of the inferior colliculus of the cat. *J Comp Neurol*, 182(4):661–80.
- Rouiller, E. M., Hornung, J. P., and De Ribaupierre, F. (1989). Extrathalamic ascending projections to physiologically identified fields of the cat auditory cortex. *Hear Res*, 40(3):233–46.
- Saint Marie, R. L. (1996). Glutamatergic connections of the auditory midbrain: selective uptake and axonal transport of d-[3H]aspartate. *J Comp Neurol*, 373(2):255–70.
- Saldana, E., Feliciano, M., and Mugnaini, E. (1996). Distribution of descending projections from primary auditory neocortex to inferior colliculus mimics the topography of intracollicular projections. *J Comp Neurol*, 371(1):15–40.
- Saldana, E. and Merchan, M. A. (1992). Intrinsic and commissural connections of the rat inferior colliculus. *J Comp Neurol*, 319(3):417–37.
- Sawatari, A. and Callaway, E. M. (2000). Diversity and cell type specificity of local excitatory connections to neurons in layer 3B of monkey primary visual cortex. *Neuron*, 25(2):459–71.
- Sayegh, R., Aubie, B., and Faure, P. A. (2014). Dichotic sound localization properties of duration-tuned neurons in the inferior colliculus of the big brown bat. *Front Physiol*, 5:215.
- Schofield, B. R. and Cant, N. B. (1992). Organization of the superior olivary complex in the guinea pig: II. patterns of projection from the periolivary nuclei to the inferior colliculus. *J Comp Neurol*, 317(4):438–55.

- Schofield, B. R. and Cant, N. B. (1996). Projections from the ventral cochlear nucleus to the inferior colliculus and the contralateral cochlear nucleus in guinea pigs. *Hear Res*, 102(1-2):1–14.
- Schreiner, C. E. and Langner, G. (1988). Periodicity coding in the inferior colliculus of the cat. ii. topographical organization. *J Neurophysiol*, 60(6):1823–40.
- Schreiner, C. E. and Langner, G. (1997). Laminar fine structure of frequency organization in auditory midbrain. *Nature*, 388(6640):383–6.
- Schreiner, C. E. and Winer, J. A. (2005). *The inferior colliculus*. Springer.
- Semple, M. N. and Aitkin, L. M. (1979). Representation of sound frequency and laterality by units in central nucleus of cat inferior colliculus. *J Neurophysiol*, 42(6):1626–39.
- Serviere, J., Webster, W. R., and Calford, M. B. (1984). Isofrequency labelling revealed by a combined [14C]-2-deoxyglucose, electrophysiological, and horseradish peroxidase study of the inferior colliculus of the cat. *J Comp Neurol*, 228(4):463–77.
- Shammah-Lagnado, S. J., Alheid, G. F., and Heimer, L. (1996). Efferent connections of the caudal part of the globus pallidus in the rat. *J Comp Neurol*, 376(3):489–507.
- Shneiderman, A. and Henkel, C. K. (1987). Banding of lateral superior olivary nucleus afferents in the inferior colliculus: a possible substrate for sensory integration. *J Comp Neurol*, 266(4):519–34.
- Shneiderman, A., Oliver, D. L., and Henkel, C. K. (1988). Connections of the dorsal nucleus of the lateral lemniscus: an inhibitory parallel pathway in the ascending auditory system? *J Comp Neurol*, 276(2):188–208.
- Sivaramakrishnan, S. and Oliver, D. L. (2001). Distinct k currents result in physiologically distinct cell types in the inferior colliculus of the rat. *J Neurosci*, 21(8):2861–77.

- Smith, P. H. (1992). Anatomy and physiology of multipolar cells in the rat inferior collicular cortex using the in vitro brain slice technique. *J Neurosci*, 12(9):3700–15.
- Sotoca, J. V., Alvarado, J. C., Fuentes-Santamaria, V., Martinez-Galan, J. R., and Caminos, E. (2014). Hearing impairment in the p23H-1 retinal degeneration rat model. *Front Neurosci*, 8:297.
- Spiegel, E. (1926). Experimentalstudien am nervensystem. *Pflügers Archiv European Journal of Physiology*, 212(1):769–780.
- Stiebler, I. and Ehret, G. (1985). Inferior colliculus of the house mouse. i. a quantitative study of tonotopic organization, frequency representation, and tone-threshold distribution. *J Comp Neurol*, 238(1):65–76.
- Straka, M. M., Hughes, R., Lee, P., and Lim, H. H. (2015). Descending and tonotopic projection patterns from the auditory cortex to the inferior colliculus. *Neuroscience*, 300:325–337.
- Sturm, J., Nguyen, T., and Kandler, K. (2014). Development of intrinsic connectivity in the central nucleus of the mouse inferior colliculus. *J Neurosci*, 34(45):15032–46.
- Taschenberger, H., Scheuss, V., and Neher, E. (2005). Release kinetics, quantal parameters and their modulation during short-term depression at a developing synapse in the rat CNS. *J Physiol*, 568(Pt 2):513–37.
- Tokunaga, A., Sugita, S., and Otani, K. (1984). Auditory and non-auditory subcortical afferents to the inferior colliculus in the rat. *J Hirnforsch*, 25(4):461–72.
- Uteshev, V. V. and Pennefather, P. S. (1996). A mathematical description of miniature postsynaptic current generation at central nervous system synapses. *Biophys J*, 71(3):1256–66.

- Vater, M., Casseday, J. H., and Covey, E. (1995). Convergence and divergence of ascending binaural and monaural pathways from the superior olives of the mustached bat. *J Comp Neurol*, 351(4):632–46.
- Venkataraman, Y. and Bartlett, E. L. (2013). Postnatal development of synaptic properties of the gabaergic projection from the inferior colliculus to the auditory thalamus. *J Neurophysiol*, 109(12):2866–82.
- Wagner, T. (1994). Intrinsic properties of identified neurones in the central nucleus of mouse inferior colliculus. *Neuroreport*, 6(1):89–93.
- Wagner, T. (1996). Lemniscal input to identified neurons of the central nucleus of mouse inferior colliculus: an intracellular brain slice study. *Eur J Neurosci*, 8(6):1231–9.
- Wallace, M. M., Kavianpour, S. M., and Gabriele, M. L. (2013). Ephrin-b2 reverse signaling is required for topography but not pattern formation of lateral superior olivary inputs to the inferior colliculus. *J Comp Neurol*, 521(7):1585–97.
- Wallace, M. N., Shackleton, T. M., and Palmer, A. R. (2012). Morphological and physiological characteristics of laminar cells in the central nucleus of the inferior colliculus. *Front Neural Circuits*, 6:55.
- Wang, L., Devore, S., Delgutte, B., and Colburn, H. S. (2014). Dual sensitivity of inferior colliculus neurons to itd in the envelopes of high-frequency sounds: experimental and modeling study. *J Neurophysiol*, 111(1):164–81.
- Wiberg, M., Westman, J., and Blomqvist, A. (1987). Somatosensory projection to the mesencephalon: an anatomical study in the monkey. *J Comp Neurol*, 264(1):92–117.
- Willmore, B. D., Cooke, J. E., and King, A. J. (2014). Hearing in noisy environments: noise invariance and contrast gain control. *J Physiol*, 592(Pt 16):3371–81.

- Winer, J. and Schreiner, C. (2005). The central auditory system: A functional analysis. In Winer, J. and Schreiner, C., editors, *The Inferior Colliculus*, pages 1–68. Springer New York.
- Wu, S. H. (2005). *Biophysical properties of inferior colliculus neurons*, pages 282–311. Springer.
- Xie, R., Gittelman, J. X., Li, N., and Pollak, G. D. (2008). Whole cell recordings of intrinsic properties and sound-evoked responses from the inferior colliculus. *Neuroscience*, 154(1):245–256.
- Xiong, X. R., Liang, F., Li, H., Mesik, L., Zhang, K. K., Polley, D. B., Tao, H. W., Xiao, Z., and Zhang, L. I. (2013). Interaural level difference-dependent gain control and synaptic scaling underlying binaural computation. *Neuron*, 79(4):738–53.
- Yassin, L., Pecka, M., Kajopoulos, J., Gleiss, H., Li, L., Leibold, C., and Felmy, F. (2015). A unifying functional organization principle in the auditory midbrain based on temporal processing precision. Unpublished paper.
- Yasui, Y., Nakano, K., Kayahara, T., and Mizuno, N. (1991). Non-dopaminergic projections from the substantia nigra pars lateralis to the inferior colliculus in the rat. *Brain Res*, 559(1):139–44.
- Zarrinpar, A. and Callaway, E. M. (2014). Functional local input to layer 5 pyramidal neurons in the rat visual cortex. *Cereb Cortex*.
- Zhang, Y., Hakes, J. J., Bonfield, S. P., and Yan, J. (2005). Corticofugal feedback for auditory midbrain plasticity elicited by tones and electrical stimulation of basal forebrain in mice. *Eur J Neurosci*, 22(4):871–9.
- Zhou, J. and Shore, S. (2006). Convergence of spinal trigeminal and cochlear nucleus projections in the inferior colliculus of the guinea pig. *J Comp Neurol*, 495(1):100–12.

Zook, J. M. and Casseday, J. H. (1985). Projections from the cochlear nuclei in the mustache bat, *pteronotus parnellii*. *J Comp Neurol*, 237(3):307–24.

Eidesstattliche Versicherung/Affidavit

Hiermit versichere ich an Eides statt, dass ich die vorliegende Dissertation *Intrinsic Structure of the Inferior Colliculus* selbstständig angefertigt habe, mich außer der angegebenen keiner weiteren Hilfsmittel bedient und alle Erkenntnisse, die aus dem Schrifttum ganz oder annähernd übernommen sind, als solche kenntlich gemacht und nach ihrer Herkunft unter Bezeichnung der Fundstelle einzeln nachgewiesen habe.

I hereby confirm that the dissertation *Intrinsic Structure of the Inferior Colliculus* is the result of my own work and that I have only used sources or materials listed and specified in the dissertation.

München, den 08. Dez. 2016

Munich, December 8th, 2016

Lu Li

Author Contributions

The author, Lu LI, performed all experiments, and acquired and analyzed all data. The thesis has been solely written by Lu LI and the work has been supervised by Prof. Dr. Christian Leibold and Prof. Dr. Felix Felmy.